

# Electron–hole liquid in semiconductors and low-dimensional structures

N N Sibeldin

DOI: <https://doi.org/10.3367/UFNe.2017.08.038194>

## Contents

1. Introduction	1147
2. Electron–hole liquid in semiconductors	1149
2.1 Density and binding energy of the electron–hole liquid; 2.2 Stability of the electron–hole liquid; 2.3 Phase diagrams; 2.4 Size and concentration of EHDs; 2.5 Kinetics of exciton condensation; 2.6 Recombination kinetics; 2.7 Motion of EHDs under external forces; 2.8 Giant electron–hole drops; 2.9 Phonon wind; 2.10 Spatial structure and dynamics of the electron–hole drop cloud	
3. Electron–hole liquid in low-dimensional semiconductor structures	1164
3.1 Stability of the electron–hole liquid in low-dimensional structures; 3.2 Condensation of dipolar excitons in GaAs/AlGaAs structures with double quantum wells; 3.3 Quantum electron–hole droplets (dropletons); 3.4 Electron–hole liquid in type-I silicon quantum wells; 3.5 Spatially direct and dipolar electron–hole liquids in type-II Si–Ge heterostructures	
4. Conclusions	1174
References	1175

**Abstract.** The condensation of excitons into an electron–hole liquid (EHL) and the main EHL properties in bulk semiconductors and low-dimensional structures are considered. The EHL properties in bulk materials are discussed primarily in qualitative terms based on the experimental results obtained for germanium and silicon. Some of the experiments in which the main EHL thermodynamic parameters (density and binding energy) have been obtained are described and the basic factors that determine these parameters are considered. Topics covered include the effect of external perturbations (uniaxial strain and magnetic field) on EHL stability; phase diagrams for a nonequilibrium exciton–gas–EHL system; information on the size and concentration of electron–hole drops (EHDs) under various experimental conditions; the kinetics of exciton condensation and of recombination in the exciton–gas–EHD system; dynamic EHD properties and the motion of EHDs under the action of external forces; the properties of giant EHDs that form in potential wells produced by applying an inhomogeneous strain to the crystal; and effects associated with the drag of EHDs by nonequilibrium phonons (phonon wind), including the dynamics and formation of an anisotropic spatial structure of the EHD cloud. In discussing EHLs in low-dimensional structures, a number of studies are reviewed on the observation

and experimental investigation of phenomena such as spatially indirect (dipolar) electron–hole and exciton (dielectric) liquids in GaAs/AlGaAs structures with double quantum wells (QWs), EHDs containing only a few electron–hole pairs (dropletons), EHLs in type-I silicon QWs, and spatially direct and dipolar EHLs in type-II silicon–germanium heterostructures.

**Keywords:** excitons, electron–hole liquid, density, binding energy, stability, phase diagram, thermodynamic parameters, electron–hole droplet, droplet size and concentration, condensation kinetics, recombination kinetics, droplet motion, giant droplets, phonon wind, drag effect, droplet cloud, spatial structure of droplet cloud, dynamics of droplet cloud, strain field, magnetic field, low-dimensional structures, quantum wells, electron–hole bilayers, spatially direct and dipolar excitons, spatially direct and dipolar liquids, dropletons.

*To the cherished memory of the Mentor*

## 1. Introduction

In 1968, L V Keldysh introduced and substantiated the idea of the possibility of condensation of excitons in a semiconductor into a metallic electron–hole liquid (EHL) in which electrons and holes are collectivized and are bound together by internal interaction forces [1–3]. The general features of this phase transition are similar to those of the condensation of an alkali-metal vapor into a liquid metal.<sup>1</sup> Similarly to conventional gas–liquid transitions, exciton condensation is a first-order phase transition and occurs at

<sup>1</sup> See, e.g., [4].

N N Sibeldin Lebedev Physical Institute, Russian Academy of Sciences, Leninskii prosp. 53, 119991 Moscow, Russian Federation  
E-mail: [sibeldin@sci.lebedev.ru](mailto:sibeldin@sci.lebedev.ru)

Received 31 July 2017, revised 23 August 2017  
*Uspekhi Fizicheskikh Nauk* 187 (11) 1236–1270 (2017)  
DOI: <https://doi.org/10.3367/UFNe.2017.08.038194>  
Translated by M Skorikov; edited by A M Semikhatov

temperatures below the critical temperature when the exciton gas density exceeds the ‘saturated vapor’ density or, at a given exciton density, when the temperature is reduced to the ‘dew point.’

Within the following year, EHL was discovered experimentally in germanium crystals: recombination radiation from EHL at high levels of optical excitation and liquid-helium temperatures was identified by Pokrovskii and Svistunova [5], the motion of electron–hole drops (EHDs) at macroscopic distances in nonuniformly strained samples was observed by Bagaev et al. [6], and resonance absorption of far-infrared radiation by the drops of the condensed phase was measured by Vavilov et al. [7]. Less clear evidence for the occurrence of the liquid phase was obtained in [8], where absorption changes in the spectral region of direct exciton transitions in germanium introduced by optical pumping was investigated.<sup>2</sup>

The first studies of exciton condensation stimulated further interest in this problem, which became a field of intense activity. Much attention was attracted to this research area due to the unusual and beautiful nature of the phenomenon: a gas–liquid transition occurs in a nonequilibrium electron–hole system in a semiconductor crystal, which leads to the diversity and uniqueness of the properties of EHDs. Furthermore, the exciton system in a semiconductor is an excellent model object for the experimental investigation of the properties of matter under conditions that cannot be attained in laboratory for conventional matter (e.g., the conditions of ultrahigh magnetic fields).

To date, exciton condensation and the properties of EHL in bulk semiconductors have been rather broadly and comprehensively investigated both theoretically and experimentally. Many novel and totally unexpected effects have been discovered. Although by no means all ideas and possibilities have been realized, it can be stated that for a number of semiconductors, the main properties of the exciton–gas–EHL system, peculiarities of the phase transition, EHL parameters, properties of EHL drops, etc. have been fairly well studied and, in general, understood. EHL has been observed in Ge, Si, GaP, GaAs, CdS, and many other semiconductors. The gas–liquid phase transition and EHL properties are investigated in most detail in germanium and silicon, which are classical materials for studying this phenomenon. The material parameters of Ge and Si and the characteristics of excitons and the EHL in these semiconductors are beneficial for a clear manifestation of the diverse properties of the exciton–gas–EHL system, which can be investigated extensively in experiments of different types. Studies of the EHL in bulk materials are presented in a number of review papers and monographs [11–18], containing sufficiently comprehensive information about theoretical and experimental results obtained in this field, as well as references to virtually all the main original papers and earlier reviews published at the time.

Space limitations make it impossible to cover in full the results obtained in this field. In Section 2, we try to describe the basic features of the exciton condensation phenomenon and EHL properties in bulk materials, primarily in qualitative terms on the basis of experimental results obtained for germanium and silicon and without going into detail. More

detailed information on the properties and characteristics of EHL in other semiconductors can be found in [19].

Section 3 describes the experimental studies of excitonic effects, particle–particle interactions, and phase transitions in nonequilibrium electron–hole systems in semiconductor nanostructures, mainly in heterostructures with quantum wells (QWs). Theoretical ideas about effects that can occur in these systems began to take shape as early as the 1970s. Keldysh and members of his school considered several types of electron–hole systems whose common feature is the high anisotropy of the electron spectrum [20]. It was shown that under certain conditions, the electron–hole plasma (EHP) in these systems undergoes self-compression, leading to the formation of a stable high-density EHL with a high binding energy. In particular, the systems that were analyzed in those early studies included arrays of quasi-one-dimensional conducting wires and quasi-two-dimensional (multilayer) systems of conducting planes. The phase diagrams and the critical temperatures and densities of the gas–liquid transition in a multilayer electron–hole system were calculated in [21].

A system with spatially separated electron and hole layers occupying the opposite parallel boundary planes of an ultrathin semiconductor film (electron–hole bilayer) was considered by Andryushin and Silin [22, 23]. It was demonstrated that for certain thicknesses of the film, the metallic EHL is stable against the gas of excitons composed of spatially separated electrons and holes (dipolar excitons), and, furthermore, that the ordering of the heavier particles can occur in a system of this kind with a large difference between the electron and hole masses. The possibilities of exciton Bose condensation, superfluidity, and superconductivity in spatially separated layers of electrons and holes were studied theoretically in [24, 25]. Gas–liquid phase transitions and the properties of the excitonic (dielectric) liquid phase were later analyzed in detail in [26].

Arguably, most of the efforts in the investigation of phase transitions in low-dimensional electron–hole systems are currently devoted to studies of electron–hole bilayers. Theoretical work in this area mainly concerns the properties of the ground state of the electron–hole system and gas–liquid phase transitions [27–36], Bose condensation of spatially indirect (dipolar) excitons [37–42], spatial distribution and ‘dark’ states of the condensate [43–48], Wigner crystallization [49, 50], collective modes in the liquid [55, 56], Mott transition in the exciton system [57–60], exciton condensation in graphene bilayers [61–63], etc.

Electron–hole bilayers can be formed at interfaces in type-II heterostructures, as well as in double QWs (two QWs separated by a thin tunneling-transparent potential barrier) or wide single QWs in type-I heterostructures to which an electric field is applied along the growth axis. The Bose condensation of dipolar excitons in double QWs in GaAs/AlGaAs heterostructures was the subject of a series of studies by Butov et al. (see, e.g., [64–66]) and by Gorbunov and Timofeev [67, 68]. The latter team also observed and investigated Bose condensation in wide single QWs in detail [69, 70]. In their study of the exciton Bose condensate in single wide QWs, Alloing et al. [71] established that ‘dark’ excitons contribute the dominant share to the density of the condensate. Detailed information on the studies of the Bose condensation of dipolar excitons can be found in reviews [40, 42, 72–76].

It is noteworthy that the possibility of the Bose condensation of excitons in semiconductors was suggested and theoretically analyzed as early as the 1960s [77–82]. How-

<sup>2</sup> EHL luminescence lines in silicon were observed by Haynes [9] even before Keldysh formulated the concept of exciton condensation. However, Haynes interpreted these lines as recombination radiation of excitonic molecules (biexcitons). The correct interpretation was given in [10].

ever, numerous attempts to observe this remarkable phenomenon in bulk materials have been unsuccessful.

This brief outline of research on electron–hole bilayers is given here for the sake of completeness. The main subject of this review is the real-space condensation of an exciton gas leading to the formation of liquid phases. Some of the experimental studies of electron–hole bilayers carried out in this area to date are considered in Section 3.

## 2. Electron–hole liquid in semiconductors

### 2.1 Density and binding energy of the electron–hole liquid

It is known that an electron and a hole can bind together in a semiconductor due to Coulomb attraction to form a large-radius, or Wannier–Mott exciton. The ground-state energy  $E_{\text{ex}}$  and the effective Bohr radius  $a_{\text{ex}}$  of the Wannier–Mott exciton are given by expressions similar to the well-known Bohr formulas:

$$E_{\text{ex}} = -\frac{1}{2} \frac{m^* e^4}{\kappa^2 \hbar^2}, \quad a_{\text{ex}} = \frac{\kappa \hbar^2}{m^* e^2}, \quad (1)$$

where  $e$  is the electron charge,  $\kappa$  is the static dielectric constant of the crystal,  $m^* = (m_e^{-1} + m_h^{-1})^{-1}$  is the reduced electron–hole effective mass, and  $m_e$  and  $m_h$  are the effective masses of electrons and holes. Coulomb interaction is considerably reduced inside a crystal due to the polarization of the medium, and the electron and hole effective masses are typically much smaller than the free-electron mass. Thus, the binding energy of excitons is 2–4 orders of magnitude lower than typical atomic energies, and their size considerably exceeds interatomic distances in the crystal.

Excitons in semiconductors can exist only at low temperatures ( $k_B T < |E_{\text{ex}}|$ ), when the rate of their thermal ionization is small. At these temperatures, there are virtually no excitons in thermal equilibrium because usually  $|E_{\text{ex}}| \ll E_g$  (where  $E_g$  is the semiconductor band gap), and excitation of the crystal is required to generate excitons. In most cases, the sample is pumped by light with a photon energy exceeding  $E_g$ . Electrons and holes produced by the optical excitation thermalize rapidly and bind together into excitons. At low excitation levels, an insulating ideal Bose gas of excitons with a relatively low density is formed in the crystal.

In many respects, excitonic systems behave like those composed of ordinary atoms. As the exciton gas density increases, interaction between excitons can lead to the formation of excitonic molecules (biexcitons) and the condensation of excitons (and/or biexcitons) into a liquid phase, representing a bound state of a macroscopically large number of particles.

We note two factors that lead to essential differences between excitonic and atomic systems. First, the effective masses of electrons and holes are usually of the same order of magnitude, which means that heavy particles like atomic nuclei are absent in the electron–hole system. For this reason, quantum effects, including quantum delocalization of particles, are pronounced. The amplitude of zero-point oscillations in an excitonic molecule is large and its dissociation energy is fairly low. Zero-point oscillations in the liquid state cause delocalization of electrons and holes over the entire volume occupied by the liquid. In other words, rather than being composed of excitons or biexcitons, the liquid phase represents a metallic state in which electrons and holes are collectivized [1, 83]. Second, both excitons and the EHL are nonequilibrium entities and have finite lifetimes.

We briefly discuss the calculation of the main thermodynamic parameters of the EHL, which are its density  $n_0$  and the energy per pair of particles (electron–hole pair)  $E_0$  in the ground state of the liquid. In the EHP, the total energy per pair of particles depends on its density  $n$  and can be expressed as

$$E(n) = E_{\text{kin}} + E_{\text{exch}} + E_{\text{corr}}. \quad (2)$$

At low temperatures ( $k_B T \ll E_F^{\text{e,h}}$ ), the electrons and holes are degenerate. In the case of parabolic dispersion relations, the mean kinetic energy per pair of particles in a three-dimensional plasma is  $E_{\text{kin}} = 3/5 (E_F^{\text{e}} + E_F^{\text{h}})$ , where the electron and hole Fermi energies are  $E_F^{\text{e,h}} = \hbar^2 k_F^2 / (2m_{\text{e,h}})$ . The magnitude of the Fermi wave vector is  $k_F = \pi(3n/\pi)^{1/3}$ , where spin degeneracy is taken into account. The last two terms in the right-hand side of Eqn (2) are responsible for the Coulomb potential energy. Although the plasma as a whole is locally neutral, there are spatial correlations in the mutual arrangement of particles that lead to a decrease in its total energy: in the immediate vicinity of each particle, there is a certain excess of oppositely charged particles. There are two separate physical mechanisms that cause these correlations (see, e.g., [11, 17]). The first is the Pauli principle, which forbids two identical particles with parallel spins to have the same location in space. The corresponding contribution to the Coulomb interaction energy, which is called the exchange energy, is given by

$$E_{\text{exch}} = -\frac{3e^2}{2\kappa} \left( \frac{3n}{\pi} \right)^{1/3}. \quad (3)$$

The second mechanism is of dynamic origin. Correlations of this type arise because of the response of the surrounding plasma to the electric field of each charged particle. The contribution to the total energy resulting from these correlations is called the correlation energy  $E_{\text{corr}}$ . Like the exchange energy,  $E_{\text{corr}}$  is negative in accordance with its physical meaning, and its absolute value increases with the plasma density.

Calculations indicate that the total energy per pair of particles in an EHP as a function of density, determined by Eqn (2), has a minimum at the equilibrium density  $n_0$ . This means that a dense EHP experiences self-compression or expansion until it fills the volume corresponding to the equilibrium density. Thus, this system behaves as a liquid (electron–hole liquid). It is a neutral quantum two-component Fermi liquid (in the simplest case), with the internal pressure of the degenerate plasma balanced by the Coulomb attraction forces. The energy per pair of particles in the ground state of the liquid is  $E_0 \equiv E(n_0)$  at  $T = 0$ .

The chemical potential of the plasma is

$$\mu(n) = \frac{\partial [NE(N/V)]}{\partial N} = E(n) + n \frac{\partial E(n)}{\partial n}, \quad (4)$$

where  $N = nV$  is the total number of pairs in a volume  $V$ . In an EHL,  $n = n_0$  and  $\partial E / \partial n = 0$ , and hence  $\mu(n_0) \equiv \mu_0 = E_0$ . The renormalized band gap in the part of the crystal occupied by the EHL is

$$\begin{aligned} E_{\text{gL}} &= E_g + \mu_0 - (E_F^{\text{e}} + E_F^{\text{h}}) \\ &= E_g + \left( E_{\text{exch}} + E_{\text{corr}} - \frac{2}{3} E_{\text{kin}} \right) < E_g, \end{aligned} \quad (5)$$

where  $E_g$  is the band gap in the unperturbed crystal.

The value of  $E_0$  is the minimum energy required to remove an electron–hole pair from the liquid and to separate the electron and hole by an infinite distance from each other. As was already said, at low density, the electron–hole system represents a gas of excitons and excitonic molecules. If the energy  $E_0$  (we note that  $E_0 < 0$ ) exceeds the energy per pair of particles in the biexciton, then, even for  $T \rightarrow 0$ , the lowest-energy state of the system is a gas of biexcitons, and condensation into a liquid is impossible (at least for  $n \ll n_0$ ). In the opposite case, it is the liquid state that is thermodynamically stable and for any value of the average density of electron–hole pairs (i.e., the density averaged over the entire available volume rather than just over the volume occupied by the liquid), the EHL is the ground state of the system. Because the dissociation energy of excitonic molecules is low, they can be disregarded in many cases.<sup>3</sup> In the following discussion, we therefore assume that electrons and holes can bind only into excitons or EHL, as is actually observed in most experiments. It can then be assumed that the EHL is stable with respect to the breakup into free excitons if the binding energy per pair of particles in the liquid (the exciton work function in the EHL) is  $\varphi_0 = E_{\text{ex}} - E_0 > 0$ , where  $E_{\text{ex}}$  is given by Eqn (1).

The described procedure for the calculation of the EHL ground-state energy and density carried out taking the multivalley structure of the conduction band into account was first used by Pokrovskii and Svistunova [85] and by Kaminskii et al. [86] for the EHL in germanium and silicon, respectively. The foundations of the quantitative theory of EHL were laid by Brinkman et al. [87], Combescot and Nosieres [88], Brinkman and Rice [89], and Vashishta et al. [90]. The theoretical results are described and analyzed in review papers [11, 14, 19, 91], where theory is also compared with numerous experimental data (see also review [12]).

We now turn to experimental results. The EHL binding energy and density have been measured in numerous experiments, described in detail in reviews listed in the Introduction. Among the techniques used to determine these parameters, the one based on the analysis of the shape of the EHL luminescence spectrum stands out as the most informative. An analysis of the shape of the EHL emission spectrum of Ge and Si was first carried out in [85, 86]. Later, this method was widely used, in particular, to investigate the EHL in other semiconductors. Typically, the lineshape of the EHL recombination radiation in indirect-gap semiconductors is approximated by the expression

$$I(\hbar\omega) \propto \iint D_e(E_e) D_h(E_h) f_e(E_e) f_h(E_h) \times \delta(E_e + E_h + E_{\text{gL}} - \hbar\Omega - \hbar\omega) dE_e dE_h, \quad (6)$$

where  $D_e$  and  $D_h$  are the respective densities of states in the conduction and valence bands,  $f_e$  and  $f_h$  are the Fermi distribution functions of electrons and holes,  $E_e$  and  $E_h$  are the electron and hole energies referenced to the edges of the corresponding bands in the liquid,  $E_{\text{gL}}$  is the renormalized band gap [determined by Eqn (5)] in the volume of the crystal occupied by the liquid, and  $\Omega$  is the frequency of the phonon

<sup>3</sup> The role of biexcitons and their effect on the thermodynamics of the gas–liquid phase transition in electron–hole systems, as well as many other related problems remaining beyond the scope of this review (dielectrization of the electron spectrum of the liquid, Bose condensation of biexcitons, Mott transition, etc.), are discussed in reviews [11, 16, 83, 84].

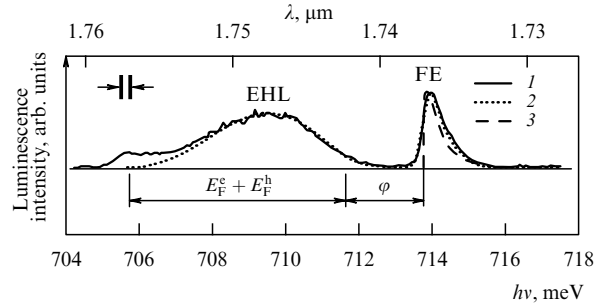


**Figure 1.** Longitudinal acoustic phonon components of the EHL and free-exciton (FE) luminescence spectrum in germanium at  $T = 3.04$  K: (1) experiment, (2) and (3) respective theoretical fits with and without taking the finiteness of the spectrometer slit into account (from [92]).

emitted in the electron transition. The emission of a phonon in the recombination act is required for the quasimomentum conservation in the crystal; at low temperatures, the probability of recombination accompanied by phonon absorption is extremely low. Expression (6) takes the complicated structure of the crystal energy bands into account in the electron and hole density-of-states effective masses.

We recall that germanium and silicon are indirect-gap semiconductors: unlike the valence-band maximum, the conduction-band minima in these materials occur away from the center of the Brillouin zone (there are four equivalent minima on the  $\langle 111 \rangle$  axes in Ge and six equivalent minima on the  $\langle 100 \rangle$  axes in Si). Therefore, their luminescence spectra consist of several phonon replicas. The most intense lines of the exciton and EHL luminescence in germanium and silicon are related to the radiative recombination processes occurring with the emission of respective longitudinal acoustic (LA) and transverse optical (TO) phonons.

The EHL density is determined as the value  $n_0$  corresponding to the best fit of the calculated lineshape of the EHL emission in Eqn (6) to the experimental one (Fig. 1). Next, we can obtain the electron and hole Fermi energies and the exciton work function  $\varphi$  in the EHL (as is shown in Fig. 1) at the temperature corresponding to the measurement conditions. To determine  $\varphi_0$ , we need to measure the temperature dependences of these quantities and extrapolate them to  $T = 0$  [93]. We note that in order to obtain the energy  $E_0$  per electron–hole pair in the ground state of the liquid, it is necessary to measure the exciton ground-state energy  $E_{\text{ex}}$  independently (the corresponding experiments are discussed in reviews [11] and [12]). The numerical values of  $n_0$ ,  $\varphi_0$ ,  $E_0$ , and  $E_{\text{ex}}$  for Ge and Si, taken from [12], are listed in the table.

**Table.** Thermodynamic parameters of the EHL in unstrained and highly compressed germanium and silicon.\*

Parameter	Ge	Si	Ge	Si
	$P = 0$	$P = 0$	$P \parallel \langle 111 \rangle$	$P \parallel \langle 100 \rangle$
$E_{\text{ex}}$ , meV	−4.17	−14.7 ± 0.4	−2.33	−12.8
$\varphi_0$ , meV	1.8 ± 0.2	8.2 ± 0.1	0.65	2.0
$E_0$ , meV	−6.0 ± 0.2	−22.9 ± 0.5	−2.98	−14.8
$n_0$ , 10 <sup>17</sup> cm <sup>−3</sup>	2.38 ± 0.05	33.3 ± 0.5	0.274	4.5
$T_c$ , K	6.5 ± 0.1	25 ± 5	3.5	13
$n_c$ , 10 <sup>17</sup> cm <sup>−3</sup>	0.8 ± 0.2	12 ± 5	0.077	1.5

\*  $E_{\text{ex}}$  — exciton ground state energy;  $E_0$  — EHL ground state energy;  $\varphi_0$  — work function of excitons in the EHL;  $n_0$  — EHL density;  $n_c$  — EHL critical density;  $T_c$  — critical temperature of the transition.

To conclude the discussion of EHL luminescence spectroscopy, we note that by relying upon the Fermi energy distribution for electrons and holes in the EHL in expression (6), we actually make an assumption about the metallic nature of the liquid in the calculation of the emission lineshape. Good agreement between theoretical and experimental shapes of the EHL luminescence spectra in germanium and silicon gives evidence of the validity of this assumption.

The metallic properties of the EHL manifest themselves in many other experiments of different kinds. For example, the metallic nature of the EHL determines its electric and electromagnetic properties (metallic conductivity, excitation of plasma oscillations, magneto-oscillation effects, efficiency of the scattering of infrared radiation by EHL drops, etc.), which are considered in detail in review articles [94] and [95], as well as in monograph [15].

Here, we only discuss the investigation of resonance absorption of EHDs in the submillimeter spectral range [7]. Measurements of the transmission spectra of photoexcited Ge at temperatures below 2 K revealed a broad absorption band peaking at  $\hbar\omega \approx 9$  meV, due to the excitation of plasma oscillations in the EHL droplets. Plasma resonance occurs in the absorption when the size of the particles is much smaller than the wavelength of the electromagnetic radiation. In this case, for spherical metallic particles, the absorption has a peak at the frequency  $\omega = \omega_{\text{pl}}/\sqrt{3}$ , where  $\omega_{\text{pl}} = [4\pi e^2 n_0 / (km^*)]^{1/2}$  is the plasma frequency and  $m^*$  is the reduced effective mass of electrons and holes. Thus, the EHL density can be found from the measured value of the resonance frequency.

Another indication of the metallic (Fermi-liquid) nature of the EHL is the observation of oscillations, periodic in the reciprocal magnetic field, in the integrated intensities of EHL luminescence [96] and far-infrared resonance absorption by the EHL [97] in Ge, which are similar to de Haas–van Alphen and Shubnikov–de Haas oscillations. These oscillations occur as the Fermi level of electrons bound to the EHL is crossed by successive Landau levels with an increase in the magnetic field and, according to [98], originate from oscillations in the liquid density. The calculation results obtained in [98] were corroborated by the experiments in [99, 100], where the corresponding oscillations were observed in the width of the EHL luminescence line (determined by the sum of the electron and hole Fermi energies; see Fig. 1) and in the lifetime of electron–hole pairs in the liquid (on recombination in the EHL; see Section 2.6). The EHL properties in a magnetic field are considered in more detail in [11, 12, 14, 15, 17, 94, 95]. Review [101] is entirely devoted to the thermodynamic properties of the EHL in a magnetic field.

We note that in the early 1970s, some researchers adhered to a different view of the nature of the EHL luminescence line in germanium, which they interpreted as a line related to emission from biexcitons [102]. At that time, this issue provoked fairly heated debates, which have only historical importance now.

## 2.2 Stability of the electron–hole liquid

The EHL can exist if it is stable with respect to dissociation into free excitons, i.e., if the exciton work function  $\varphi_0 = E_{\text{ex}} - E_0 > 0$  (see Section 2.1). We consider the factors that serve to stabilize the condensed state of electrons and holes in semiconductors.

Theoretical calculations indicate that the EHL in covalent direct-gap semiconductors with an idealized band structure

(i.e., with isotropic, parabolic, and nondegenerate electron and hole bands) is unstable [11, 12, 14, 16, 19, 83, 91] and, at low densities ( $na_{\text{ex}}^3 \ll 1$ ), the nonequilibrium electron–hole system in the ground state is a gas of noninteracting excitons. In polar semiconductors (GaAs, CdTe, etc.), the Coulomb electron–hole interaction is retarded owing to the inertia of ions. Therefore, calculations of the energy of this interaction must take the frequency dependence of the dielectric function into account (the interaction of electrons and holes with longitudinal optical phonons). Then the ratio of the energy per pair of particles in the ground state of the liquid to the exciton binding energy increases and the condensed state becomes stable already for a low degree of ionicity of chemical bonds in the crystal [103, 104].

The most significant factors affecting the stability of the EHL are the anisotropy and degeneracy of the electron spectrum. If, for a given density of the liquid, the electron or hole density of states is increased, the average kinetic energy of particles in the liquid decreases, while the potential energy, whose value is determined by the EHL density, remains nearly unchanged. The balance between the attraction and repulsion forces is affected, and the liquid experiences self-compression until the balance is restored with some higher values of its density and ground-state energy per electron–hole pair. In semiconductors with a degenerate and especially multivalley electron spectrum, the density of states is noticeably higher than it is in a semiconductor with an idealized band structure for the same values of  $m_e$  and  $m_h$ . In multivalley semiconductors (Ge, Si, GaP, etc.), the electron density of states is directly proportional to the number of equivalent minima in the conduction band. At the same time, the exciton binding energy is independent of the number of valleys, because each exciton belongs to a certain valley. Thus, the multivalley nature of the electron spectrum leads to considerable enhancement of the EHL stability [6]. It can be seen from similar reasoning (see [83]) that the degeneracy of the valence-band maximum and the anisotropy of the electron spectrum also represent stabilizing factors. Under certain conditions in highly anisotropic (e.g., quasi-one- and quasi-two-dimensional) electron–hole systems, an ‘ultra-dense’ ( $n_0 \gg a_{\text{ex}}^{-3}$ ) EHL can exist with a ground-state energy considerably exceeding (in absolute value) the exciton binding energy [20].

External perturbations that modify the electron spectrum of a crystal can either stabilize or destabilize the EHL. Uniaxial strain applied to the crystal leads to the lifting of degeneracy at the valence-band maximum and, in multivalley semiconductors, to a relative energy shift of the conduction-band minima (see, e.g., [105]). In typical experiments, a uniform compressive stress is applied to the sample under study along some high-symmetry crystallographic direction. Figure 2 shows variations in the energies of conduction-band minima in Ge under uniaxial compressive strain along the  $[1\bar{1}0]$  axis. The strain causes a shift of the conduction-band bottom as a whole by an energy  $\delta_c$ , while the pairs of minima that remain equivalent with respect to the strain axis shift in opposite directions by the energy  $\Delta_c/2$ . Electrons bound into the liquid are transferred to unoccupied lower-lying states, i.e., the upper pair of minima is emptied and the lower pair of minima becomes additionally populated (see Fig. 2b). Thus, the electron Fermi energy increases, the liquid expands, and the absolute value of its ground-state energy and the binding energy (work function) decrease.

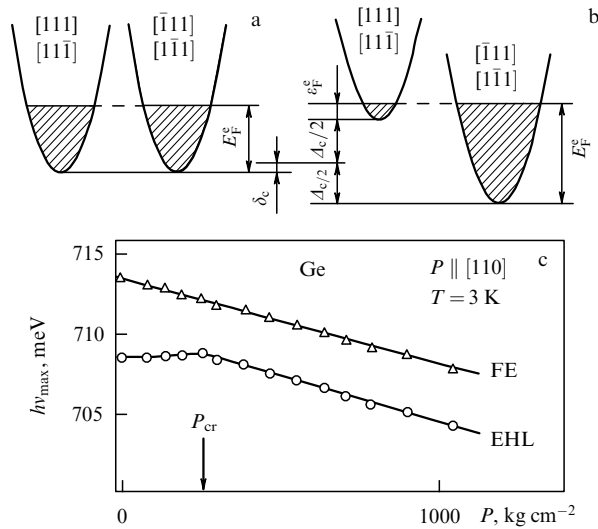


**Figure 2.** (a, b) Redistribution of electrons between the conduction-band minima in Ge under uniaxial compressive strain in the  $[1\bar{1}0]$  direction ( $P < P_{cr}$ ). Occupied states in an (a) unperturbed and (b) strained crystal are indicated by hatching.  $\delta_c$  and  $\Delta_c$  are not shown to scale. Minima that are equivalent with respect to the compression axis are shown as a single one in this schematic diagram. (c) Dependences of the peak spectral positions of the free exciton (FE) and EHL luminescence lines on the compressive stress applied along the  $[110]$  axis (from [106]).

Experimental data from [106] are shown in Fig. 2c. Because the exciton binding energy is virtually independent of strain, the linear shift of the exciton line peak reflects a reduction in the band gap with increasing the uniaxial compressive stress  $P$ . For  $P < P_{cr}$ , the energy spacing between the line peaks and hence the exciton work function in the EHL decrease with increasing the magnitude of stress. When  $P$  approaches  $P_{cr}$ , all electrons bound to the EHL appear in the two lowest minima of the conduction band (Fig. 2b) and, with a further increase in the stress, the peaks of the EHL and exciton luminescence lines shift at equal rates, which means that the EHL binding energy remains unchanged [106–108].

The magnitude of the splitting of the conduction-band bottom  $\Delta_c$  and hence the value of  $P_{cr}$  depend on the crystallographic orientation of the stress axis. For a given  $P$ , the splitting is largest when the stress is applied along crystallographic directions corresponding to those reciprocal-lattice axes where the conduction-band minima are located ( $\langle 111 \rangle$  directions in Ge and  $\langle 100 \rangle$  directions in Si). If the direction of uniaxial stress is chosen such that all minima remain equivalent (e.g., the  $\langle 100 \rangle$  direction in Ge), then  $\Delta_c = 0$ ; in this case, a reduction in the EHL density and binding energy occurs only due to the splitting of the top of the valence band.

The thermodynamic characteristics of the EHL in highly strained Ge (stressed along the  $\langle 111 \rangle$  axis) and Si (along the  $\langle 100 \rangle$  axis), taken from review [19], are listed in the table.

Due to a considerable reduction in the work function of excitons in the EHL in highly strained Si and Ge, the density of the exciton gas in equilibrium with the liquid at a given temperature increases considerably (see Section 2.3). At low temperatures, the gas phase can contain an observable amount of biexcitons, whose density is proportional to the exciton density squared. As a result, the emission line of biexcitons emerges in the luminescence spectra between the

exciton and the EHL lines [109, 110]. It is also noteworthy that electrons occupying different valleys in uniaxially strained crystals can be regarded as particles of different types. In this sense, the EHL in multivalley semiconductors is a multicomponent Fermi liquid. The application of uniaxial strain to the crystal allows changing the number of components in the EHL and their relative concentrations (see Figs 2a, b); thus,  $E_F^e$  and  $E_F^h$  in Fig. 2b are the Fermi energies of two different components of the EHL. These changes can lead to first-order phase transitions within the liquid [111]. More comprehensive information on the properties and behavior of the exciton-gas–EHL system in strain fields can be found in review papers cited at the beginning of this section and also in reviews [17, 112, 113], which are largely devoted to this topic.

In contrast to the strain field, a strong magnetic field acts to stabilize the EHL [20, 114–116]. The electron spectrum in a magnetic field is quasi-one-dimensional. In ultrahigh magnetic fields, the Landau level spacing  $\hbar\omega_c \gg |E_{ex}|$  (where the cyclotron frequency is  $\omega_c^{e,h} = eB/(cm_{e,h})$  and  $B$  is the magnetic field induction), all electrons and holes occupy the lowest Landau levels (the ultraquantum limit). In the absence of damping, the density of states near the electron and hole Landau band edges diverges inversely proportional to  $(E_k^{e,h})^{1/2}$ . Furthermore, the density of states grows as  $\propto B$ . Therefore, in a sufficiently high magnetic field, the Fermi energy decreases as  $\propto B^{-2}$  as the field increases. The calculations in [116] indicate that in an ultrahigh field, the dominant contribution to the attraction energy comes from the correlation energy, which is determined by correlations between particles on adjacent Landau cylinders. In this situation, an ‘ultradense’ EHL is expected to form: the liquid density becomes considerably greater than the reciprocal exciton volume ( $n_0 \gg (a_{ex}a_B^2)^{-1}$ , where  $a_B = [ch/(eB)]^{1/2}$  is the magnetic length). The density and the absolute value of the energy per electron–hole pair in the liquid ground state increase with the magnetic field as  $n_0 \propto B^{8/7}$  and  $|E_0| \propto B^{2/7}$ . We note that from the theoretical standpoint, the EHL in ultrahigh magnetic fields is formally equivalent to the EHL in a system of parallel wires [20].

Excitons in ultrahigh magnetic fields are highly anisotropic. The exciton shape becomes a rotation ellipsoid elongated in the direction of the field, with the longitudinal and transverse semiaxes respectively equal to  $a_{ex}$  and  $a_B$ . The exciton binding energy increases as  $\propto \ln B^2$  with the field (see, e.g., [117, 118]). Because the absolute value of the EHL ground-state energy increases with the magnetic field  $B$  at a higher rate than the exciton binding energy does, the EHL should become stable in a sufficiently strong field even if it is unstable in the absence of the field. The theory of the EHL in ultrahigh magnetic fields is considered in review [101]. This and some related issues are also discussed in reviews [16, 83].

A study of the luminescence spectra of the EHL in germanium in a magnetic field demonstrated that the liquid density increases with the field and becomes almost a factor of 5 higher in the field  $B = 19 \text{ T}$  (the highest field in those experiments) than in a zero field [119]. At the same time, the magnetic field did not affect the stability of the liquid state (the exciton work function). We note that the fields used in this study are not ultrahigh for Ge. Recently, a magnetically stabilized EHL was investigated in multivalley compound  $\text{Al}_x\text{Ga}_{1-x}\text{As}$  ( $x = 0.387$ ) in magnetic fields up to 90 T [120]. The authors observed an increase in the density and a decrease in the temperature of the EHL with an increase in the field.

The magnetic stabilization of the EHL was observed in highly compressed Ge, where the liquid is less stable than in the unstrained crystal (see the table). In the experiments in [121], the EHL emission line in Ge disappeared under compression in the absence of a magnetic field and reappeared in a magnetic field  $B > 4$  T. The liquid density and binding energy respectively increased threefold and twofold with a further increase in  $B$  in the range 5.5–14 T.

A magnetic-field-stabilized EHL was observed for the first time in indium antimonide [122–124]; this work is briefly reviewed in [125]. The exciton binding energy in InSb is extremely small ( $|E_{\text{ex}}| \approx 0.5$  meV), and therefore a magnetic field applied to this semiconductor can be considered ultrahigh for  $B \gg 0.1$  T. The EHL does not exist in InSb in the absence of a magnetic field. It appears for  $B > 2$  T; as the field increases from 2.3 to 5.5 T, the liquid density  $n_0$  increases from  $3.2 \times 10^{15}$  to  $6.7 \times 10^{15} \text{ cm}^{-3}$ , and the binding energy  $\varphi$  per electron–hole pair in the liquid increases from 0.4 to 1.2 meV. Measurements in InSb and in highly compressed Ge reveal the existence of a magnetically stabilized EHL whose thermodynamic parameters vary with the magnetic field in qualitative agreement with the theory [20, 116]. However, the EHL was not ‘ultradense’ in these experiments (the criterion  $n_0 \gg (a_{\text{ex}} a_B^2)^{-1}$  was not satisfied), and the theory cannot be applied for a quantitative description of the results (see [101, 125] for more details).

To conclude this discussion of EHL stability, we recall that the density of various kinds of electronic liquids is commonly characterized in the theory by a dimensionless parameter  $r_s$  that in the case of the EHL is expressed as  $r_s = [(4/3) \pi a_{\text{ex}}^3 n_0]^{-1/3}$ . For the EHL in Ge and Si,  $r_s = 0.5$  and 0.86, respectively. It is known that for electron Fermi liquids in metals,  $r_s \geq 1.88$ . Thus, the EHL in Ge and Si is characterized by the highest density among ‘earthly’ electron liquids. Moreover, EHL is the ‘most quantum’ of all known quantum liquids [12].

### 2.3 Phase diagrams

Similarly to conventional liquid–vapor systems, phase equilibrium in the exciton–gas–EHL system can be described graphically by diagrams. In the  $(n, T)$  plane, the region where the liquid and the gas phases coexist is bounded by two lines intersecting at the critical point  $(n_c, T_c)$ . On the liquid side, the boundary line follows the temperature dependence of the EHL density. On the gas side, the boundary line for conventional liquids follows the temperature dependence of the saturated vapor density, which, for a flat liquid–gas interface, can be written in our case as

$$n_{0T} = v_d \left( \frac{M_d k_B T}{2\pi \hbar^2} \right)^{3/2} \exp \left( -\frac{\varphi}{k_B T} \right), \quad (7)$$

where  $v_d$  is the ground-state degeneracy factor and  $M_d$  is the density-of-states effective mass of the exciton.

The thermodynamics of the exciton–gas–EHL system in the critical region is described fairly well by the theory, which yields values of the critical parameters (the density  $n_c$  and the temperature  $T_c$ ) that are close to the ones obtained experimentally for Ge and Si. Theoretical studies on this issue are reviewed and analyzed in [11, 19, 91]. Here, we address experimental results only.

In Section 2.1, we have already discussed the use of spectroscopic measurements to determine the EHL density. To obtain the gas branch of the phase diagram, threshold and

spectroscopic techniques are used. Here, we do not discuss spectroscopic measurements, but mention threshold measurements, which are more illustrative. In-depth consideration of experiments in which phase diagrams of the exciton–gas–EHL system in Ge and Si were established is given in reviews [12, 19].

It was established in the very first experiments that EHL lines in the luminescence spectra [5, 85] and the resonance absorption feature in the far-infrared spectral range [7] exhibit a threshold-type behavior as the excitation level is increased at a fixed temperature or as the temperature is reduced at a fixed excitation level. A plot of the exciton gas density, measured somehow at the EHL formation threshold, as a function of temperature represents the vapor line of the phase diagram. The work function determined according to expression (7) from dependences of this kind, which were measured in various types of threshold experiments (see, e.g., [126, 127]), turns out to be lower than the value of  $\varphi$  determined from spectroscopic data, as is described in Section 2.1. This is because the formation of the nuclei of the liquid phase requires some degree of supersaturation of the exciton vapor, which, similarly to conventional liquids, increases as the temperature decreases (see Section 2.5), but expression (7) describes the gas branch of the phase diagram under thermodynamic equilibrium conditions. Therefore, it is more appropriate to register thresholds corresponding to the disappearance of the liquid phase than to its formation [12, 128] (see Section 2.5). In this case, the observed deviation of the gas branch from dependence (7) at low temperatures is related to the nonequilibrium nature of the EHL. This behavior is especially pronounced in silicon. We can see in Fig. 3b that for  $T < 20$  K, dependence (7), plotted by the solid line, diverges from the experimental data.

Figure 3 shows phase diagrams for germanium [129, 130] and silicon [131] obtained from spectral measurements by registering the thresholds for the appearance of EHL luminescence, as outlined in the preceding paragraph. The critical parameters of the EHL in these semiconductors are listed in the table, along with the critical parameters of the EHL in highly compressed Ge [132] and Si [133, 134]. Under high compression, the gas phase in these materials can be of mixed atomic/molecular composition, i.e., it can contain biexcitons in addition to excitons (see Section 2.2). The critical parameters, along with the density and binding energy, are the main thermodynamic parameters of the EHL.

A subject of rather intense studies in recent years is the EHL in diamond [135–140], which features record-high thermodynamic parameters  $n_0 = (1-1.5) \times 10^{20} \text{ cm}^{-3}$ ,  $\varphi = 60-100$  meV,  $T_c \approx 170$  K, and  $n_c \approx 4 \times 10^{19} \text{ cm}^{-3}$ .

We have discussed the simplest type of phase diagram of the exciton–gas–EHL system. More complicated phase diagrams are possible if, in addition to the gas–liquid transition, other phase transitions can occur in the liquid or gas phases. Various possibilities are discussed in Keldysh’s papers [16, 83] and in review articles cited in this section.

### 2.4 Size and concentration of EHDs

At low temperatures ( $T < T_c$ ), the EHL density is considerably higher than the exciton gas density at equilibrium with the EHL and, in the range of optical excitation levels commonly used, the liquid occupies a small fraction ( $10^{-3}-10^{-2}$ ) of the volume of the excited region in the crystal. The very first experiments on resonance absorption

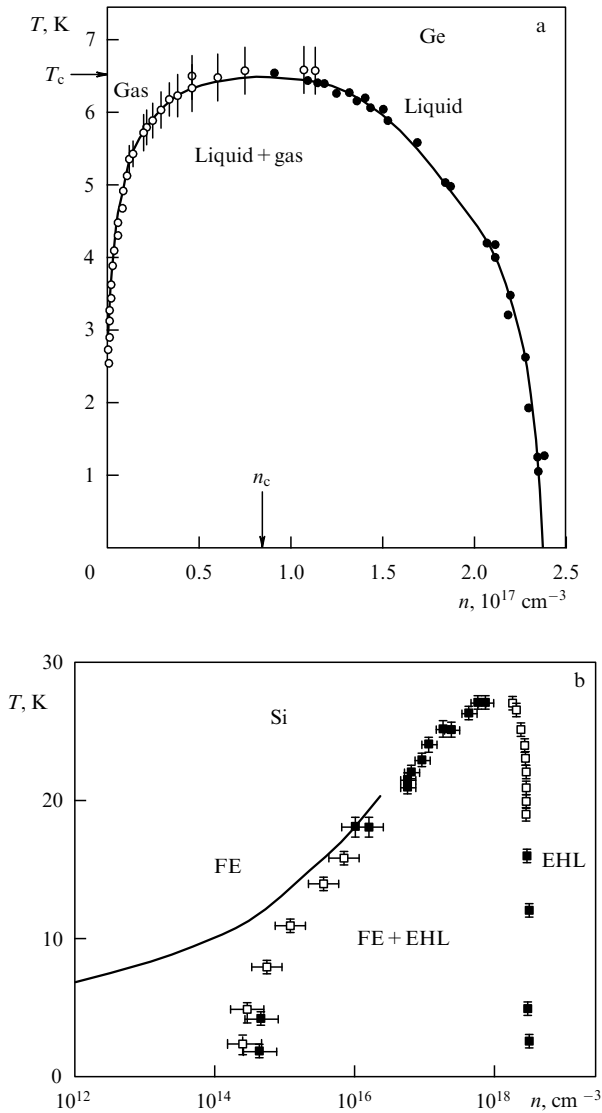


**Figure 3.** Phase diagrams of the exciton-gas–EHL system in (a) germanium [129, 130] and (b) silicon [131]. The solid line in panel b shows the gas branch of the phase diagram calculated according to Eqn (7).

in the far-infrared spectral range [7] produced evidence that the EHL in germanium appears in the form of EHDs several micrometers in size. The existence of EHDs also manifests itself in the observation of intense bursts of photocurrent through a p–n junction [141, 142]: the dissociation of an EHD entering the high-field region of the junction to free electrons and holes is accompanied by an abrupt increase in the current, whose magnitude is determined by the number of electron–hole pairs ( $10^7$ – $10^9$ ) in the drop. The most direct and convincing evidence of the existence of EHDs and detailed information about the size and concentration of drops under different experimental conditions were obtained in light-scattering experiments [143–146].

In scattering experiments, the excited region of the sample is probed by a laser beam (usually at a wavelength of  $3.39\ \mu\text{m}$ ) for which the crystal is transparent. The radius of scattering particles (EHDs) is deduced from the angular distribution of the scattered light intensity (scattering indicatrix). After the radius of EHDs is determined, their concentration can be found from measurements of the scattered light intensity (or

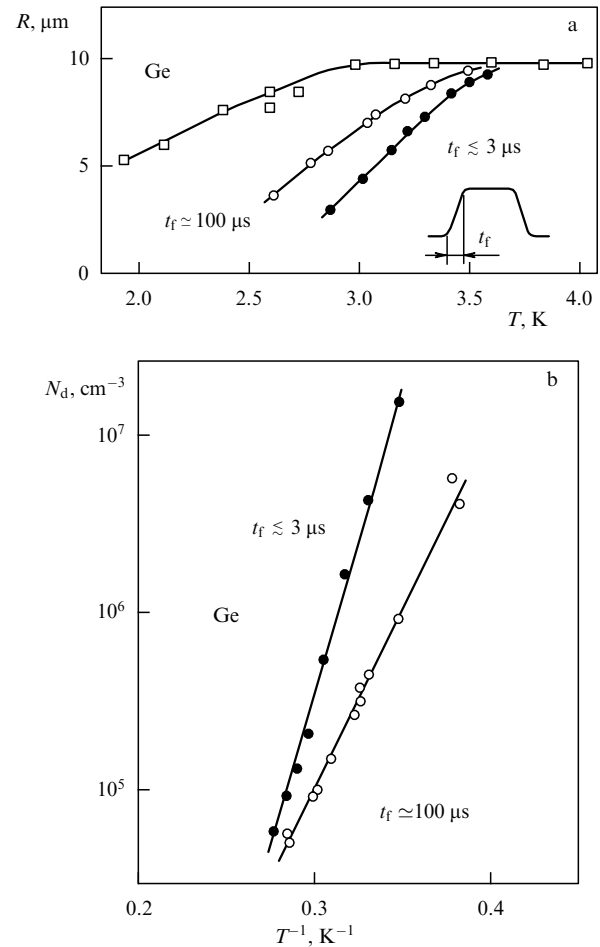


**Figure 4.** Temperature dependences of the (a) radius and (b) concentration of EHDs in germanium obtained under quasi-CW excitation with short- and long-edge pulses [148]. (a) The upper curve (squares) corresponds to a higher excitation level (the threshold temperature of condensation is  $T_{\text{th}} \approx 4.3\ \text{K}$ ). For the two lower curves,  $T_{\text{th}} \approx 3.55\ \text{K}$ . The inset shows the shape of the excitation pulses. The pulse duration is  $t_p = 500\ \mu\text{s}$ ; the pulse edge duration is  $t_f < 3$  and  $\approx 100\ \mu\text{s}$ . (b) The drop concentration was determined using the values of  $R$  corresponding to the two lower curves in panel (a).

probe beam absorption, which is recorded simultaneously with scattering) (see, e.g., [147]).

Experiments on light scattering demonstrated that both the size and concentration of drops depend on a number of factors: experiment configuration, excitation regime (pulsed or continuous-wave (CW), surface or bulk), etc. Here, we briefly consider the results obtained under CW bulk excitation, stressing some general features. Under typical experimental conditions, the EHD radius in germanium ranges between 1 and  $10\ \mu\text{m}$ , depending on the temperature and excitation level. Figure 4 shows the temperature dependences of the EHD radius and concentration [148]. The size of drops increases and their concentration decreases with increasing temperature. However, when the EHD radius grows as large as  $R \approx 10\ \mu\text{m}$ , it becomes independent of the temperature (Fig. 4a) and nearly independent of the excitation level (possible mechanisms limiting the EHD radius are considered in Section 2.9). At lower temperatures, the EHD radius can either increase (under the excitation by pulses with a slowly rising front) or decrease (pulses with a steep front) with



increasing the excitation level. Such a difference is related to the different behavior of the EHD concentration in this temperature range in the two cases [148]. It is shown in the next section that the EHD size and concentration are determined by the exciton condensation kinetics. In particular, at low temperatures, the size of drops is determined by their concentration and hence by the rate of liquid-phase nucleation. The EHD concentration depends on the rise time of the excitation pulses due to the relation between the nucleation rate and the exciton vapor supersaturation.

Data on the size and concentration of EHDs in Ge are reviewed much more comprehensively in [12, 14, 17]. Unfortunately, such information for EHDs in Si is virtually absent. From the magnitude of the photocurrent bursts in a p–n junction, the EHD radius in Si was estimated to be  $R \approx 0.75 \mu\text{m}$  at  $T \approx 2 \text{ K}$  [149]. Other indirect estimates yield even smaller values of  $R$ . Thus, EHDs in silicon are considerably smaller than in germanium.

## 2.5 Kinetics of exciton condensation

The condensation of any vapor into liquid begins with the formation of liquid phase nuclei capable of further growth (critical-radius nuclei). The subsequent growth of these nuclei proceeds until a vapor–liquid equilibrium is established. However, the nonequilibrium nature of the electron–hole system gives rise to a range of novel properties, manifested both in the condensation kinetics and in steady-state conditions, which conventional liquids do not have. In particular, the finiteness of the electron–hole pair lifetime in the liquid results in qualitative changes in the gas branch of the phase diagram (see Section 2.3).

The kinetics of exciton condensation has been the subject of numerous studies (see, e.g., [148, 150–157]), and was considered in reviews [11, 12, 14, 16–18, 83, 112, 128]. Here, we only briefly discuss the main features in the behavior of the exciton–gas–EHD system. The total number of electron–hole pairs in a spherical EHL drop of radius  $R$  varies according to the equation [85, 148]

$$\frac{d}{dt} \left( \frac{4}{3} \pi n_0 R^3 \right) = 4\pi R^2 \left[ n(R) - n_{0T} \exp \left( \frac{2\sigma}{n_0 R k_B T} \right) \right] v_T - \frac{4}{3} \pi R^3 \frac{n_0}{\tau_0}, \quad (8)$$

where  $n(R)$  is the density of excitons in the vicinity of the drop surface (which, in general, differs from the average exciton–gas density  $n$  in the bulk of the sample but can be expressed through it), the saturated vapor density  $n_{0T}$  is given by Eqn (7),  $v_T$  is the mean thermal velocity of excitons,  $\sigma$  is the surface tension coefficient of the EHL, and  $\tau_0$  is the electron–hole–pair lifetime in the EHL. The first term in the right-hand side of this equation represents the difference between the rates of exciton capture and evaporation from the drop, and the second term accounts for particle recombination within the drop.

The steady-state ( $dR/dt = 0$ ) solution of Eqn (8) yields a relation between the exciton gas density  $n$  and the radius  $R$  of a drop in equilibrium with the gas. This solution has two branches. The one descending with increasing  $R$  is unstable (for  $\tau_0 \rightarrow \infty$ , it is described, similarly to conventional liquids, by the second term in square brackets in Eqn (8)): upon a small random deviation of  $n$  or  $R$  from the values corresponding to this branch, the drop evaporates or starts to grow. Such drops are called critical nuclei. The growth of the drop

continues until  $n$  and  $R$  reach the values corresponding to one of the points on the ascending, stable branch of the  $n(R)$  relation.

The occurrence of the ascending branch of this relation is a characteristic feature of phase equilibrium in a system with a finite lifetime of particles in the liquid and is related to the last term in the right-hand side of Eqn (8): an increase in the exciton density with increasing  $R$  ensures that the flux of excitons onto the drop surface increases, and their condensation compensates the reduction in the number of electron–hole pairs within the drop caused by recombination. Due to the existence of this branch, there is a minimum in the  $n(R)$  relation. The lowest exciton gas density for which the existence of EHDs in stable equilibrium with the exciton gas is possible exceeds the density corresponding to thermodynamic equilibrium ( $n_{\min} > n_{0T}$ ). The relative excess  $(n_{\min} - n_{0T})/n_{0T}$  of the minimum exciton density over the thermodynamically equilibrium one increases with decreasing the temperature. Hence, as was mentioned in Section 2.3, the gas branch of the phase diagram is not correctly described by expression (7) in the low-temperature region.

To find  $n$  and  $R$  at given experimental conditions, determined by the temperature and the excitation level, a steady-state solution of Eqn (8) has to be complemented with an equation describing particle-number conservation in the system. In a steady state, this equation can be written as

$$g = \frac{n}{\tau} + \frac{4\pi R^3 n_0 N_d}{3\tau_0}, \quad (9)$$

where  $\tau$  is the exciton lifetime and  $N_d$  is the concentration of the drops. This equation simply states that the generation rate  $g$  is equal to the net rate of recombination in the gas and liquid phases. The combined solution of Eqns (8) and (9) yields the critical nucleus radius for a given exciton density and the steady-state EHD radius, which depends on the EHD concentration. At low temperatures and high excitation levels, recombination proceeds mainly in the liquid phase, and the second term in (9) is much greater than the first. In this case,  $R \approx [3g\tau_0/(4\pi n_0 N_d)]^{1/3}$ . Under the reverse relation between the recombination rates (high temperatures,  $n$  only slightly exceeding  $n_{\min}$ ), we have  $n \approx g\tau$ , and the drop radius is independent of  $N_d$ .

To complete the argument, we consider factors that determine the concentration of drops. It is known from the classical theory of condensation (see, e.g., [158]) that the concentration of drops is determined by the probability of fluctuations leading to the formation of critical nuclei:

$$\frac{dN_d}{dt} \propto n^2 \exp \left( -\frac{4\pi\sigma R_{\text{cr}}^2}{3k_B T} \right), \quad (10)$$

where  $R_{\text{cr}}$  is the critical nucleus radius, which in the case of a sufficiently large supersaturation  $\Delta n = n - n_{0T}$  (and  $n > n_{\min}$ ) can be expressed as  $R_{\text{cr}} \approx 2\sigma/[n_0 k_B T \ln(n/n_{0T})]$ , a formula valid under the conditions of thermodynamic equilibrium. We can see from Eqn (10) and the expression for  $R_{\text{cr}}$  that the rate of critical nuclei formation increases abruptly with an increase in the exciton vapor supersaturation. In particular, for a given generation rate, the degree of supersaturation and hence the concentration of drops increase as the temperature decreases, in agreement with the experimental data shown in Fig. 4b. These formulas also show that the relative supersaturation  $\Delta n/n_{0T}$  required to sustain a given critical nuclei formation rate increases as the temperature decreases. This

leads to a low-temperature discrepancy between the gas branch of the phase diagram determined from the measurements of the EHL formation thresholds and the dependence given by Eqn (7), which corresponds to thermodynamic equilibrium (see Section 2.3).

The effects of supersaturation are most pronounced in experiments on optical hysteresis, which was discovered in [159]. A detailed discussion of these experiments can be found in review [128]. When the excitation power  $P$  is increased gradually, such that a steady state is established at each value of  $P$ , the EHL luminescence appears as the power approaches a threshold value  $P_+$  (Fig. 5). A further increase in  $P$  results primarily in the formation of new EHDs and, to a lesser extent, in the growth of existing ones; thus, the EHL luminescence intensity increases. If  $P$  is increased to some peak value and is then gradually reduced, the concentration of EHDs does not change, while their radii start to decrease. The EHL luminescence disappears at  $P = P_- < P_+$ , when the drop radii decrease to a value close to  $R_{\min}$ .

The dependence of the size and concentration of EHDs on the steepness of the front of excitation pulses (see Section 2.4) is another manifestation of supersaturation effects. Hysteresis phenomena, in which the system keeps a memory of its preceding history, are typical of first-order phase transitions. However, the uniqueness of the EHL lies in the fact that billions of generations of its constituent particles, created long after the EHDs have been formed (several hours in some experiments), ‘remember’ the initial nucleation conditions.

The critical nucleus formation rate (10) highly depends on the surface tension coefficient of the EHL. In germanium, the surface tension coefficient was determined from measurements of the temperature dependence of the EHD concentration [160, 161, 148], the analysis of the optical hysteresis thresholds [153, 157], and other methods. At  $T = 0$ , the surface tension is  $\sigma = (2.6 \pm 0.3) \times 10^{-4}$  erg cm $^{-2}$  (see review [128]). The results of theoretical calculations of surface tension (see reviews [11, 91] and the references therein) for the EHL in germanium are in satisfactory agreement with the experimental data. For reference, the EHL surface tension in silicon is  $\sigma \approx 2 \times 10^{-3}$  erg cm $^{-2}$  [162].

We note that at sufficiently low temperatures ( $T \leq 1.4$  K for Ge), condensation can occur in the absence of supersaturation. Under these conditions, there is no hysteresis [83, 128]. Most likely, in this case, the nucleation of EHDs is triggered by multiexciton–impurity complexes (at least in silicon) [86, 163, 164].

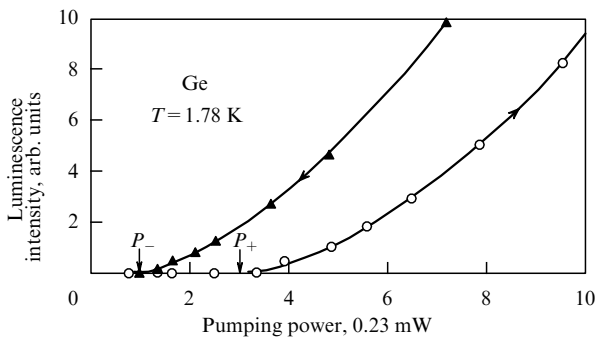


**Figure 5.** Hysteresis in the EHD luminescence in germanium. The pump power increases steadily from zero to 7.5 mW (outside the plot frame) and then decreases back to zero. The total time of the cycle is 192 s [159].

The picture of the exciton condensation kinetics outlined in this section provides an explanation of almost all experimental results obtained in studies of the dependences of the EHD concentration and radius on temperature and the amplitude and front duration of excitation pulses described in Section 2.4, except a bound on the drop radius at around  $R \approx 10$   $\mu\text{m}$ . Possible mechanisms responsible for this bound are apparently related to phonon-wind effects (Section 2.9).

At the same time, the above picture corresponds to relatively low excitation levels. High-power pulsed pumping initially produces a dense EHP, and EHDs and excitons start to form only after the EHP density decreases in the course of recombination to the Mott density or the EHL density. In silicon, this delay can be as long as several hundred picoseconds [165]. However, exciton correlations exist in the EHP even at densities exceeding the Mott threshold [165, 166]. Experiments under pulsed pumping are discussed in reviews cited at the beginning of this section.

## 2.6 Recombination kinetics

We consider the behavior of the two-phase nonequilibrium exciton–gas–EHD system after excitation is turned off. The kinetics of recombination in this system is described by Eqn (8), complemented by the continuity equation for the rate of the variation of the exciton gas density with the capture and escape of excitons from EHDs (the first term in Eqn (8) multiplied by  $N_d$ ) and the annihilation of excitons owing to the recombination of constituent electrons and holes taken into account [85, 148]. It is implied that as the system returns to equilibrium, the concentration of drops remains unchanged ( $N_d = \text{const}$ ). Instead of writing this equation, we consider the example of the gas–liquid system in germanium ( $\tau_0 \gg \tau$ , where  $\tau$  is the exciton lifetime) and discuss several specific cases that allow clarifying the main features of the recombination process.

At low temperatures, when exciton evaporation from the surface of the drops can be disregarded, the drop radius and hence the volume of the liquid phase (which is proportional to  $R^3 N_d$ ), decrease primarily due to the recombination of electrons and holes in the liquid. In this case, it follows from Eqn (8) that

$$\begin{aligned} R(t) &\approx R(0) \exp\left(-\frac{t}{3\tau_0}\right), \\ R^3(t)N_d &\approx R^3(0)N_d \exp\left(-\frac{t}{\tau_0}\right), \end{aligned} \quad (11)$$

where  $R(0)$  is the initial EHD radius. The exciton gas density  $n$  then first decreases from its initial value  $n(0)$  exponentially with a time constant  $\tau$ , and then, at times  $t \gg \tau$ , decreases less rapidly (as the total surface area of the EHDs), its value being determined by the rate of slow evaporation of the drops.

At higher temperatures, the rate of drop evaporation becomes comparable to the electron–hole recombination rate in the liquid. Disregarding the backward flux of excitons onto the drop surface we obtain

$$\begin{aligned} R(t) &\approx R(0) \exp\left(-\frac{t}{3\tau_0}\right) \\ &\quad - 3 \frac{n_{0T}}{n_0} v_T \tau_0 \left[1 - \exp\left(-\frac{t}{3\tau_0}\right)\right], \end{aligned} \quad (12)$$

from Eqn (8). In this case, the EHD radius decreases non-exponentially with time and vanishes at some moment  $t_c$  [126].

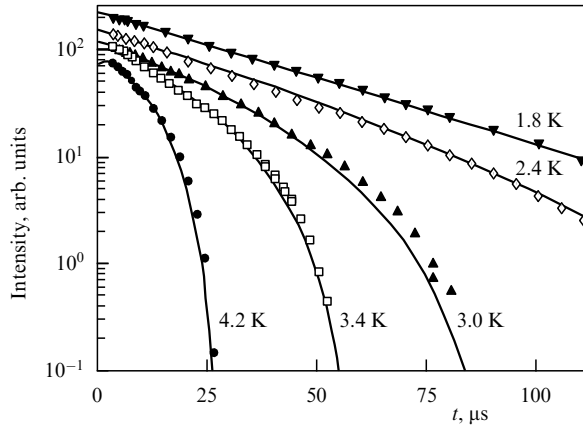


**Figure 6.** EHD luminescence kinetics in ultrapure germanium after excitation with an 80 ns pulse from a GaAs laser (pulse energy 30 erg; diameter of the laser spot at the sample surface  $\approx 0.6$  mm) at various temperatures (indicated next to each curve) [167].

Thus, the initial radius of the drops can be determined from the measurements of  $t_c$ .

The kinetics of the EHD luminescence in germanium measured in [167] is shown in Fig. 6 (references to other experiments and the corresponding discussion can be found in reviews [12, 128, 163]). From the slope of the kinetic curve recorded at  $T = 1.8$  K, we can obtain the electron-hole pair lifetime in the liquid  $\tau_0 = 36$   $\mu$ s. In qualitative agreement with Eqn (12), the total decay time of the EHD luminescence  $t_c$  decreases with increasing the temperature. However, evaluating  $R(0)$  in accordance with Eqn (12) is less straightforward [12, 17]. This procedure can be used only at relatively low levels of pulsed excitation, in which case it yields reasonable values of  $R(0)$  [126, 168] that agree with the results obtained by other methods [169, 170].

As the intensity of pulsed excitation is increased (and hence supersaturation also increases), the concentration of drops increases steeply, according to Eqn (10). Then the rate of the exciton capture by the surface of the drops can become higher than the rate of exciton annihilation. In this collective relaxation regime (where excitons appearing upon the evaporation of the drops are recaptured by them prior to annihilation), measurements of the cutoff time yield the total number of electron-hole pairs in the liquid phase (the volume of the liquid) immediately after an excitation pulse, rather than the initial radius of the EHDs  $R(0)$  (as is the case in the regime of independent annihilation) [171]. The results presented in Fig. 6 were obtained under these conditions. In this situation, excitons are in quasi-equilibrium with the EHDs, and, in the course of the decay of the drops, the exciton concentration  $n \approx n_{0T}$  remains nearly constant (more exactly, it decreases much more slowly than the volume of the liquid phase) for a fairly long period  $t \approx (2-3) \tau_0$  [167, 172, 173] (Fig. 7).

Until now, we have implicitly assumed that all EHDs are of the same size. Actually, this is incorrect for high excitation levels. The size distribution of the drops follows a power law:  $f(R) \propto R^{-\nu}$ , where  $\nu$  can vary from 3 to 6 (for Ge) depending on the experimental conditions [170, 175]. Thus, small drops account for a noticeable fraction of the total EHL volume, and evaporation can substantially contribute to the total rate of decay of the volume of small drops even at low temperatures ( $T \leq 2$  K).

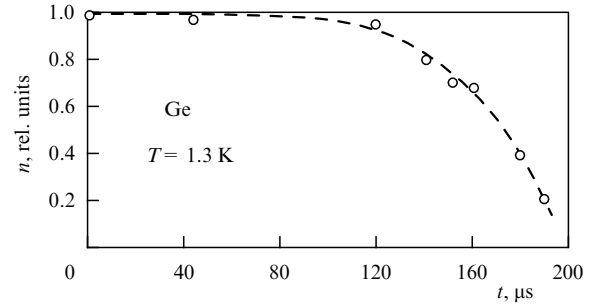


**Figure 7.** Exciton gas density in germanium as a function of time after an excitation pulse generating  $\approx 10^{15}$   $\text{cm}^{-3}$  electron-hole pairs. At  $t \approx 120$   $\mu$ s  $\gg \tau_0$ , the collective mode gives way to the independent EHD decay mode. The exciton concentration was determined from the change in high-frequency conductivity caused by the occurrence of free charge carriers upon pulsed microwave breakdown of excitons [173, 174].

The electron-hole pair lifetime in the EHL in germanium, determined from experiments of the kind described above, is  $\tau_0 = 36-40$   $\mu$ s. Typical exciton lifetimes in different samples are  $\tau = 2-9$   $\mu$ s (see reviews [12, 128, 163]). The particle recombination rate in the liquid is  $\tau_0^{-1} = \tau_r^{-1} + \tau_A^{-1}$ , where  $\tau_r^{-1} \propto n_0$  is the radiative recombination rate and  $\tau_A^{-1} \propto n_0^2$  is the nonradiative Auger recombination rate. The quantum efficiency of EHL luminescence in Ge is  $Q = \tau_0/\tau_r \approx 25\%$  [176]. In silicon, the EHL density  $n_0$  is greater than in germanium by more than an order of magnitude (see the table). Therefore, for the EHL in Si, the Auger recombination rate  $\tau_A^{-1} \gg \tau_r^{-1}$ , and the quantum efficiency  $Q \sim 5 \times 10^{-4}$  is very low [177]. The lifetime of electron-hole pairs in the liquid and that of excitons are respectively  $\tau_0 \approx 0.15$   $\mu$ s and  $\tau = 2-5$   $\mu$ s [177-181].

Thus, in contrast to germanium, in silicon we have  $\tau_0 \ll \tau$  and EHDs decay faster than excitons. Hence, the recombination kinetics in the exciton-gas-EHL system in silicon differs qualitatively from the picture of kinetic processes outlined above for germanium [12, 14, 17, 19, 128, 163].

## 2.7 Motion of EHDs under external forces

Because the charge carriers bound into the EHDs are Fermi degenerate, their scattering by lattice vibrations and crystal-structure defects is strongly suppressed; only electrons and holes in the energy intervals of width  $\approx k_B T \ll E_F^{e,h}$  near the respective Fermi levels can take part in scattering processes. For this reason, the mobility of drops at low temperatures is fairly high and they can easily be accelerated by external forces to velocities close to the velocity of sound in the crystal and can travel over macroscopic distances. High mobility represents one of the main properties of EHDs, which, to a large extent, allows observing most of the phenomena discussed in this section and Sections 2.8-2.10.

The dominant mechanism responsible for the deceleration of EHDs in sufficiently pure crystals is the scattering of electrons and holes comprising a drop by acoustic phonons, and, at low velocities  $v \ll s$ , where  $s$  is the speed of sound, the friction force, which is proportional to the velocity [3]. Therefore, when an external force  $\mathbf{F}$  acts on a drop, a constant-speed drift motion sets in after a short time  $t \sim \tau_p$  (where  $\tau_p$  is the drop momentum relaxation time). The drift velocity is

$$\mathbf{v} = \frac{\tau_p}{MN} \mathbf{F} = \frac{\tau_p}{M} \mathbf{f}, \quad (13)$$

where  $N$  is the total number of electron–hole pairs in the drop,  $M$  is the effective mass of an electron–hole pair, and  $\mathbf{f} = \mathbf{F}/N$  is the external force per pair of particles in the liquid. The coefficient before  $\mathbf{F}$  in Eqn (13) is the drop mobility. As a rule,  $F \propto N$  and the drift velocity  $v$  is independent of the drop size. Exactly this situation is implied when we speak about the ‘high mobility’ of EHDs, the term ‘mobility’ being used in this case for the ratio  $\tau_p/M$ . At the same time, the diffusion coefficient of EHDs is fairly small, because, according to the Einstein relation  $D_{\text{EHD}} = k_B T \tau_p / (MN)$ , it is inversely proportional to the total mass of the drop [17].

The EHD momentum relaxation time  $\tau_p$  was calculated by Keldysh [3] and Keldysh and Tikhodeev [182] for a semiconductor with an idealized band structure; later, a number of authors carried out calculations with the multi-valley structure of the conduction band, screening of the deformation potential by the EHD-bound charge carriers, and other factors taken into account.<sup>4</sup> The relaxation time increases significantly with decreasing the temperature. At low temperatures ( $T < 1$  K for Ge),  $\tau_p \propto T^{-5}$ , similarly to the mobility of electrons in metals limited by acoustic-phonon scattering.

In this section, we consider the motion of EHDs in the fields of nonuniform strain, either static [6, 106, 160] or dynamic (ultrasound waves [182, 184] and strain pulses [185]). Effects related to the drag of EHDs by the phonon wind [186] are considered in Sections 2.9 and 2.10. The acceleration of EHDs by other forces is also possible, but we do not dwell on these issues here.

In a nonuniform strain field, each electron–hole pair in the liquid is acted upon by a force

$$\mathbf{f} = -\nabla(E_g + E_0) = -\sum_{i,k} D_{ik} \nabla \varepsilon_{ik}, \quad (14)$$

where  $\varepsilon_{ik}$  are the components of the deformation tensor,  $D_{ik} = \partial(E_g + E_0)/\partial \varepsilon_{ik}$  is the net deformation potential of electrons and holes in the liquid, and  $E_g$  is the band gap. For  $P > P_{\text{cr}}$  (see Section 2.2), the energy  $E_0$  per pair of particles in the ground state of the liquid is independent of  $P$  (Fig. 2c), and  $\mathbf{f} = -\nabla E_g$ . The force given by Eqn (14) causes the motion of EHDs in strain fields.

In the field of a plane longitudinal ultrasound wave with  $\lambda_s \gg R$  propagating along the  $z$  axis, the force is  $\mathbf{f} = \mathbf{q} D \varepsilon_{zz} \sin(\omega t - qz)$ , where  $\varepsilon_{zz}$  is the strain amplitude in the wave,  $\omega$  is the angular frequency,  $q = 2\pi/\lambda_s$  is the magnitude of the wave vector  $\mathbf{q}$ , and  $\lambda_s$  is the wavelength. Under the action of  $\mathbf{f}$ , the drop is dragged in the direction of  $\mathbf{q}$  and at the same time performs an oscillatory motion as a whole in the course of the drift [182]. For low sound-wave intensities, when the drift velocity of drops is  $v \ll s_L$ , the ultrasound absorption coefficient attains a maximum as a function of  $\tau_p$  at  $\omega \tau_p = 1$ . For high sound-wave intensities, the drops can be entirely ‘captured’ by the wave and carried along at the speed of longitudinal sound ( $v = s_L$ ).<sup>5</sup>

The damping of ultrasound upon propagation through an EHD cloud in germanium was observed and investigated in [183] (the sound frequency and wavelength were 160 MHz

and  $\lambda_s \approx 30 \mu\text{m}$ ). The temperature dependence of the sound absorption coefficient exhibited a maximum at  $T = 2.4$  K. Under the experimental conditions of that study, the temperature dependence of the absorption coefficient was determined by the behavior of the EHD momentum relaxation time. The value of the momentum relaxation time at  $T = 2.4$  K was  $\tau_p = \omega^{-1} \approx 1$  ns. As the ultrasound intensity was increased, an additional maximum appeared in the temperature dependence of the absorption at  $T \approx 3.2$  K. This maximum is related to the excitation of capillary oscillations in EHDs [187, 188] (see also [189]). The drag of the EHDs by ultrasound was demonstrated in [184] by observing a change in the shape of the EHD cloud, which became elongated in the direction of the sound wave.

An experimental study of the EHD drag by pulses of longitudinal and transverse (shear) strain (coherent phonons) was carried out in [185]. Such pulses were generated in a Ge sample upon the irradiation of a thin metallic film deposited onto one of the faces of the sample by short high-intensity laser pulses. Propagating through the EHD cloud, strain pulses dragged the drops and transferred them with the speeds of longitudinal and transverse sound at distances as long as 4 mm (Fig. 8).

The motion of EHDs in nonuniform static strain fields has been studied most thoroughly [12, 14, 17, 112, 113]. Here, we briefly discuss the experiments in [106, 160], carried out using germanium samples of a special shape (resembling that of an hourglass) where the cross-sectional area varied along the compression axis according to a certain law. The distributions of elastic stress and of the strain gradient in the sample (and hence the force  $\mathbf{f}$ ) could easily be calculated. Therefore, the position of drops along the axis could be determined by monitoring the spectral position of the EHL luminescence line (Fig. 2c). These experiments demonstrated that EHDs created near the top or bottom of the sample move toward the middle section, where the strain is the highest. Upon excitation of strained samples with short laser pulses (duration  $t_p \approx 0.2 \mu\text{s}$ ), it was observed that the line corresponding to EHD luminescence in the top section of the sample, where the droplets were created, fades away from the spectrum with time, and the line corresponding to EHD luminescence in the middle section appears instead. Under these experimental conditions, the time of this spectral transformation, which is the time required for the drops to

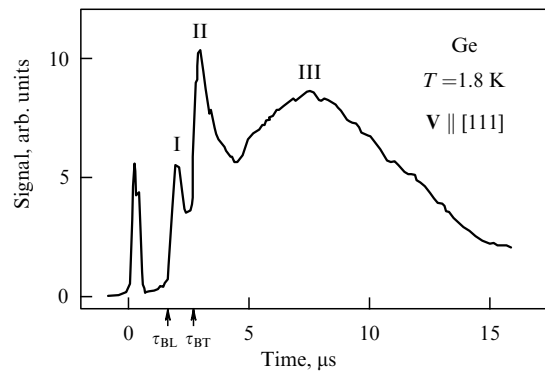


**Figure 8.** Signal arising at the p–n junction when EHDs moving with pulses of (I) longitudinal and (II) transverse deformation and (III) dragged by nonequilibrium phonons emitted by the ‘hot spot’ (see Section 2.9) arrive at the high-field region;  $\tau_{\text{BL}}$  and  $\tau_{\text{BT}}$  are times required for ballistic longitudinal and transverse phonons to traverse the sample [185].

<sup>4</sup> Relevant references and a discussion of the results obtained can be found in reviews [17, 112], where almost the entire range of issues related to the motion of EHDs is considered (see also reviews [12, 14, 113]).

<sup>5</sup> The deceleration and the properties of EHDs moving at near- and supersonic velocities represent an interesting topic in and of itself (see reviews cited in footnote 4).

travel from the top to the middle of the sample, was  $\approx 1 \mu\text{s}$ . This corresponds to the average velocity of EHD motion  $v \approx 3 \times 10^5 \text{ cm s}^{-1}$ .

In conclusion, we present some numerical data on the EHD momentum relaxation time. The values of  $\tau_p$  in Ge obtained by different methods exhibit considerable scatter (see reviews [12, 14, 17, 112, 113]). Adjusting the above-reported value of  $\tau_p$  corresponding to the maximum in the temperature dependence of ultrasound absorption to the temperature  $T = 2 \text{ K}$ , we obtain  $\tau_p \approx 2 \text{ ns}$ . The experiments by Tamor and Wolfe, considered in the next section, yield  $\tau_p = 0.53 \text{ ns}$  for Ge [190] and  $\tau_p \approx 0.6 \text{ ns}$  for Si [191] at  $T = 2 \text{ K}$ .

## 2.8 Giant electron–hole drops

Qualitatively new properties of the EHL were discovered under conditions where the electron–hole system is confined within some region of a nonuniformly strained sample where strain-induced shifts of the conduction and valence band edges result in the appearance of potential wells for electrons and holes (below, we refer to this region simply as the ‘potential well’). In the experiments considered below, a compressive force was applied to the surface of the sample using a nylon screw or a steel die with a spherical tip. In this case, one or several potential wells form in the crystal, depending on the crystallographic orientation of the compression axis. A wide range of issues related to the behavior of nonequilibrium electron–hole systems confined to a potential well in nonuniformly strained Ge and Si is discussed in review [113]. Additional information can be found in reviews [12, 94, 95, 192]. Here, we restrict ourselves to a discussion of experiments with large, or giant, EHL drops (called  $\gamma$  drops<sup>6</sup>).

Figure 9 shows a photograph of the surface of a nonuniformly strained Ge sample recorded by scanning a magnified image of this surface in the plane of the entrance slit of a spectrometer tuned to the EHL luminescence line [190]. A

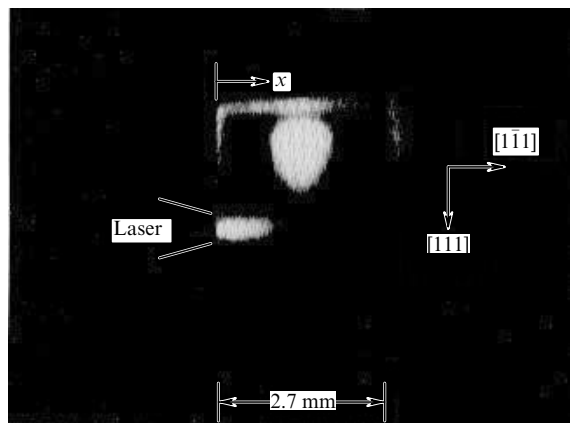


**Figure 9.** Images of luminescent regions in a nonuniformly strained Ge sample under CW excitation. The large luminous spot is a giant EHD and the elongated spot is a stream of small drops. The glow at the edges of the sample results from the scattering of recombination radiation from the EHDs on the surface. The sample size is  $3.5 \times 3.3 \times 2.7 \text{ mm}^3$  and  $T = 2 \text{ K}$  [190].

compression force was applied to the center of the upper face of the sample. The potential well is located in the bulk of the sample near the middle of the large egg-shaped luminous spot, which is the image of a giant EHD formed in the potential well. A ‘flare’ emanating from the excited region of the sample (in the vicinity of the laser focus) represents a cloud of conventional EHDs moving in the nonuniform strain field. Owing to the strain pattern, the EHDs are initially forced away from the sample surface in a nearly straight motion along the  $x$  axis and then, after traveling about 1 mm, move toward the potential well, where they merge into a giant drop.

Giant EHDs in nonuniformly strained Ge were discovered by a team at the University of California, Berkeley [193, 194], who observed the appearance of dimensional resonances in the absorption of 25 GHz microwave radiation at certain values of the magnetic field. These resonances are related to the formation of standing Alfvén waves in a giant EHD. Because the velocity of Alfvén waves is  $v_A \propto B$ , resonance conditions for different standing-wave modes can be attained by varying the magnetic field (see review [95]). These experiments made it possible to determine the radius of giant EHDs and to investigate their kinetics after the excitation is switched off. This kinetics could be described by the first expression in Eqn (11).

The radius of a giant EHD can also be determined from its photographic image (Fig. 9). However, such an image does not provide information on the internal structure of objects; in particular, a cloud of small-size drops cannot be distinguished from a monodrop (cf. their images in Fig. 9). The fact that the giant drop is a single whole is corroborated by the occurrence of Alfvén dimensional resonances and by the absence of light scattering, characteristic of a cloud of  $\alpha$  drops, in the bulk of the giant drop [195, 196].

The unusual paramagnetic properties of giant EHDs are a very interesting subject. A paramagnetic moment appears in a magnetic field due to the existence of recombination flows of electrons and holes within the liquid [197]. For this reason, the drop flattens in the direction of the field (see reviews [94, 95, 113] and the references therein).

Like conventional EHDs,  $\gamma$  drops have a metallic nature. The quantitative characteristics of giant EHDs, which were determined in experiments of different kinds [113, 198–200], depend on the orientation and magnitude of the compression. The radius of a  $\gamma$  drop increases with the excitation level, because the total number of electron–hole pairs in the potential well increases, and can be as large as  $\approx 0.5 \text{ mm}$ . Because the giant drop is located in the region of highest strain in the sample, its density is considerably lower (by a factor of 3–5 in most experiments) than the density of EHDs in unstrained Ge (see the table). Because of their low density, the lifetime of giant EHDs is more than an order of magnitude longer ( $\tau_0 \sim 500 \mu\text{s}$ ) than the lifetime of conventional EHDs (see Section 2.6).

Thus, similarly to a conventional liquid prevented from spilling out by the walls of a vessel, the EHL in nonuniformly strained germanium is accumulated in the potential well and forms a giant drop. A different scenario is realized in silicon. Small EHDs in a potential well do not merge into a single drop [113]; the formation of a giant EHD is prevented by the forces of mutual repulsion between the drops originating from phonon-wind effects (Section 2.9). The kinetics of the formation of a giant EHD in a potential well with the phonon-wind forces taken into account, as well as other

<sup>6</sup> In contrast to conventional EHDs, also called  $\alpha$  drops. Giant EHDs are sometimes also called monodrops.

related theoretical and experimental results, are considered in review [17].

## 2.9 Phonon wind

Nearly all of the energy spent on the formation of electron–hole pairs in a crystal ultimately dissipates into heat, i.e., is transferred to acoustic phonons (optical phonons decay into acoustic phonons very rapidly). Hence, in the presence of EHDs in a semiconductor, the appearance of intense streams of nonequilibrium acoustic phonons is inevitable. Nonequilibrium phonons are absorbed by excitons and EHDs and impart quasimomentum to them, which means that a phonon stream exerts a force on excitons and EHDs. As we see below, this force (the phonon-wind force) is of key importance for dynamic, microscopic, and spatial properties of the exciton–gas–EHD system [201, 186]). Effects related to the phonon wind are discussed in this and the next sections. Most comprehensively, this issue is considered in reviews [17, 112] (see also [12, 14]).

In an elastically isotropic semiconductor with an idealized band structure, the phonon-wind force acting on a pair of particles in the liquid at a point  $\mathbf{r}$  is

$$\mathbf{f}(\mathbf{r}) = \frac{m^2 D^2}{2\pi\hbar^3 \rho s_L^2 n_0} \overline{|\mathbf{q}|}_{q \leq 2k_F} \mathbf{J}(\mathbf{r}) \quad (15)$$

(summation over electrons and holes is omitted). Here,  $m$  is the charge-carrier effective mass,  $D$  is the deformation potential constant,  $\rho$  is the crystal density,  $s_L$  is the velocity of longitudinal sound,  $\mathbf{J}(\mathbf{r})$  is the phonon energy flux density, and  $|\mathbf{q}|_{q \leq 2k_F}$  is the magnitude of the wave vector of phonons averaged over their distribution function (the subscript indicates that due to energy and quasimomentum conservation, only relatively long-wavelength phonons with  $q \leq 2k_F$  can be absorbed in a degenerate EHL).

In a semiconductor with an idealized band structure, charge carriers can interact only with longitudinal phonons. In multivalley semiconductors, absorption of transverse phonons by the EHL is also possible. In this case, the electron–phonon interaction is anisotropic, which means that for each conduction-band valley,  $D$  and  $m$  in Eqn (15) depend on the angle between  $\mathbf{q}$  and the rotation axis of the constant-energy ellipsoid and, in addition,  $D$  depends on the phonon polarization. Moreover, deformation potentials within the EHL change due to the screening of electron–phonon interaction, which is also anisotropic. Furthermore, the magnitude of the electron Fermi wave vector  $k_F$  in the EHL depends on the direction of  $\mathbf{q}$ , which also contributes to the anisotropy of the force given by Eqn (15). Owing to the degeneracy of the valence band, holes can also interact with both longitudinal and transverse phonons. But the leading contribution to the absorption of phonons by the EHL comes from electrons (see [17, 112] and the references therein).

Under the action of a force  $f$ , EHDs acquire a drift velocity  $v$  determined by expression (13). This effect of EHD drag by the phonon wind, predicted by Keldysh [186], gives rise to most of the phenomena considered in this and the next sections. The layout of the experiment in which the drag effect was observed for the first time [186] is shown in the inset in Fig. 10. An EHD cloud formed under a bulk quasi-CW excitation of Ge by a laser emitting at the wavelength  $\lambda = 1.52 \mu\text{m}$  was analyzed by the absorption of a probe beam with  $\lambda = 3.39 \mu\text{m}$ . Nonequilibrium phonons were generated in the bottom part of the sample under CW

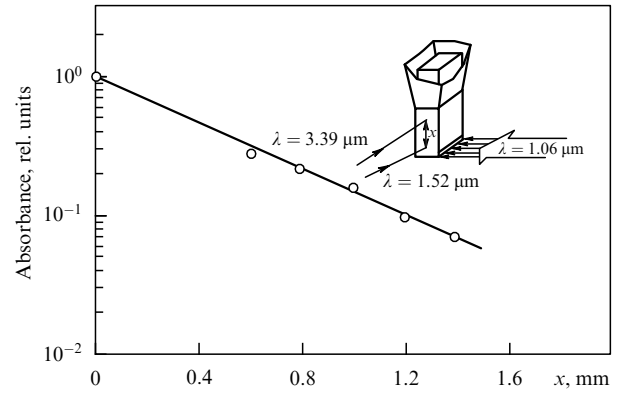


**Figure 10.** Absorption of probe radiation ( $\lambda = 3.39 \mu\text{m}$ ) by EHL droplets versus the distance between the center of the EHD generation region and the probe beam. Phonons are generated  $\approx 7 \text{ mm}$  below the probe beam by radiation with  $\lambda = 1.06 \mu\text{m}$  and a power  $\approx 40 \text{ mW}$ ; the temperature is  $T = 1.95 \text{ K}$ . The inset shows the experiment layout [186].

pumping by a laser with  $\lambda = 1.06 \mu\text{m}$ . When the EHD cloud was located between the probe beam and the phonon-generation region, EHDs moved under the action of the phonon wind toward the probe beam. In these experiments, EHDs were dragged by the phonon wind over distances of more than 2 mm. The spatial distribution of the absorption established under the action of the phonon wind is shown in Fig. 10. It can be described by the dependence  $\bar{n}(x) \propto \exp(-x/L_d)$ , typical of drift motion (here,  $\bar{n}$  is the average concentration of electron–hole pairs bound to the EHDs,  $L_d = v\tau_0$  is the drift length, and  $\tau_0$  is the electron–hole pair lifetime in the liquid). The slope of the straight line in Fig. 10 yields the drift length  $L_d \approx 0.5 \text{ mm}$ , which, for  $\tau_0 = 40 \mu\text{s}$ , corresponds to the velocity of the drop motion  $v \approx 1.3 \times 10^3 \text{ cm s}^{-1}$ . Measurements carried out for different values of the  $\lambda = 1.06 \mu\text{m}$  pump power indicate that in agreement with expressions (13) and (15), the drift velocity of EHDs increases linearly with the pump intensity. Subsequently, the drag of EHDs by the phonon wind [202–204] and the absorption of nonequilibrium phonons by the EHL [203, 205–208] were investigated in a range of experiments of different kinds.

An important role in understanding the entire range of phenomena under discussion is played by the mechanisms responsible for the generation of the phonon wind, i.e., relatively long-wavelength acoustic phonons with  $q \leq 2k_F$  under optical excitation of semiconductor crystals. Such phonons are emitted at the final stage of thermalization of photoexcited charge carriers, when their kinetic energy becomes lower than the Fermi energy of the EHL particles (the primary phonon wind).

The energy of charge carriers released upon their thermalization is mainly carried away by optical phonons, which rapidly decay into high-frequency acoustic phonons. At low temperatures ( $k_B T \ll \hbar\omega$ ) and small occupancies of phonon states ( $N_\omega \ll 1$ ), the main process of acoustic phonon relaxation is the spontaneous decay into two phonons with lower energies, which occurs at a rate  $\tau_N^{-1} \propto \omega^5$ . In sufficiently pure Ge and Si, the main resistive process leading to the loss of quasimomentum by the phonon subsystem is the Rayleigh scattering of phonons on isotopic impurities; the rate of this process is  $\tau_R^{-1} \propto \omega^4$ . A cloud of nonequilibrium phonons forms in the photoexcited region of the crystal, and

the rate of the diffusive expansion of this cloud, which is determined by the time  $\tau_R$ , increases with a decrease in the phonon frequency  $\omega$ . At large occupancies ( $N_\omega \sim 1$ ), processes of phonon merger become important, and a Planck distribution of nonequilibrium phonons with a temperature considerably exceeding that of the crystal can be established in the photoexcited region: a so-called hot spot forms [203, 209–211], which emits long-wavelength phonons in the course of cooling. The regimes of propagation of nonequilibrium phonons can be rather diverse; they are analyzed in detail in review [212] (see also [17, 112]). It is essential for us, however, that there exists a diffusively expanding cloud of high-frequency nonequilibrium phonons, which ultimately decay into long-wavelength ballistic phonons (phonon wind). Hereafter, we call this region a ‘hot spot’ (regardless of whether a certain temperature has been established in this spot), and the corresponding component of the phonon wind is referred to as phonons emitted by the hot spot.

Another contribution to the phonon wind arises from the EHDs themselves. The main channel of the electron–hole pair recombination in the liquid phase is the Auger process (see Section 2.6). In each recombination act, an Auger particle acquires an energy of the order of the band gap  $E_g$ . During the relaxation of Auger particles, some fraction  $\beta$  of this energy is transferred to the charge carriers bound into EHDs. As a result, the drop temperature is higher than the lattice temperature [12, 17, 112, 213–215]. In the limit case of small overheating ( $\Delta T \ll T$ ), the relative increase in the drop temperature is  $\Delta T/T = \beta E_g \tau_p / (3Ms^2\tau_0)$  [17, 112]. An EHD overheated compared with the crystal lattice acts as a thermal generator of nonequilibrium phonons.

The phonon energy flux emitted per unit volume of the liquid is  $\Delta\Phi = \beta E_g n_0 / \tau_0$ . The existence of this flux leads to several effects that have a significant effect on the EHD properties. In the isotropic case, the phonon energy flux density at a distance  $r$  from the center of a drop of radius  $R$  is

$$\mathbf{J}(\mathbf{r}) = \frac{1}{3} \beta E_g \frac{n_0}{\tau_0} \frac{R^3}{r^3} \mathbf{r}. \quad (16)$$

This stream of phonons drags the excitons,<sup>7</sup> and hence the exciton–gas density in the vicinity of the drop decreases, which leads to a reduction in the drop growth rate. Because  $J(R) \propto R$ , the growth of EHDs slows down abruptly with increasing  $R$ . This is one of the possible mechanisms responsible for the limitation of the EHD radius observed experimentally (see Section 2.4) [147, 186].

Another, probably more efficient, mechanism that can limit the EHD size is related to the instability of large volumes of the EHL caused by the phonon wind generated within the liquid itself [201]. Some of the nonequilibrium phonons emitted by the EHL are absorbed within the liquid. Between two elementary volumes  $\delta V$  and  $\delta V'$  in the liquid separated by a distance  $r$ , there is a repulsion force given by the expression

$$\mathbf{F} = \frac{\beta E_g}{8\pi^2} \frac{n_0}{\tau_0} \frac{m^2 D^2}{\hbar^3 \rho_s^2} \frac{\delta V \delta V'}{r^3} \mathbf{r} = \rho_{ph}^2 \frac{\delta V \delta V'}{r^3} \mathbf{r}, \quad (17)$$

<sup>7</sup> A drag of excitons by the phonon wind was observed in [186] in experiments similar to those in which the EHD drag was studied. However, this effect is much weaker.

which follows from Eqns (15) and (16). Here, we have introduced a notation  $\rho_{ph}$ , and we can see that bulk forces within the EHL originating from the phonon wind can be formally described as forces within a uniformly charged liquid with the charge density  $\rho_{ph}$ . A stability analysis for drops with  $R > R_s = [15\sigma / (4\pi\rho_{ph}^2)]^{1/3}$  demonstrates that surface tension supports the stability of spherical drops with the radii  $R < R_b = \sqrt[3]{2} R_s$ . An estimation for EHDs in Ge (where  $\rho_{ph} \approx 300 \text{ g}^{1/2} \text{ cm}^{-3/2} \text{ s}^{-1}$ ) yields the limit radius  $R_b \approx 20 \text{ }\mu\text{m}$ , in reasonable agreement with the experimental data [17, 112, 216].<sup>8</sup>

Certainly, repulsive forces (17) act not only between different parts of the same drop but also between all EHDs in the drop cloud [201]. In [216], the expansion of an EHD cloud due to the action of these mutual repulsion forces was observed over time spans of 10–100  $\mu\text{s}$  after bulk excitation of germanium with short light pulses, i.e., in the situation where the formation of an EHD layer and the relaxation of the hot spot were completed (see Section 2.10). The experiment was arranged such that the EHD layer had the shape of a ring whose radius increased with time at an average velocity  $\approx 4 \times 10^3 \text{ cm s}^{-1}$ . From these experimental data, the value of the constant of repulsive interaction in the EHL  $\rho_{ph}$  that is quoted above was obtained.

Forces of mutual repulsion acting between EHDs play an important role in the dynamics of the drop cloud and considerably affect its shape and size. This issue is treated in more detail in Section 2.10, while here we mention the experiment in [216], which confirmed the existence of this interaction. The authors observed an increase in the drift velocity of EHDs in a drop cloud in Ge (see Section 2.10, Fig. 11) when the drops were heated by infrared radiation. The generation of phonons upon EHD heating by infrared radiation was observed in [217].

There are no estimates for the repulsive interaction constant  $\rho_{ph}$  in the EHL in silicon based on experimental data. An estimation according to formula (17) yields  $\rho_{ph} \approx 2 \times 10^4 \text{ g}^{1/2} \text{ cm}^{-3/2} \text{ s}^{-1}$  for  $\beta = 0.1$  [17]. Using this value, we

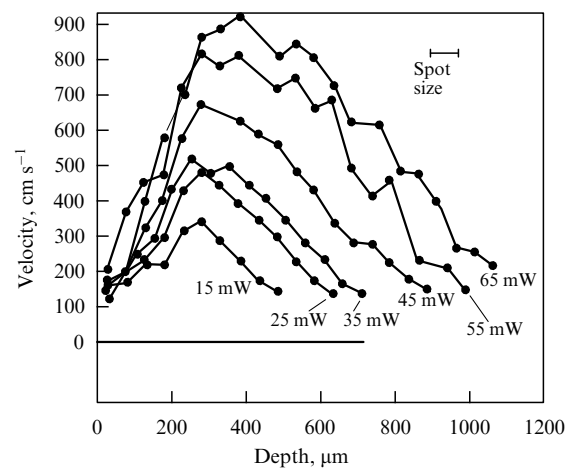


**Figure 11.** Drift velocity of EHDs in germanium versus the distance between the probe beam ( $\lambda = 3.39 \text{ }\mu\text{m}$ ) and the surface of the sample excited by an Ar laser ( $\lambda = 5145 \text{ }\text{\AA}$ ) for various excitation levels at  $T = 2 \text{ K}$  [222].

<sup>8</sup> Other mechanisms limiting the EHD size, unrelated to phonon wind effects, are possible as well (see reviews [17, 112] and the references therein).

obtain the maximum EHD radius  $R_b \approx 2 \mu\text{m}$ . In highly compressed Si, a reduction in the EHL density and an increase in the electron–hole pair lifetime in the liquid (see the table and Section 2.6) lead to a decrease in  $\rho_{\text{ph}}$  by about an order of magnitude. However, even in highly compressed Si,  $\rho_{\text{ph}}$  exceeds that in unstrained Ge by almost a factor of 10. Strong repulsive interaction between the EHDs prevents the formation of giant drops in a potential well in nonuniformly strained silicon (Section 2.8).

In conclusion, we mention that EHDs can be considered to be lumps of crystal-excitation energy, and their motion under the action of external forces to be directional excitation-energy transfer. The energy stored in EHDs can be transformed into other forms of energy. For example, in the experiments in [218] and [219], EHDs were transferred by the phonon wind to the surface of the sample, where the energy stored in the drops was released in a process of rapid nonradiative surface recombination and emitted into liquid helium surrounding the sample, being transformed into the energy of sound waves excited in a helium bath.

## 2.10 Spatial structure and dynamics of the electron–hole drop cloud

For a long time, the problem of the spatial distribution of EHDs was one of the most mysterious (a detailed discussion of this problem and the corresponding experiments can be found in reviews [12, 14, 17, 112, 163]). Numerous measurements of the ‘diffusion coefficient’ of EHDs yielded values differing by six orders of magnitude. It was established that EHDs move from the excitation region, where they form, at high speeds, and the size of the drop cloud increases with increasing the excitation level and decreasing the temperature. Models proposed for the dynamics of the EHD cloud did not explain the entire body of experimental data. The key to the solution to this problem was found by Keldysh [186, 201], who demonstrated that the drag of EHDs by the phonon wind (see Section 2.9) can be of decisive importance for the dynamics of the drop cloud and determine its shape and size. Experimental results, some of which are discussed below, have fully confirmed this conclusion.

The velocity of the drop motion and the shape of the EHD cloud depend on the excitation geometry. The spherical geometry is used most frequently: if the propagation of nonequilibrium phonons and the electron–phonon interaction are isotropic, focusing the excitation light into a tight spot leads to the formation of a hemispherical EHD cloud. The drops move from the excitation region along the radii of the hemisphere, and, under CW excitation, the velocity of the drop motion outside the excitation region at a distance  $r$  from the center of the hemisphere can be expressed as

$$v(r) = \frac{1}{2\pi\bar{n}_{\text{max}}\tau_0 r^2} \left( \Gamma G\tau_0 + 2\pi \int_0^r \bar{n}(r') r'^2 dr' \right), \quad (18)$$

where  $G$  is the total number of electron–hole pairs generated in the sample per unit time,  $\bar{n}(r)$  is the average density of the liquid phase at the point  $r$ ,  $\Gamma = \Delta E/(\beta E_g)$ ,  $\Delta E$  is the energy converted into the phonon wind in the excitation region per photoexcited electron–hole pair, and

$$\bar{n}_{\text{max}} = \frac{Mn_0^2}{4\pi\rho_{\text{ph}}^2\tau_p\tau_0}. \quad (19)$$

The term proportional to  $\Gamma$  in Eqn (18) accounts for the drag of the drops by the phonon wind produced in the excitation region (the primary phonon wind and phonons emitted at the hot spot; see Section 2.9). The integral term describes the expansion of the EHD cloud caused by the repulsive interaction between the drops. The quantities  $\Gamma$  and  $\bar{n}_{\text{max}}$  are the main parameters that govern the spatial distribution of EHDs.

Here, we omit detailed analysis and cumbersome formulas that describe the spatial distribution of EHDs (see reviews [17, 112] and the references therein) and restrict ourselves to a brief discussion of the main properties of the drop cloud. We can see from Eqn (18) that the velocity of the drop motion and hence the drift length of the drops, which determines the size of the cloud, increases with decreasing the temperature ( $v \propto \tau_p$ ; see Section 2.7) and with increasing the excitation level. At high excitation levels ( $\Gamma g\tau_0 \gg \bar{n}_{\text{max}}/\Gamma$ , where  $g$  is the generation rate per unit volume in the excitation region) and low temperatures (when the evaporation of the drops during their motion can be disregarded), the EHD drift length is

$$L_{\text{eff}} = \left[ \frac{3G\tau_0}{2\pi\bar{n}_{\text{max}}} (1 + \Gamma) \right]^{1/3}. \quad (20)$$

As long as the total number of electron–hole pairs bound into drops is proportional to  $G$  and the volume of the drop cloud is proportional to  $L_{\text{eff}}^3$ , the density of liquid-phase particles averaged over the volume of the cloud is independent of the generation rate at high excitation levels. In the excitation region,  $\bar{n} \approx \bar{n}_{\text{max}}/\Gamma$ ; this is the highest average density of particles in the condensed phase that can be attained under the conditions of steady-state non-bulk excitation [186].

An increase in the size of the EHD cloud in Ge proportional to the excitation intensity, as well as the saturation at a level of  $\bar{n} \approx 10^{15} \text{ cm}^{-3}$  of the average density of the liquid phase with increasing the excitation intensity were observed in a number of studies considered in detail in the cited review publications. The estimation of  $\bar{n}_{\text{max}}$  according to formula (19) using the value of  $\rho_{\text{ph}}$  given in the preceding section yields  $\bar{n}_{\text{max}} \approx 1.8 \times 10^{14} \text{ cm}^{-3}$  and  $\Gamma \approx \bar{n}_{\text{max}}/\bar{n} \approx 0.2$  [220, 221].

Direct confirmation of the dynamic nature of the EHD cloud was obtained in the experiments in [222], where the spatial distribution of the EHD drift velocities was measured at different excitation levels (Fig. 11). The velocities of EHDs were deduced from the measured Doppler frequency shift of the probe radiation scattered upon them.

We note that the description of exciton condensation kinetics considered in Section 2.5 cannot be immediately applied to a dynamic EHD cloud. In a steady-state dynamic cloud, the memory of the initial conditions, defined by the rate of switching on the excitation, is lacking. The main macroscopic parameters characterizing the exciton-drop cloud (the exciton gas density, the average concentration of electron–hole pairs bound into drops, the radius and concentration of the drops) and the spatial distribution of these parameters depend significantly on the EHD drift velocity, which is determined by the phonon wind intensity [223]. Transient processes can be fairly complicated, which can be seen in Fig. 12. Before a steady state is established after the excitation is switched on, the EHD radius, determined from the scattering of probe radiation at  $\lambda = 3.39 \mu\text{m}$ , decreases initially and then begins to increase to a steady-state value.



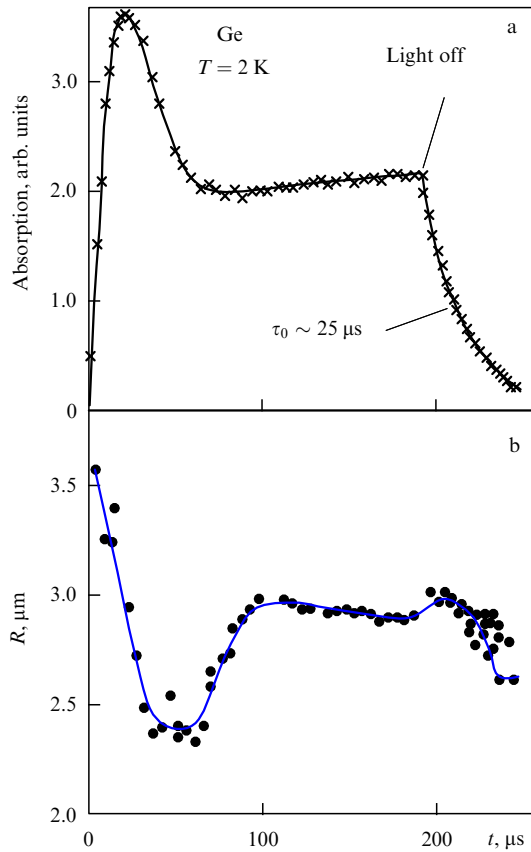


**Figure 12.** Time dependences of (a) absorption by EHDs and (b) EHD radius after switching on the excitation by an Ar laser at the time  $t = 0$ ; the excitation pulse duration is  $t_p = 200 \mu\text{s}$  (K L Shaklee, H W Epworth, and J M Worlock; see [224]).

The absorption of probe radiation passes through a maximum at the initial stage [224]. It was demonstrated in [225] that the transient absorption peak is observed only at high excitation levels, when the phonon wind effect is important.

The most beautiful manifestation of the effect of EHD drag by phonon wind and, at the same time, convincing evidence indicating that this effect is responsible for the formation of the spatial distribution of EHDs is the occurrence of the anisotropic spatial structure of the drop cloud in germanium, observed and investigated in detail in a series of experiments [226–230]. The anisotropic spatial structure of the EHD cloud appears upon the tight point-like focusing of the excitation laser beam onto the surface of the sample. Its existence originates from the anisotropy of phonon fluxes and the anisotropy of the electron spectrum of the crystal and the electron–phonon interaction, as mentioned in Section 2.9. Because of the anisotropy in the elastic properties, acoustic phonons in crystals propagate predominantly along certain crystallographic directions (the focusing, or channeling, of phonons<sup>9</sup>). In germanium, longitudinal acoustic phonons are focused along the  $\langle 111 \rangle$  directions, while transverse phonons in the  $T_1$  mode (fast transverse

mode for the  $\langle 110 \rangle$  directions) propagate close to the  $\{100\}$  planes, and those in the  $T_2$  mode (slow transverse mode) close to the  $\langle 100 \rangle$  and  $\langle 111 \rangle$  axes. Correspondingly, the main features in the spatial structure of the EHD cloud are wide lobes near the  $\langle 111 \rangle$  crystallographic directions and narrow flares stretched along the  $\langle 100 \rangle$  axes of the crystal. Photographs of an EHD cloud are shown in Fig. 13.

Experimental data for silicon are scarce. Because the EHL lifetime in Si is considerably shorter than that in Ge (see Section 2.6), the size of the drop cloud in Si is small. The average concentration of electron–hole pairs bound into drops saturates with the pump intensity at a level of  $\bar{n} \approx 1.5 \times 10^{16} \text{ cm}^{-3}$  [232]. An estimation by formula (19) using the value of  $\rho_{\text{ph}}$  given in Section 2.9 yields  $\bar{n}_{\text{max}} \approx 1.9 \times 10^{16} \text{ cm}^{-3}$ . These values of the average concentration correspond to  $\Gamma \approx 1.3$ . The anisotropic structure of the EHD cloud in Si is fairly weakly pronounced, apparently mainly because the size of the cloud is of the same order as the size of the excitation region.

So far, we have considered the properties of a steady-state drop cloud. Spatiotemporal measurements under pulsed laser excitation allow investigating the dynamics of the EHD cloud and, furthermore, revealing effects originating from different components of the phonon wind (see Section 2.9), because these components are separated in time (see reviews [17, 112] and the references therein).

The dynamics of the EHD cloud in germanium under pulsed excitation was studied for the first time in [233], where spatially and temporally resolved measurements of the scattering of probe radiation by drops were carried out. Under sufficiently intense excitation, a layer of EHDs was observed to form, moving from the excited surface into the bulk of the crystal. In a series of similar experiments carried out later by a team at the Lebedev Institute, it was established that the dynamics of the drop cloud passes consecutively through three stages differing by the mechanisms of the generation of the phonon wind (see Section 2.9) propelling the drops:

(i) A cloud of nonequilibrium charge carriers expands at a constant near-sonic velocity under the action of the primary phonon wind, with the formation of an EHD layer commencing at the leading edge of the cloud. The expansion velocity is nearly independent of the excitation level and temperature. The duration of this stage is  $t \leq 0.5 \mu\text{s}$  [234].

(ii) Under the action of the phonon wind emitted by the hot spot, the EHD layer moves into the bulk of the sample for  $\approx 8 \mu\text{s}$  with a velocity that decreases steadily from its initial value  $\sim 10^5 \text{ cm s}^{-1}$  (parallel linear segments on the curves in Fig. 14) [235].

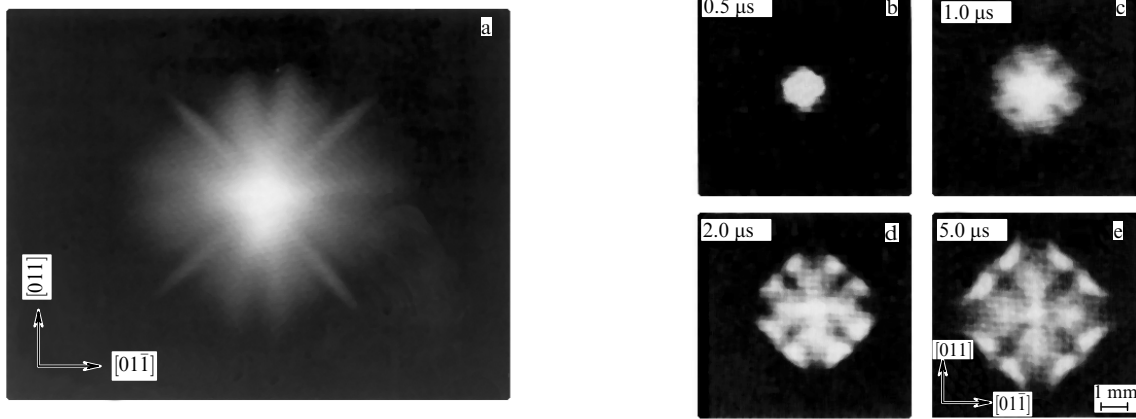
(iii) Expansion of the EHD cloud at an average velocity  $\sim 10^3 \text{ cm s}^{-1}$  under the action of the mutual repulsion forces between the EHDs [236]. The duration of this final stage of the cloud dynamics exceeds  $100 \mu\text{s}$ .

Figure 14 shows the variation in the velocity of the leading edge of the EHD layer during the first and second stages of the drop cloud dynamics.

Similarly to the steady-state case, the drop cloud has an anisotropic spatial structure under pulsed excitation (Figs 13b–13e) [237, 238].

Finally, we note that the model suggested in [234] to describe the first stage of the EHD cloud dynamics proves to be also applicable to explaining exciton transport in bulk semiconductors [239, 240] and quantum wells [241] at high levels of optical excitation.

<sup>9</sup> Phonon focusing is considered in detail in review [231]. See also [17, 112] and the references therein, which also include information on the studies of phonon propagation in germanium.



**Figure 13.** EHD cloud in germanium photographed through the face of the sample parallel to the (100) plane; the excitation radiation is focused onto the opposite surface. (a) Stationary EHD cloud; the photograph size corresponds to a size of 2.5 mm on the sample,  $P = 76$  mW, and  $T = 1.75$  K [228]. (b–e) Dynamics of the EHD cloud: photographs are taken at different times after a 300 ns excitation pulse with an energy of 200 erg;  $T = 1.8$  K. Images in panels (b–d) are magnified by a factor of 1.3 in comparison to panel (e) [238].

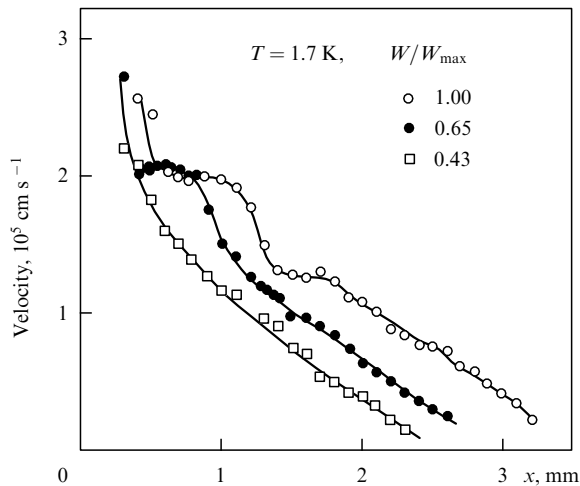


**Figure 14.** Velocity of the leading edge of an EHD cloud in germanium versus the distance from the excited surface of the sample for different excitation pulse energies ( $W_{\max} = 120$  erg). A molecular-nitrogen laser served as the excitation source ( $\lambda = 0.34$   $\mu\text{m}$ , pulse duration  $t_p \approx 10$  ns), and planar excitation geometry (one-dimensional inward motion of EHDs from the excited surface of the sample) was used. The  $x$  axis is oriented along the  $\langle 110 \rangle$  direction [234].

### 3. Electron–hole liquid in low-dimensional semiconductor structures

#### 3.1. Stability of the electron–hole liquid in low-dimensional structures

The possibility of the formation of a liquid in low-dimensional structures is determined, similarly to bulk materials, by the stability of the liquid state (see Section 2.2): the absolute value of the energy per pair of particles in the ground state of the liquid has to exceed the exciton binding energy (or, strictly speaking, the energy per exciton in an exciton molecule). Both the ground-state energy of the liquid and the exciton binding energy in low-dimensional structures depend on the parameters of the specific structure (e.g., the well width and depth in QW structures) and of the constituent materials.

According to the calculations in [242–244], in GaAs/AlGaAs QWs, which are type-I heterostructures (the potential wells for electrons and holes occur in the same layers of the structure, in this case, in GaAs layers), the EHL is unstable for typical parameters of the structure because the exciton ground state has the lowest energy. In this regard, we recall that the EHL in bulk GaAs is stable only because of the polaron effect (see Section 2.2).<sup>10</sup> At the same time, the EHL is stable in narrow (several-monolayer-wide) GaAs/AlAs QWs of type II (electrons and holes occupy the neighboring layers of the structure, in this case, AlAs and GaAs layers) [244–246]. For six- and four-monolayer-wide layers respectively in GaAs and AlAs, the work function of excitons in the EHL is as high as 2.5 meV [244].

We note that upon the transition from GaAs/AlGaAs to GaAs/AlAs structures, both excitons and the EHL become spatially indirect (dipolar) and, furthermore, momentum-space indirect and anisotropic. A higher degeneracy (an increase in the number of equivalent minima in the conduction band) and the anisotropy of the electron spectrum have a relatively weak effect on the binding energy of excitons and biexcitons,<sup>11</sup> but lead to a considerable increase in the ground-state binding energy of the liquid (see Section 2.2). It can therefore be guessed *a priori* that the EHL is stable in low-dimensional systems based on multivalley semiconductors.

#### 3.2 Condensation of dipolar excitons in GaAs/AlGaAs structures with double quantum wells

Apparently, the condensation of dipolar excitons into the EHL in type-II heterostructures was observed for the first time in a study of the photoluminescence (PL) spectra of short-period GaAs/AlAs superlattices grown on (311)A-oriented GaAs substrates [249]. A structure of this kind represents a superlattice of quantum wires that form along the growth steps and

<sup>10</sup> It should be mentioned that the experimental observation of an EHL with a low binding energy (exciton work function in the liquid) in direct-gap semiconductors and in QWs based on these materials can be hampered by the self-heating of the exciton system in the processes of radiative recombination of excitons and biexcitons [247].

<sup>11</sup> The binding energies of excitonic molecules in bilayer systems were calculated in [248].

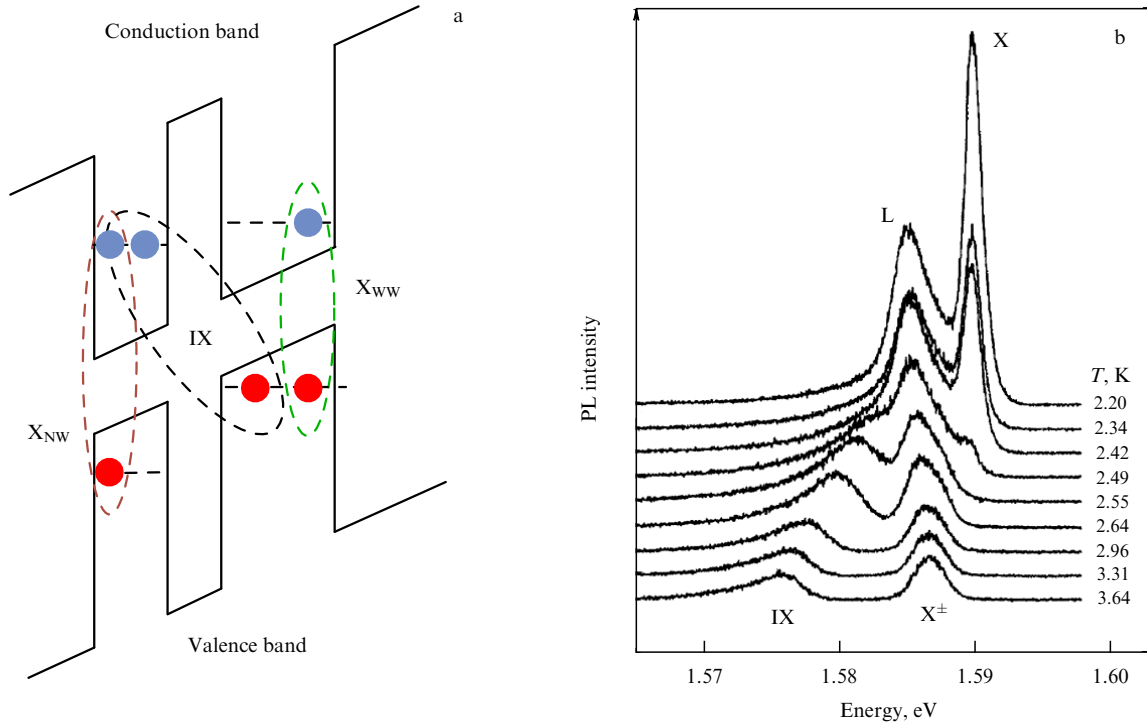


**Figure 15.** (Color online.) (a) Energy band diagram of an asymmetric double-well structure in an electric field applied along the growth axis. IX,  $X_{NW}$ , and  $X_{WW}$  designate spatially indirect (interwell) exciton and intrawell excitons in narrow and wide QWs; blue and red circles respectively represent electrons and holes [253]. A symmetric structure (with two QWs of the same width) was used in [252]. (b) PL spectra of a symmetric double-well structure at different temperatures, indicated on the right next to each curve. The excitation intensity is  $P = 10 \text{ mW cm}^{-2}$ . A forward bias of  $+0.7 \text{ V}$  is applied to the p-i-n structure [252].

are tunneling-coupled in the plane of the superlattice layers. The density, the binding energy (exciton work function), and the critical temperature of the observed EHL were found to be  $n_0 \approx 1.3 \times 10^{12} \text{ cm}^{-2}$ ,  $\phi \approx 4.5 \text{ meV}$ , and  $T_c \approx 16 \text{ K}$ . At temperatures exceeding the critical temperature, the EHP luminescence was observed.

Superlattices that had similar parameters but were grown on (001)-oriented GaAs substrates and hence represented heterostructures with planar QWs were investigated in [250, 251]. The dynamics of the PL spectra was measured under excitation with a mode-locked Ti:sapphire laser emitting a train of 140 fs pulses at a repetition rate of 76 MHz (380 kHz after pulse picker). At the temperature  $T = 10 \text{ K}$ , the PL spectrum featured a broad EHP luminescence line for about 0.4 ns after the excitation pulse, and exciton and biexciton lines appeared after about 0.7 ns. After about 14 ns, the EHP luminescence band ceased to depend on time, which is a signature of EHL emission, because the liquid density remains unchanged in the course of recombination of constituent particles. The binding energy of this spatially indirect (dipolar) EHL with respect to the energy of the exciton molecule was  $\sim 3.1 \text{ meV}$ .

An EHL with spatially separated electrons and holes in double GaAs/AlGaAs QWs was observed and investigated in [252]. These experiments were carried out on a p-i-n GaAs/Al<sub>x</sub>Ga<sub>1-x</sub>As structure ( $x = 0.35$ ) into which two GaAs QWs 8 nm wide, separated by an Al<sub>x</sub>Ga<sub>1-x</sub>As barrier layer 5 nm wide, were embedded. The energy-band diagram of the active region of the structure under an applied electric bias is shown schematically in Fig. 15a. Figure 15b shows the PL spectra of the structure recorded at different temperatures under CW resonant excitation into the ground state of the

spatially direct (intrawell) light-hole exciton. As the temperature decreases, the emission line of the spatially indirect (interwell, or dipolar) exciton (labeled IX) shifts to higher energies. In a narrow temperature range (2.55–2.42 K), the PL spectrum experiences a dramatic transformation: the IX line almost vanishes; in place of the line  $X^\pm$  of charged excitonic complexes (trions), a new line L gradually appears, which differs from the trion line in its spectral position, shape, and width; the line of intrawell excitons X appears. Line L appears in the spectrum in a threshold manner both upon a reduction in temperature at constant excitation intensity and upon an increase in the excitation intensity at constant temperature (lower than the critical temperature, which, for the forward bias voltage  $+0.7 \text{ V}$  applied to the p-i-n structure, was  $\sim 8.5 \text{ K}$ ).

Data on the PL and PL excitation spectra in magnetic fields up to 5 T and the results of spectrally resolved kinetic measurements upon the excitation of the structure with picosecond laser pulses led the authors of [252] to the conclusion that the L line corresponds to an EHL with electrons and holes occupying the neighboring QWs of a double-well structure. The liquid density estimated using the results of magneto-optical measurements is  $n_0 \approx 8.8 \times 10^{10} \text{ cm}^{-2}$ , independent of the forward-bias voltage applied to the structure. Under a reverse bias of  $-2.5 \text{ V}$ , the estimated EHL density is  $n_0 \approx 1.5 \times 10^{11} \text{ cm}^{-2}$ . The binding energy of the liquid with respect to the intrawell-exciton energy, estimated from the lineshape analysis of the L line, is  $\phi \approx 4.5 \text{ meV}$ .

The experiments in [253] were carried out on asymmetric double-well GaAs/AlGaAs structures ( $x = 0.28$ ) containing 12 nm and 18 nm QWs separated by a 3 nm barrier (Fig. 15a).

The samples were shaped like mesas  $100 \times 100 \mu\text{m}$  in size. The PL spectra were recorded under CW intrawell excitation (laser photon energy 1.59 eV). With increasing the excitation level, the PL spectrum at  $T = 1.5 \text{ K}$  exhibited almost the same qualitative changes as those occurring with decreasing the temperature in the experiments in [252] (Fig. 15b), described in the preceding paragraphs (in the experiments under discussion, the line designated as X in Fig. 15b corresponds to the intrawell exciton  $X_{\text{WW}}$  in the wide QW). The luminescence line of a metallic dipolar EHL (line L in Fig. 15b) was not observed in this case (or, at least, the authors do not discuss the behavior of the PL spectra at high pumping levels in these terms).

The most pronounced changes in the PL spectra occurred at considerably (about an order of magnitude) higher excitation levels. A new line (line Z), shifted by 3–4 meV to lower energies from the line of dipolar excitons, appeared in the spectrum in a threshold manner upon either decreasing the temperature or increasing the excitation level. For the excitation power  $W = 250 \mu\text{W}$ , the threshold temperature was 4.7 K; for the temperature  $T = 0.7 \text{ K}$ , the threshold power was  $210 \mu\text{W}$ . In this situation, the luminescent images of the mesa surface broke into domains (regions I and II in Fig. 16a) with a clear dark boundary between them. These domains correspond to distinct emission lines in the PL spectra: the lines of interwell excitons IX and the Z line are dominant in respective regions I and II (Fig. 16b). With an increase in the excitation power, the area of region II increased until it expanded over the entire surface of the mesa.

The authors of [253] believe that the Z line corresponds to a ‘classical’ excitonic liquid predicted in [26]. According to their estimates, the liquid density is  $(4-6) \times 10^{10} \text{ cm}^{-2}$ . The main arguments in favor of this interpretation are the considerably lower lateral electrical conductivity in domain II compared to domain I and the shape and behavior of line Z with increasing the excitation level. This line has a Gaussian shape and shifts to higher energies and narrows with an increase in the excitation level. The narrowing and high-energy shift give evidence of an increase in the density of the new phase, although, apparently, the density of a liquid, which is determined by internal repulsion and attraction forces, should remain constant until the liquid fills the entire sample.

### 3.3 Quantum electron–hole droplets (dropletons)

According to the discussion in Section 3.1, the EHL in type-I GaAs/AlGaAs QWs is unstable. At the same time, as was demonstrated in [254] and [255], a strongly nonequilibrium EHP in these QWs can host liquid droplets (which the authors called dropletons) consisting of just a few electron–hole pairs and having a quantized binding energy. Experiments were performed on GaAs/AlGaAs structures ( $x = 0.3$ ) with several tunneling-isolated QWs 10 nm wide (separated by barriers of the same width). After the removal of the substrate, the samples were placed on a sapphire disk. The transmission spectra of the structure were recorded at different times after an excitation pulse (the pump–probe technique). A Ti:sapphire laser tuned to the frequency of the transition to the ground (1s) state of the heavy-hole exciton in the QW was used as a source of both pump and probe pulses, whose respective durations were 320 and 160 fs. The pump and probe beams were circularly polarized opposite to each other.

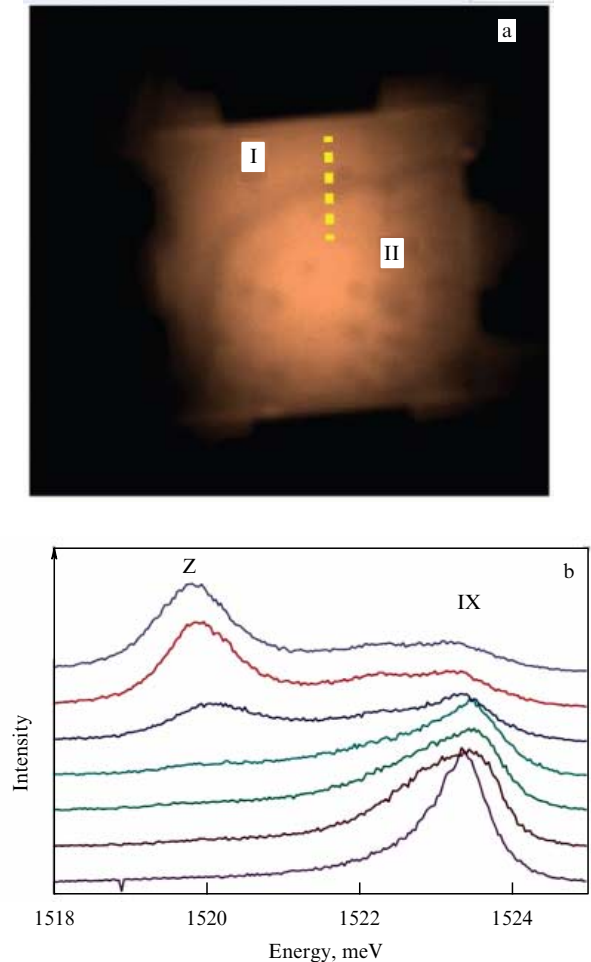


**Figure 16.** (Color online.) (a) Luminescent image of a mesa surface. The boundary between domains I and II is clearly visible. (b) MicroPL spectra recorded at different points of the structure along the thick dotted line shown in panel (a). Each spectrum is shifted vertically by an amount corresponding to the position of the measurement point.  $T = 1.5 \text{ K}$ ,  $W = 250 \mu\text{W}$ , the bias voltage applied to the structure is  $V_g = 2.3 \text{ V}$  [253].

To increase the sensitivity of the registration of multi-particle correlated states, the authors used a special projection protocol [256] that allowed transforming an array of data obtained in the measurements of conventional differential absorption  $\Delta\alpha$  (defined in terms of classical changes in the pump intensity) for a large set of pump intensities into an array of data from quantum-optical ‘measurements’ of differential absorption  $\Delta\alpha_{\text{MB}}$  (defined in terms of the quantum-optical fluctuations in the pump source). The results obtained with such a transformation are shown in Fig. 17 in coordinates of the binding energy  $E_{\text{bind}}$  (with respect to the exciton energy level) versus the number of photons in the pump pulse  $N_{\text{pump}}$ . At low pump levels, the spectra of  $\Delta\alpha_{\text{MB}}$  feature a biexciton resonance. With increasing the pump level, as  $N_{\text{pump}}$  approaches the values  $1.3 \times 10^6$ ,  $3.5 \times 10^6$ , and  $5 \times 10^6$ , the resonances experience abrupt shifts corresponding to transitions between neighboring energy bands of dropletons. In other words, the formation of dropletons containing 4, 5, and 6 electron–hole pairs becomes possible at these pump levels. The positions of the maxima in the  $\Delta\alpha_{\text{MB}}$  spectra are in good agreement with the results of calculations of the dropleton energy spectra carried



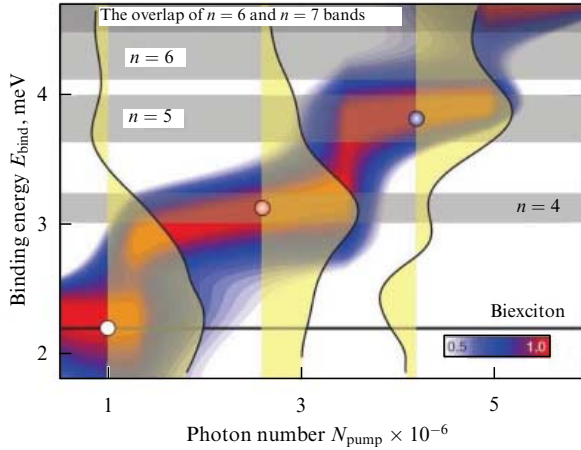


**Figure 17.** (Color online.) Detection of dropletions by quantum spectroscopy. Color-scale map of quantum-optical differential absorption  $\Delta\alpha_{\text{MB}}$  at the time  $t = 16$  ps after a pump pulse ( $T = 10$  K). Black lines framing yellow-shaded regions represent the spectra of  $\Delta\alpha_{\text{MB}}$  for  $N_{\text{pump}} = 1 \times 10^6$ ,  $2.6 \times 10^6$ , and  $4.2 \times 10^6$  (left, middle, and right curves, respectively). Gray horizontal bands show the calculated energy bands of respective dropletions containing  $n = 4, 5, 6$ , and  $7$  electron–hole pairs. Black horizontal line shows the biexciton binding energy [254].

out by the authors. Spectrally resolved kinetic measurements of  $\Delta\alpha_{\text{MB}}(E_{\text{bind}}, t)$ , where  $t$  is the time delay between the pump and probe pulses, demonstrated the occurrence of quantum beats between energy levels corresponding to dropletions with 4 and 5 pairs of particles; the beat frequency corresponded to the energy separation between these levels. These experiments also allowed obtaining a rough estimate of the dropletion lifetime (25 ps).

### 3.4 Electron–hole liquid in type-I silicon quantum wells

Experimental studies of the EHL formed in thin Si layers [257, 258] and Si QWs [259, 260] in type-I Si/SiO<sub>2</sub> heterostructures were carried out on structures grown by silicon-on-insulator technology. Such structures are made on an Si substrate and consist of a thin layer of single-crystal silicon embedded between two oxide layers, which represent barriers for electrons and holes in silicon. Thus, Si/SiO<sub>2</sub> structures are characterized by a type-I energy band diagram with deep potential wells for charge carriers in the Si layer; the respective band offsets at the interfaces are 3.2 and 5 eV for electrons and holes. The PL spectra of such structures with the Si layer thicknesses ranging from 54 to 320 nm were investigated in [257, 258]. At low temperatures, the formation of the EHL was observed; at temperatures exceeding the critical one, an exciton–gas–EHP transition occurred. The properties of the observed EHL were almost the same as in bulk silicon (see Section 2.1). At the same time, as was mentioned by the authors of both papers, the confinement of nonequilibrium charge carriers in Si layers leads to a considerable reduction in the threshold excitation intensity for the formation of the EHL at a given temperature as compared to bulk silicon (see also [261]).

The PL spectra of Si/SiO<sub>2</sub> structures with the silicon layer thicknesses  $d$  from 4.7 to 190 nm were investigated in [259, 260]. In the structures with  $d > 3a_{\text{ex}} \approx 15$  nm (where  $a_{\text{ex}} = 4.9$  nm is the exciton Bohr radius in bulk Si), the authors observed a three-dimensional EHL. In thicker Si layers with thicknesses in this range, the spectral position and shape of the EHL luminescence line were independent of the

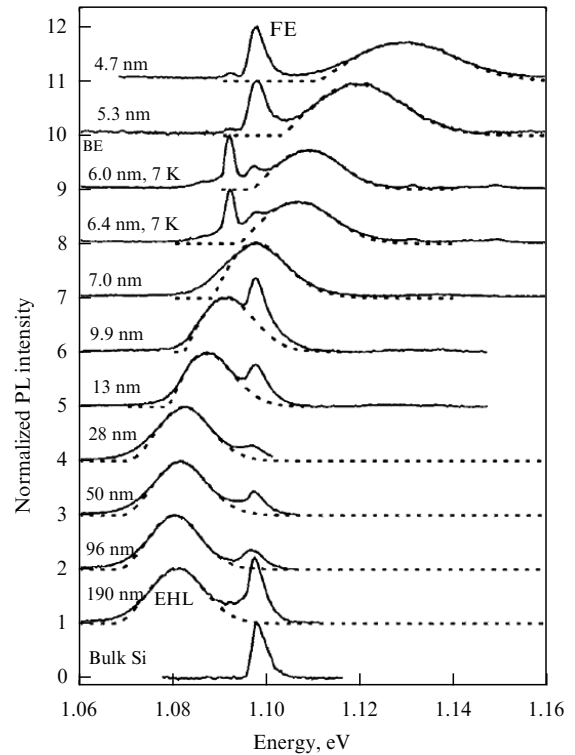


**Figure 18.** TO components of the EHL luminescence spectra (solid lines) in silicon layers of different thicknesses (indicated on the left next to each curve) recorded at  $T = 15$  K ( $T = 7$  K for two spectra) under excitation by an Ar<sup>+</sup> laser ( $\lambda = 351$  nm) with the power density  $P = 6.5$  W cm<sup>-2</sup>. The free- and bound-exciton lines of the substrate (FE and BE, respectively) are also present. Dashed lines show the theoretical fits of the EHL lines according to Eqn (6) with a three-dimensional and a two-dimensional density of states for  $d \geq 28$  nm and  $d \leq 13$  nm, respectively [260].

excitation level (Fig. 18) and the liquid density and the exciton work function in the EHL were almost the same as in bulk silicon (see the table). In thinner Si layers ( $\sim 30$  nm or less), the EHL line experienced a red shift with increasing the excitation level before stabilizing at its ultimate position. The authors explained this shift by a decrease in the contribution from the surface energy of the EHL drops to the chemical potential of the liquid as the lateral size of the drop increases. This explanation is based on the assumption that the smallest diameter of the drops that form in the structure is determined by the Si layer thickness.

In structures with  $d < 15$  nm, the quantum confinement of charge carriers starts to affect the electron energy spectrum in the silicon layer and hence the spectral position of the EHL luminescence line, which shifts to higher energies with a decrease in the Si layer thickness (see Fig. 18). In these structures, the EHL is quasi-two-dimensional and the liquid drops have a pancake-like shape. The density of this quasi-two-dimensional EHL was determined from theoretical fits to the shape of the EHL luminescence line; for a structure with  $d = 4.7$  nm, the density was  $n_0 \approx 2.4 \times 10^{12}$  cm<sup>-2</sup>. Based on Kleinman's approach [242], the authors built a theoretical model of a quasi-two-dimensional EHL and calculated phase diagrams for the electron–hole system in quantum-confined silicon layers of various thicknesses [260]. The calculations took the dielectric mismatch (the difference in the dielectric constants) between the QW and barrier layers into account [262, 263] (see also [264] and the references therein), which is

significant for structures of this kind. According to these calculations, the EHL density and critical temperature increase considerably with a decrease in the thickness of the Si layer.

### 3.5 Spatially direct and dipolar electron–hole liquids in type-II Si–Ge heterostructures

**3.5.1. Three-dimensional EHL in heterostructures with wide SiGe layers.** For a relatively low Ge content, Si/Si<sub>1-x</sub>Ge<sub>x</sub> structures are of type II: the SiGe layer represents a fairly deep potential well for holes and a low potential barrier for electrons. For  $x = 0.05$ , the conduction- and valence-band offsets are  $\Delta E_c = 5$  meV and  $\Delta E_v = 40$  meV; for  $x = 0.07$ ,  $\Delta E_c = 7$  meV and  $\Delta E_v = 60$  meV [265, 266]. As we see below, both spatially direct EHL (with electrons and holes in the SiGe layer) and dipolar EHL (with spatially separated electrons and holes) can be observed in these structures.

For small values of  $x$ , the band structure of Si<sub>1-x</sub>Ge<sub>x</sub> alloys is the same as that of Si. However, owing to the presence of internal strain in the pseudomorphic Si<sub>1-x</sub>Ge<sub>x</sub> layer grown on a strain-free Si(001) substrate, the sixfold (disregarding spin) degeneracy of the conduction-band minimum is lifted: two of the minima occur higher in energy than the other four [265, 266]. The degeneracy of the top of the valence band is also lifted.

In the remaining part of this review, we consider a series of studies of the nonequilibrium electron–hole system in Si/Si<sub>1-x</sub>Ge<sub>x</sub>/Si heterostructures (for a more detailed discussion of this work, see [267]). The structures were grown by molecular-beam epitaxy on silicon substrates. The germanium content  $x$  in the strained SiGe layers ranged from 0.029 to 0.25, and their thicknesses  $d$  were between 2 and 70 nm. The respective thicknesses of the buffer and cap Si layers were 100 and 100–200 nm.

The behavior of the low-temperature PL spectra of the structures with  $x = 0.05$  and wide SiGe layers upon varying the temperature and the excitation level was qualitatively nearly the same as that of the spectra of bulk material with the same Ge content [268, 269]. The lineshape analysis of the luminescence from the EHL in the SiGe layer according to Eqn (6), assuming three-dimensional densities of states for electrons and holes, yields the values  $n_0 = 2.3 \times 10^{18} \text{ cm}^{-3}$  and  $\phi = 2.4$  meV for the EHL density and the EHL binding energy relative to the bottom of the exciton band. In bulk material of the same composition,  $n_0 = 3.5 \times 10^{18} \text{ cm}^{-3}$  and  $\phi = 8.3$  meV. A reduction in the density and binding energy of the EHL in the alloy layer of the structure compared to bulk material is caused by the existence of internal strain in this layer. The critical temperature of the EHL in the SiGe layer estimated on the basis of experimental data is  $T_c \approx 20$  K. At higher temperatures, the luminescence of EHP was observed.

Thus, a three-dimensional EHL forms in wide SiGe layers. Both electrons and holes reside in the alloy layer because the potential barrier in the conduction band is low (and is reduced further owing to band bending caused by the electric field of holes localized in the SiGe layer) and electrons can enter the SiGe layer.

Similarly to Si/SiO<sub>2</sub> structures (see Section 3.4), a reduction in the intensity threshold for EHL formation is observed in Si/SiGe structures. In the spectral region corresponding to the buffer and cap silicon layers of the structure, as well as in bulk alloy samples of the same composition, the EHL luminescence lines appeared at a fixed temperature at considerably higher pump intensities

than in the SiGe layer. For example, at  $T = 6$  K, the threshold excitation intensity for the formation of the EHL in the SiGe layer is about one fifth that in the bulk material. This is explained by the accumulation of photoexcited charge carriers in the SiGe layer, which is a potential well for holes.

**3.5.2 Spatially direct EHL; conditions of existence.** The conditions required for the existence of a spatially direct quasi-two-dimensional EHL in Si/SiGe structures with thin SiGe layers have been investigated in a number of studies. Figures 19a and 19b show the TO components of the PL spectra of an Si<sub>1-x</sub>Ge<sub>x</sub> layer with the thickness  $d = 2$  nm and the Ge content  $x = 0.09$  at different pump levels and temperatures, obtained in [270] and [271] under short-wavelength excitation (He–Cd laser,  $\lambda = 0.44 \mu\text{m}$ ). At low excitation levels and high temperatures, the spectra feature a relatively narrow line (its FWHM at  $T = 15$  K is approximately 4 meV) that corresponds to the luminescence of free excitons (FEs). For  $T < 12$  K and low pump densities, the free-exciton line experiences a red shift with decreasing temperature owing to the localization of excitons by the inhomogeneities of the layer composition. This is accompanied by a decrease in the intensity of this line and the appearance of the localized-exciton (LE) line. At  $T = 1.8$  K, the LE is the only remaining line in the PL spectrum. This line is rather broad (its FWHM is approximately 7.5 meV; see Fig. 19a) and, according to [272], consists of three unresolved spectral components: the lines of localized and impurity-bound excitons and of localized biexcitons. With an increasing excitation level at sufficiently low temperatures (Fig. 19a) and with decreasing the temperature at sufficiently high excitation levels (Fig. 19b), a narrow line corresponding to the luminescence of excitonic molecules, designated as FBiE, occurs at the low-energy side of the exciton line FE. With a further increase in the pump intensity or a decrease in temperature, a broad line of the EHL luminescence appears at the low-energy tail of the FBiE line. The EHL line is dominant in the spectrum at high excitation levels and low temperatures.

The best agreement of the shape of the EHL emission line calculated according to Eqn (6) with the experimental lineshape (see the top curve in Fig. 19b) is attained if the calculation uses a three-dimensional density of states for electrons ( $D_e \propto E_e^{1/2}$ ) and a two-dimensional (energy-independent) density of states for holes. The Fermi energies of electrons and holes obtained from the lineshape analysis were  $E_{Fe} = 13$  meV and  $E_{Fh} = 7$  meV, which correspond to the electron and hole densities  $n_0 = 4.8 \times 10^{18} \text{ cm}^{-3}$  and  $p_0 = 8.5 \times 10^{11} \text{ cm}^{-2}$ . At this density, quasi-two-dimensional holes only occupy states in the lowest quantum-confinement subband (the heavy-hole subband hh), and the Fermi energy of quasi-three-dimensional electrons exceeds the height of the potential barrier in the conduction band (in this heterostructure, this height is  $\Delta E_c(\Delta_4) \approx 10$  meV [273, 274]). These electrons, which occupy the four  $\Delta_4$  minima in the conduction band of silicon located at the  $\langle 100 \rangle$  axes of the reciprocal lattice parallel to the plane of the strained SiGe layer, can tunnel into this layer, where the bottom of the conduction band is formed by the four  $\langle 100 \rangle$  energy minima of the same symmetry (as we can see in Fig. 20b, the maximum of the electron density occurs at the center of the SiGe layer).<sup>12</sup> We

<sup>12</sup> The energy band diagrams shown in Fig. 20 are plotted based on the results obtained in [274, 275].

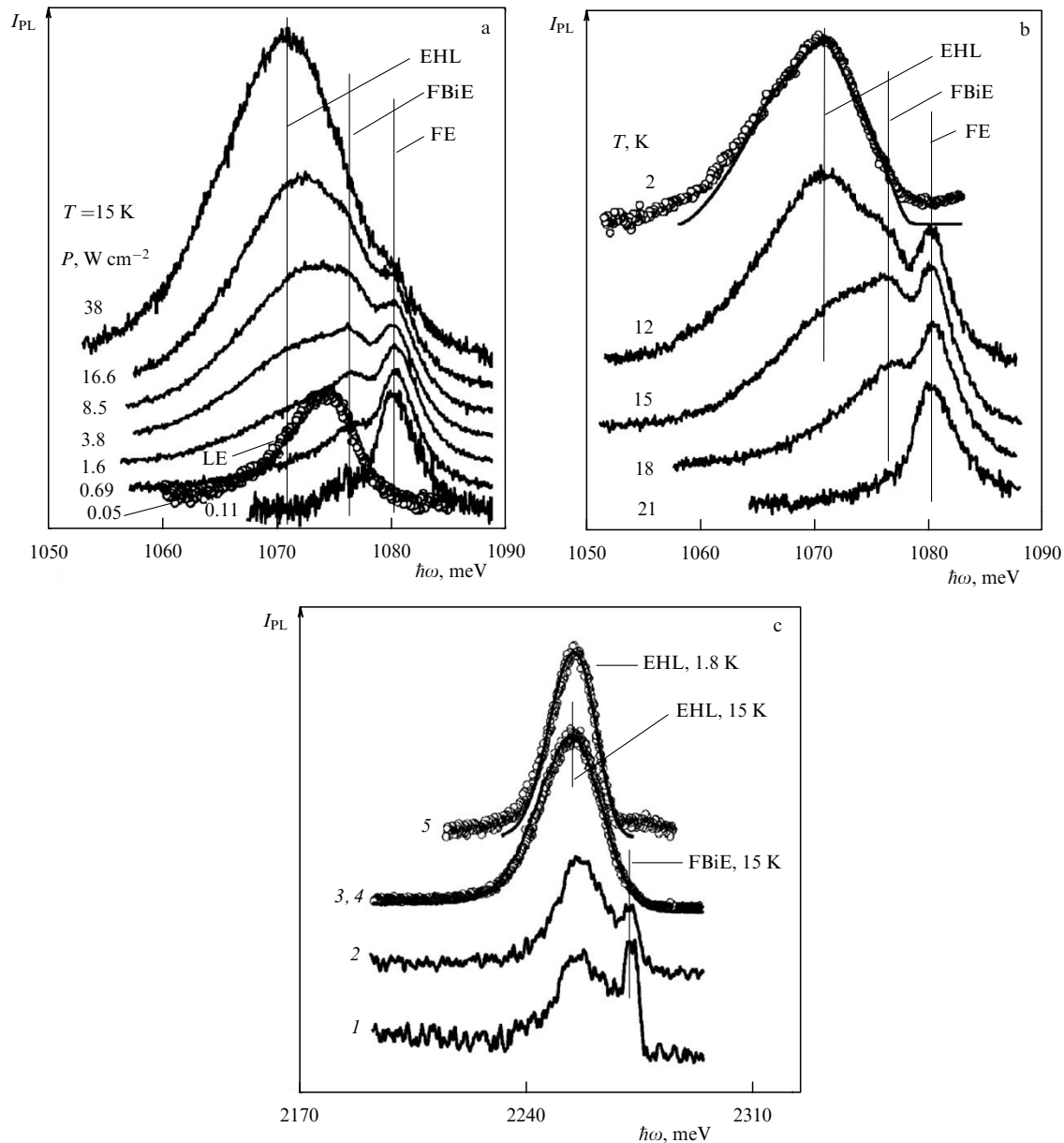


**Figure 19.** TO phonon components in the PL spectrum of a 2 nm thick  $\text{Si}_{1-x}\text{Ge}_x$  layer ( $x = 0.09$ ) versus (a) the excitation density  $P$  and (b) the temperature  $T$  [270] and (c) normalized spectra of  $2E_g$  luminescence [280]. The emission lines of free excitons, biexcitons, and the electron–hole liquid are marked FE, FBiE, and EHL; LE is the emission line of localized excitons. All spectra in panel (a) apart from LE are recorded at  $T = 15$  K and normalized to the intensity of the FE peak. The LE spectrum, shown by circles, is recorded at  $T = 2$  K. All spectra in panel (b) apart from the top one are recorded at  $P = 3.8$  W cm $^{-2}$  and  $T = 12$ – $21$  K. The top spectrum: circles are the experimental data recorded at  $T = 2$  K and  $P = 8.5$  W cm $^{-2}$  and the solid line is the theoretical fit for the EHL line shape. In panel (c), the pump intensity is (1)  $P = 0.5$ , (2)  $1.0$ , (3)  $85$ , and (4)  $150$  W cm $^{-2}$  and the temperature is  $T = 15$  K. Spectra 3 (circles,  $P = 85$  W cm $^{-2}$ ) and 4 (solid line,  $P = 150$  W cm $^{-2}$ ) are superimposed. Spectrum 5 was recorded at  $T = 1.8$  K and  $P = 26$  W cm $^{-2}$  (circles); here, the solid line shows the curve obtained by self-convolution of the experimental one-electron spectrum that was recorded in the near-infrared range.

note that excitons in type-II Si/SiGe/Si heterostructures are also formed from  $\Delta_4$  electrons and heavy holes. The work function of excitons in the EHL, estimated as the energy difference between the spectral positions of the free-exciton PL line (the FE line in Figs 19a, b) and the high-energy edge of the EHL line (see the topmost curve in Fig. 19b) is  $\varphi \approx 3$  meV.

The ratio of the hole and electron densities is  $p_0/n_0 \approx 1.8$  nm  $< d = 2$  nm; i.e., it is smaller than the SiGe layer thickness. This probably means that the electron density is distributed nonuniformly along the direction perpendicular to the layer plane. It is also noteworthy that the electron

density  $n_0$  in the EHL observed in strained quasi-two-dimensional SiGe layers is considerably higher than that in bulk unstrained silicon. Apparently, this increase in the liquid density is related to its quasi-two-dimensional nature. The critical temperature of the exciton–gas–EHL transition estimated from the experimental data is  $T_c = 18$ – $20$  K.

To obtain additional evidence that the interpretation of the spectral lines attributed to the biexciton and EHL luminescence is correct, the spectra of the PL in the visible range were measured. Visible-range luminescence ( $2E_g$  luminescence) results from so-called two-electron transi-

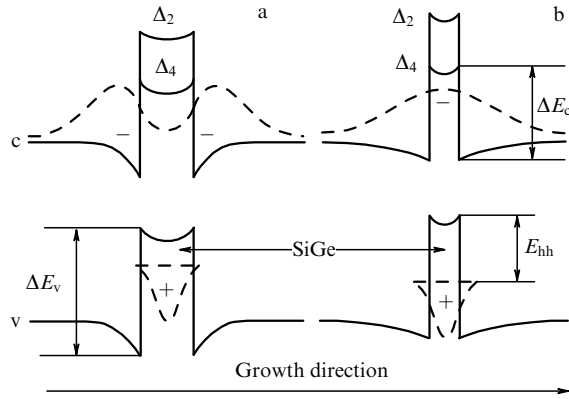


**Figure 20.** Outline of the band diagram of Si/Si<sub>1-x</sub>Ge<sub>x</sub>/Si heterostructures with  $x = 0.09$  and SiGe layer thicknesses of (a)  $d = 4$  nm and (b)  $d = 2$  nm. Dashed lines show the electron and hole density distributions along the direction perpendicular to the layer and the heavy-hole quantum-confinement level in the QWs of these structures [280].

tions, whereby two electrons and two holes recombine simultaneously with the emission of one photon whose energy equals the total energy of the four recombining particles [272, 276, 277].<sup>13</sup> Comparing one- and two-electron PL spectra allows identifying the origins of different lines in the conventional (one-electron) spectra more reliably, because emission lines that correspond to objects containing less than two electron–hole pairs cannot occur in two-electron spectra.

In these experiments, the CW photoexcitation of the structures was performed with a Ti:sapphire laser at the wavelength  $\lambda = 0.75$   $\mu\text{m}$ . The photon energy of this radiation is considerably lower than that of the  $2E_g$  luminescence in the structures under study and therefore excited states with energies of the order of  $2E_g$  cannot be populated under these pumping conditions. The  $2E_g$  luminescence spectra of the structure with a 2 nm thick SiGe layer are shown in Fig. 19c [279, 280]. At relatively low excitation levels, the spectra feature a narrow line whose spectral position corresponds to the luminescence line attributed to biexcitons in the one-electron PL spectra recorded in the near-infrared range (Figs 19a, b). With increasing the excitation level, the line corresponding to the  $2E_g$  luminescence of the EHL arises in the low-energy tail of the biexciton line. The shapes of normalized spectra 3 and 4 are the same; hence, the shape of the spectrum becomes independent of the pump level, which is a characteristic signature of EHL luminescence.

The spectral density  $J_2(\hbar\omega)$  of radiation emitted in two-electron transitions can be calculated as the self-convolution of the spectral density  $J_1(\hbar\omega)$  in the TO (or any other) component of the spectrum corresponding to one-electron transitions [276, 279]:

$$J_2(\hbar\omega) \propto \int J_1(\hbar\omega') J_1[(\hbar\omega - 2\hbar\Omega) - \hbar\omega'] d\omega', \quad (21)$$

where  $\hbar\Omega$  is the TO phonon energy. The spectrum  $J_2$  obtained according to this expression from the experimental spectrum

<sup>13</sup> It should be mentioned that similarly to one-electron transitions, the rate of two-electron transitions can be considerably increased as a result of interaction with localized surface plasmons [278].

$J_1$  nearly coincides with the  $2E_g$  spectrum 5 (Fig. 19c) recorded in the visible range. This means that the broad PL lines observed in the near-infrared and the visible spectral ranges originate from the same radiating object, i.e., in this case, the EHL.

Therefore, a spatially direct quasi-two-dimensional EHL can form at high excitation levels and low temperatures ( $T < T_c$ ) in type-II Si/SiGe/Si heterostructures with an SiGe layer that is sufficiently thin to be tunneling-transparent to electrons.

We note that the combined analysis of one- and two-electron PL spectra shown in Fig. 19 allows obtaining the excitonic-molecule binding energy with high accuracy. Without going into details (see [267, 279]), we only report here that the binding energy of free quasi-two-dimensional biexcitons in a strained 2 nm thick SiGe layer determined in this way is  $E_M = (2.0 \pm 0.5)$  meV. This value is noticeably higher than the binding energy of free biexcitons in the three-dimensional case (in bulk uniaxially strained Si,  $E_M = 1.3 - 1.4$  meV [281]).

The behavior of the PL spectra of the Si/Si<sub>1-x</sub>Ge<sub>x</sub>/Si heterostructure with  $d = 2$  nm and  $x = 0.09$  under an increase in the excitation level, described above, should now be compared with the completely different behavior observed for structures with  $d = 4$  nm,  $x = 0.09$  and  $d = 2$  nm,  $x = 0.25$ . The one-electron PL spectra of these two heterostructures feature no-phonon lines of localized excitons LE(NP) and their phonon replicas LE(TA), LE(TO<sub>Si-Si</sub>), and LE(TO<sub>Si-Ge</sub>) corresponding to the emission of transverse acoustic (TA) and transverse optical (TO) phonons that belong to Si–Si and Si–Ge vibration modes. We can see that the transformation of these spectra with increasing the excitation level mainly consists in a blue shift of the exciton lines corresponding to the SiGe layer; this shift is especially pronounced in the structure with a higher Ge content. The blue shift originates from band bending caused by the Coulomb field of spatially separated electrons and holes and is usually believed to be a signature of type-II structures [282]. At high pump levels, the exciton lines corresponding to the SiGe layer acquire long-wavelength tails, which are especially pronounced for the no-phonon components. However, no evidence of the occurrence of the EHL at pump levels comparable to those presented in Figs 19a, b can be observed.

The difference among the heterostructures whose PL spectra have been discussed here lies in the tunneling transparency of the potential barriers that prevent electrons from entering the SiGe layer. The difference in the depth of the QW for holes is apparently unimportant in this case. The probability that a particle passes through a potential barrier can be estimated from the uncertainty relation: the uncertainty in the kinetic energy of an electron moving in the barrier has to exceed the barrier height  $\Delta E_c$  (see, e.g., [283]); hence, the barrier is transparent when  $\Delta E_c(\Delta_4) d^2 < \hbar^2/(8m) \approx 50$  meV nm<sup>2</sup> (here,  $m$  is the effective mass of  $\Delta_4$  electrons in the direction perpendicular to the SiGe layer). For a structure with  $d = 2$  nm and  $x = 0.09$ , the expression in the left-hand side of the inequality evaluates as approximately 40 meV nm<sup>2</sup>, and the barrier is transparent for electrons. For the other two structures, with  $d = 2$  nm and  $x = 0.25$  and with  $d = 4$  nm and  $x = 0.09$ , this expression gives approximately 110 and 160 meV nm<sup>2</sup>; thus, the above inequality is not satisfied and nonequilibrium electrons in these structures reside mainly in silicon in the vicinity of the Si/SiGe heterointerfaces [270]. The energy band diagrams and the plots of the electron and hole density distributions for the



structures with  $x = 0.09$  and  $d = 4$  and  $2$  nm are shown schematically in Fig. 20.

**3.5.3 Impact of the barrier in the conduction band on the properties of spatially direct EHL.** The impact of the height of the barrier in the conduction band formed by the SiGe layer on the properties of the electron–hole system in Si/SiGe/Si structures and, in particular, on the existence of a spatially direct EHL and on its characteristics was investigated in detail in experiments with a number of structures containing a 5 nm thick SiGe layer with different Ge contents  $x$  [284–290]. We first consider the results obtained for structures of this type with  $x = 0.05$ . The emergence of the EHL luminescence line with increasing the excitation intensity in the PL spectra of these structures was observed in [286]. According to the lineshape analysis of the no-phonon EHL luminescence component in the near-infrared spectral range, which was carried out assuming that both electrons and holes are characterized by two-dimensional densities of states and using an expression from [291] taking homogeneous broadening into account (see [267, 285, 286] for details), the density of this quasi-two-dimensional EHL is  $n_0 \approx 10^{12} \text{ cm}^{-2}$ . Further evidence of the formation of the EHL was obtained from the spectra of  $2E_g$  luminescence.

As the pump density increases beyond a certain level, the luminescence spectrum broadens and, instead of two lines (corresponding to the EHL and free excitons), features a single band whose width increases with the pump density. This band originates from the EHP luminescence [286]. In an earlier study [285], the formation of EHP in the SiGe layer of this structure was investigated at temperatures exceeding the EHL critical temperature  $T_c \approx 20$  K. The authors demonstrated that the exciton–gas–EHP transition (Mott transition) has a smooth character.

Information on the dynamic properties of the electron–hole system was obtained from measurements of the decay kinetics of QW luminescence [286]. Kinetic dependences were recorded at four different positions across the Si–Ge luminescence spectrum (labeled 1–4 in the inset in Fig. 21). Points 1–3 correspond to the EHP/EHL luminescence line, and point 4 corresponds at longer times to the exciton line. The kinetic dependences are shown in Fig. 21. Immediately after the excitation pulse ( $t < 0.3$ – $0.4 \mu\text{s}$ ), photoexcited electrons and holes form an EHP, and, at short times, all kinetic curves reflect dynamic processes in the plasma. At longer times ( $t > 1.5 \mu\text{s}$ ), kinetic curves 1–3 correspond to EHL luminescence and run parallel to each other. This means that the shape of the EHL luminescence line remains unchanged in the course of electron–hole recombination in the liquid. A two-exponential fit to the experimental data, which proved to be quite satisfactory for  $t > 0.5 \mu\text{s}$ , yielded time constants  $\tau_0 \approx 0.4 \mu\text{s}$  and  $\tau_{\text{cap}} \approx 0.95 \mu\text{s}$ . These were respectively interpreted by the authors as the lifetime of electrons and holes in the EHL and the characteristic time of exciton capture by the QW (excitation laser pulses generated electron–hole pairs mainly in the Si layers of the structure). The value of  $\tau_{\text{cap}}$  is close to (although somewhat lower than) the exciton lifetime in bulk silicon.

Thus, the lifetime of the electron–hole system in a QW is determined by its feeding by excitons from the Si layers, and the duration of this process is determined by the lifetime of excitons in silicon. We note that the probability of recombination in a dense EHP is proportional to the square of its density (Auger recombination; see Section 2.6). The EHP density

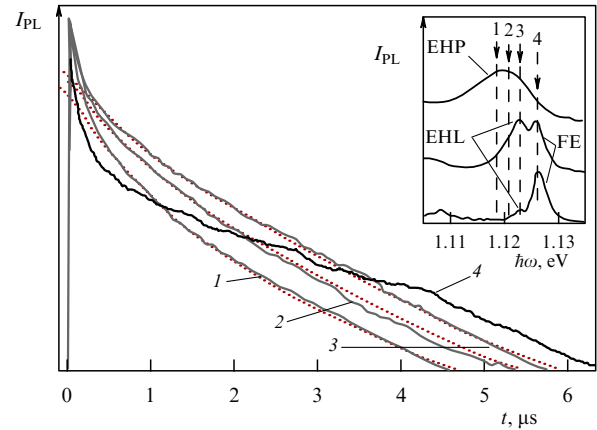


**Figure 21.** Decay kinetics of the QW luminescence in the SiGe structure with  $d = 5$  nm and  $x = 0.05$  at the four spectral points shown in the inset;  $T = 15$  K. Curves 1–3 correspond to the respective EHP<sub>NP</sub> and EHL<sub>NP</sub> bands at  $t < 0.5 \mu\text{s}$  and  $t > 0.5 \mu\text{s}$ ; curve 4 corresponds to the respective EHP<sub>NP</sub> band and the FE<sub>NP</sub> line at  $t < 0.5 \mu\text{s}$  and  $t > 0.5 \mu\text{s}$ . The dotted lines show two-exponential fits to the decay curves. Inset: the no-phonon component of the QW luminescence spectrum recorded under CW excitation of the structure; the excitation density  $P = 0.02$ ,  $1.1$ , and  $340 \text{ W cm}^{-2}$  (from bottom up) [286].

decreases and hence the lifetime of the constituent particles increases in the course of recombination. In contrast to EHP, the EHL density remains unchanged, while the volume occupied by the liquid decreases with a constant lifetime. The kinetic dependence for exciton luminescence (Fig. 21, curve 4) features a region (between  $1 \mu\text{s} < t < 4.4 \mu\text{s}$ ) where the emission intensity decreases relatively slowly with time. Probably, similarly to bulk germanium, the decay of the exciton population is slowed down in this time range owing to the evaporation of the EHL drops (see Section 2.6). At longer times, the kinetic dependence for the exciton luminescence runs parallel to those corresponding to the EHL. This behavior supports the assumption that the electron–hole system in the QW is fed with excitons from the Si layers. Earlier, a similar conclusion was reached in investigating PL in deeper Si/SiGe QWs [292]. We note that excitons reaching the QW from the Si layers are very rapidly captured by EHDs. Experiments on the evaporation of EHDs by heat pulses demonstrate that equilibrium is restored within a few dozen nanoseconds [293].

Further insight into the time evolution of the electron–hole system after the excitation pulse can be gained by analyzing time-resolved luminescence spectra. Figure 22 shows the PL spectra of the structure with  $d = 5$  nm and  $x = 0.05$  recorded at different times after the excitation by a pulse of the third harmonic of an Nd:YAG laser (emission wavelength 355 nm and pulse duration 5 ns) [288]. For delay times  $t < 330$  ns, the spectra feature lines corresponding to the EHP (EHP<sub>NP</sub>(QW) and EHP<sub>TO</sub>(QW)), whose intensity and width decrease with time. In the time range  $t = 330$ – $1000$  ns, the line shape and the instantaneous lifetime of the EHP remain unchanged. This means that the plasma density remains the same in the course of the recombination of its constituent particles, which is a signature of the EHL. Within this time interval, free-exciton luminescence lines (FE<sub>NP</sub>(QW) and FE<sub>TO</sub>(QW)) begin to emerge in the spectrum; this indicates that separation into the exciton–gas and EHL phases takes place. Subsequently, the EHL and the free-exciton luminescence decay at different

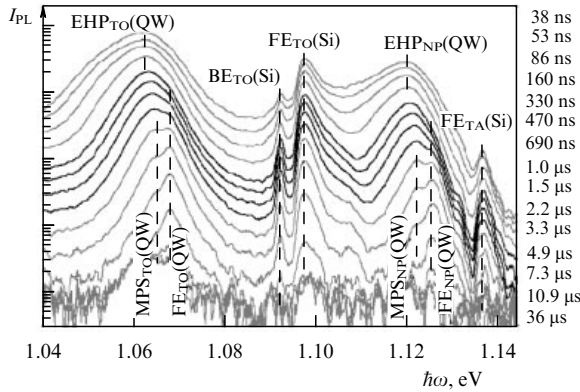


**Figure 22.** Luminescence spectra of the structure with  $d = 5$  nm and  $x = 0.05$  recorded at various delay times  $t$  after the excitation pulse (the values of  $t$  are indicated along the right edge of the plot);  $T = 15$  K.  $BE_{TO}$  and  $MPS$  designate the respective lines of bound excitons (TO component) and multiparticle states. The spectra recorded during the time interval  $t = 330 - 1000$  ns, where the EHP density remains constant, are shown in black [288].

rates and, at long times (exceeding  $3.3 \mu s$ ), the QW luminescence spectrum consists only of the lines of free excitons and exciton complexes (the lines corresponding to the latter are designated in Fig. 22 as  $MPS_{NP}(QW)$  and  $MPS_{TO}(QW)$ ). The exciton complexes can be biexcitons that form in the QW at high exciton densities or trions at low densities [288].

The properties and behavior of the electron–hole system in the SiGe layers of Si/SiGe/Si structures with  $d = 5$  nm and different Ge contents were investigated in [287, 288]. The luminescence spectra of these structures in the near-infrared and visible spectral ranges are shown in Figs 23a, b. For  $x < 6.9\%$ , the QW luminescence spectra in the near-infrared region (the TO component is shown in Fig. 23a) feature the EHL and free exciton lines. With decreasing the Ge content, the EHL luminescence line shifts to lower energies with respect to the exciton line, while the intensity of the exciton luminescence line increases compared to that of the EHL line. The low-energy shift of the EHL line is also observed in  $2E_g$  spectra (Fig. 23b). For relatively high values of the Ge content in the SiGe layer ( $x = 9.6$  and  $13.8\%$ ), the PL spectra feature a single line whose peak occurs near the bottom of the exciton band (and near the doubled exciton energy in the  $2E_g$  spectra).

As mentioned above, Si/SiGe/Si structures with low  $x$  belong to type II, with the strained SiGe layer representing a potential barrier for electrons. In structures with  $x = 9.6$  and  $13.8\%$ , this barrier is sufficiently high to keep nonequilibrium electrons in the Si layers in the vicinity of the Si/SiGe heterointerfaces. Thus, electrons are spatially separated from nonequilibrium holes, which are confined in the QW within the alloy layer (Fig. 20a). The luminescence observed in these structures (Figs 23a, b) occurs upon the recombination in the EHP in this electron–hole bilayer.\* With a decrease in the Ge content, the potential barrier becomes lower and electrons begin to enter the SiGe layer. As a result, spatially direct excitons and a spatially direct EHL can form in this layer. The fact that, upon a decrease in the barrier height

(reduction in  $x$ ), the EHL forms in the layer prior to the formation of excitons (Fig. 23a) is evidently a consequence of a considerable decrease in the barrier height owing to band gap renormalization within the volume occupied by the EHL (see Section 2.1).

The curves plotted in Fig. 23b by dashed lines show the results of a theoretical analysis of experimental spectra. The authors wrote the expression for the spectral density of the  $2E_g$  luminescence as the convolution of the theoretical spectral distribution in the near-infrared region according to [291] (see above); the corresponding formulas and other details of the lineshape analysis are available in [287]. It is important that the two-dimensional character of the density of states was assumed in these calculations for both electrons and holes. The density of the quasi-two-dimensional EHL in these QWs determined from this analysis is  $n_0 = 1.1 \times 10^{12}$  and  $0.97 \times 10^{12} \text{ cm}^{-2}$  for the respective structures with  $x = 3.5\%$  and  $5\%$ . The  $2E_g$  luminescence spectra of the structures with  $x \geq 6.9\%$  (Fig. 23b) could not be described by the two-dimensional EHL model. The exciton work function in the EHL (the binding energy per electron–hole pair in the liquid) was determined as half the energy spacing between the doubled exciton-transition energy and the high-energy edge of the theoretical fit to the spectrum of the  $2E_g$  luminescence of the EHL (Fig. 23b). The dependence of the work function on the Ge content in the SiGe layer is shown in Fig. 23c. It is noteworthy that the exciton work function in the quasi-two-dimensional EHL in the structure with  $x \approx 3\%$ , which is approximately 6 meV, is considerably higher (by a factor of 3) than that in bulk uniaxially strained silicon (see the table). The higher binding energy of particles in the liquid and its high density in the structures under study are apparently related to its quasi-two-dimensional nature.

Additional evidence in favor of this picture of the formation of the EHL in heterostructures with different Ge contents in the SiGe layer was obtained from measurements of time-resolved PL spectra. The results obtained for the structure with  $x = 0.05$  were discussed above (see Fig. 22). Similar measurements were carried out for structures with the same thickness of the SiGe layer ( $d = 5$  nm) and  $x = 3.5\%$ ,  $7\%$ , and  $9.5\%$  [288]. For the structure with  $x = 3.5\%$ , these measurements demonstrated that upon a decrease in the density of the EHP in the course of recombination of its constituent particles, the EHL begins to form at much earlier times than it does in the structure with  $x = 5\%$  and is clearly present over a longer time interval. In the structure with  $x = 7\%$ , the kinetic behavior of the electron–hole system is almost the same as in the structure with  $x = 5\%$ , while in the structure with  $x = 9.5\%$ , the EHL luminescence line is not observed at all. Therefore, a decrease in the EHP density in the process of recombination leads to the appearance of excitons, and hence the EHP–exciton–gas phase transition occurs. Thus, the kinetic behavior of the electron–hole system in the QWs of structures that differ in the Ge content in the SiGe layer agrees with the picture inferred from the results shown in Fig. 23.

Summarizing the discussion of the properties of the electron–hole system in QWs of Si/SiGe/Si heterostructures, considered here in the example of structures with a 5 m thick SiGe layer, we again emphasize that the formation of the EHL in these structures is governed by the height of the potential barrier for electrons in the SiGe layer. If this barrier is sufficiently low, such that electrons from the Si layers can enter the SiGe layer, a spatially direct quasi-two-dimensional

\* Rather, a trilayer, because there are electron layers at both Si/SiGe heterointerfaces and a hole layer between. This is, however, of minor importance for the subsequent discussion. (Author's note added to the English translation.)

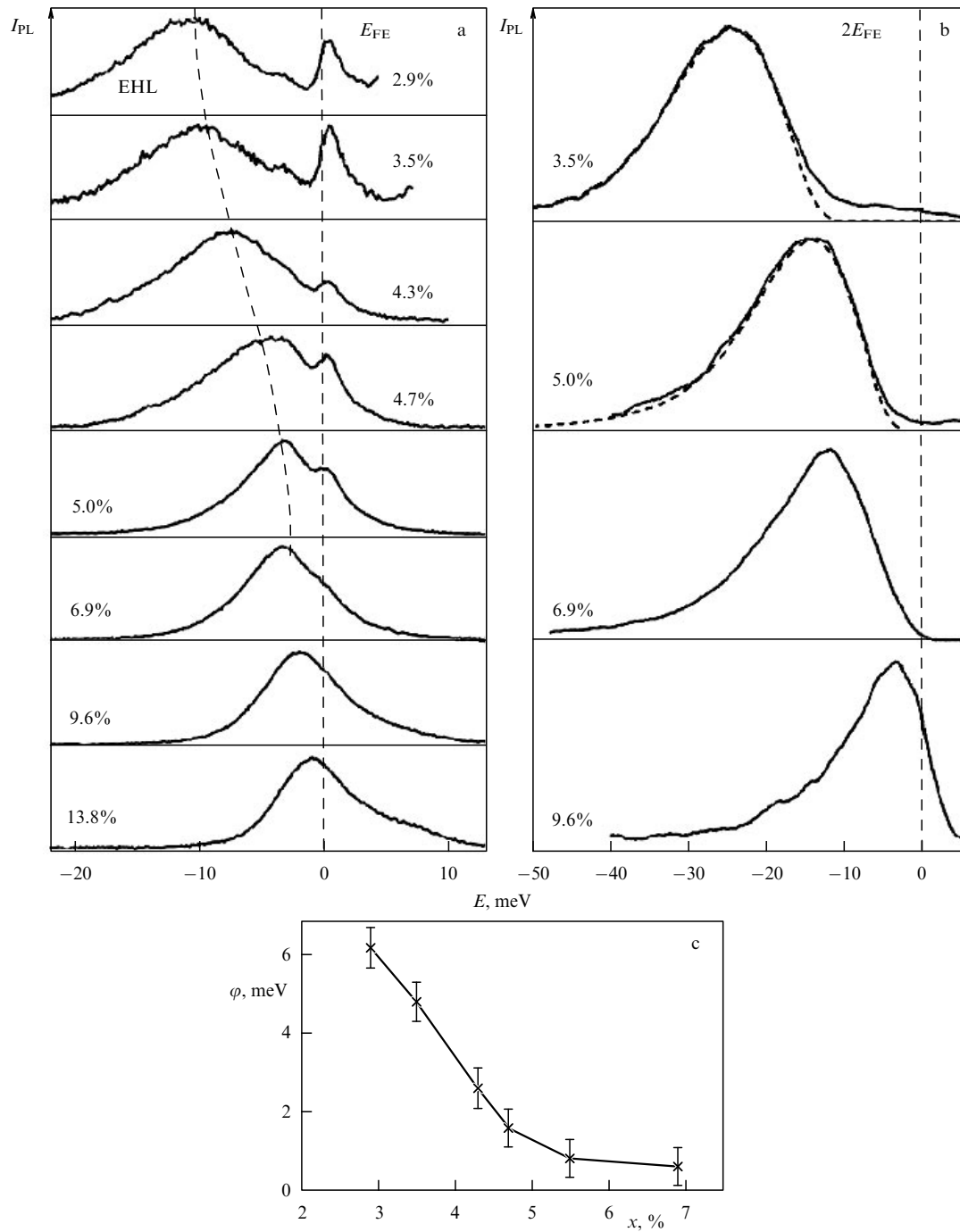


**Figure 23.** QW luminescence spectra of structures with  $d = 5$  nm and different Ge contents in the SiGe layer (indicated on the plot). (a) TO-phonon replicas of the one-electron spectra for  $P = 0.2 \text{ W cm}^{-2}$  and  $T = 10 \text{ K}$ . (b)  $2E_g$  spectra for  $T = 2 \text{ K}$  and  $P = 2 \text{ W cm}^{-2}$ ; curves plotted by dashed lines show the theoretical fits to the corresponding experimental spectra for  $x = 3.5\%$  and  $5\%$ . The energy zero is taken at (a) the position of the free-exciton line and (b) the doubled exciton energy. (c) Exciton work function in the EHL in QWs with the thickness  $d = 5$  nm as a function of the Ge content in the SiGe layer [287].

EHL can form in this layer and the density and binding energy of this EHL increase with decreasing the barrier height.

**3.5.4 Spatially indirect (dipolar) EHL.** In the foregoing, we discussed the formation of a spatially direct EHL, where the electrons and holes are ‘intermingled’ and occupy the same region of space. We now consider experimental results providing evidence of the formation of a spatially indirect (dipolar) EHL in electron–hole bilayers at Si/SiGe hetero-

interfaces upon the photoexcitation of the structure [279, 280, 294]. The experiments were carried out on the same structure with  $d = 4$  nm and  $x = 0.09$  that was discussed in Section 3.5.2, but at much higher excitation levels. The PL spectra of the structure in the near-infrared and visible ranges are shown in Figs 24a, b. At high temperatures ( $T = 23$  and  $26 \text{ K}$ ) and low excitation levels, the one-electron PL spectrum features only the line of free spatially indirect (dipolar) excitons (Fig. 24a). As the temperature decreases, the luminescence line of

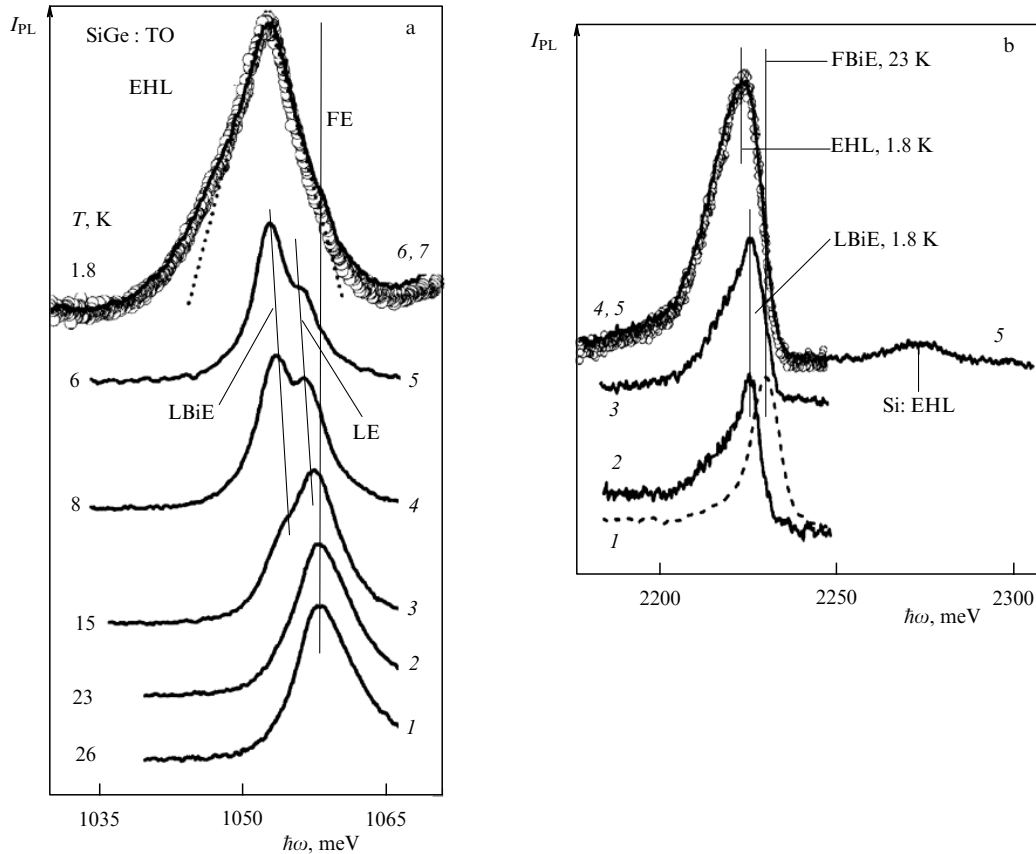


**Figure 24.** Normalized PL spectra of the structure with  $d = 4\text{ nm}$  and  $x = 0.09$  in the (a) near-infrared and (b) visible spectral ranges at various temperatures and excitation levels. (a) Curves 1–5:  $P = 0.12\text{ W cm}^{-2}$ ,  $T$  varies from 26 to 6 K. Curves 6 (circles) and 7 (solid line):  $P = 85\text{ W cm}^{-2}$  and  $170\text{ W cm}^{-2}$ , respectively, and  $T = 1.8\text{ K}$ ; the two spectra are superimposed. The dotted line shows the calculated lineshape of dipolar EHL luminescence. (b) Spectra 2–5 were recorded at  $T = 1.8\text{ K}$  and excitation levels (2)  $P = 3.8$ , (3) 13, (4) 108, and (5)  $180\text{ W cm}^{-2}$ ; curves 4 (circles,  $P = 108\text{ W cm}^{-2}$ ) and 5 (solid line,  $P = 180\text{ W cm}^{-2}$ ) are superimposed. Curve 1 (dashed line) shows the line of free dipolar biexcitons recorded at  $T = 23\text{ K}$  and  $P = 3.5\text{ W cm}^{-2}$  [294].

localized biexcitons appears in the low-energy tail of this line. At low temperatures, the biexciton line has a higher intensity than the exciton line. The red shift of both lines with decreasing temperature is caused by the localization of these particles. In the temperature range  $T < 6\text{ K}$  and at high pump levels, an intense PL line emerges whose shape and spectral position become independent of the pump intensity as it is increased further (Fig. 24a, curves 6 and 7). The peak of this line occurs approximately  $5.4\text{ meV}$  lower in energy than the free-exciton line that is observed at high temperatures. The dashed line shows the result of a theoretical fit of the shape of this line, assuming two-dimensional densities of states for electrons and holes in Eqn (6). A similar line arises under the same conditions in the spectra of  $2E_g$  luminescence. The emergence of this line with increasing the excitation level is shown in Fig. 24b. Similarly to the line arising in the near-infrared luminescence spectrum, its shape and spectral position are independent of the pump intensity (Fig. 24b, curves 4 and 5). Summarizing the experimental facts, we can conclude that the luminescence lines observed in the near-infrared and visible spectral ranges under high pump intensities belong to the quasi-two-dimensional dipolar EHL with the critical temperature  $T_c \approx 6\text{ K}$ . At high temperatures, the  $2E_g$  luminescence spectrum features only the line of dipolar biexcitons [Fig. 24b, curve 1 ( $T = 23\text{ K}$ )]. A detailed study of the formation of dipolar excitonic molecules in similar heterostructures was reported in [295].

#### 4. Conclusions

Our discussion has embraced a wide range of issues related to the properties and behavior of nonequilibrium electron–hole systems, and, first and foremost, to exciton condensation and properties of the EHL in bulk semiconductors and low-dimensional (primarily, two-dimensional) structures. Because of the inevitably limited length of this review, a significant number of the problems were discussed very briefly, and many important and interesting topics (multi-component EHL, Fermi-liquid properties of the EHL, possible types of phase diagrams, EHL in materials other than Ge and Si, and a large number of others) were passed by almost without consideration. Many of these issues are analyzed in detail in the review publications cited in the Introduction and throughout this paper.

The part of this review that covers exciton condensation in bulk materials is mostly retrospective. Contemporary studies in this field are rare and, although a number of new interesting results have been obtained, they have not led to considerable changes in the basic concepts and established views. At the same time, in our view, there are interesting problems that call for further experimental studies. One of them is the search for an insulating EHL and a metal–insulator transition in the liquid phase itself under the action of a magnetic field (see review [101]). Observation of the EHL in narrow-gap semiconductor materials like lead and tin chalcogenides,

which have direct-gap multivalley electron spectra and high permittivity, would be of significant interest; the formation of the EHL in these semiconductors could result in an essential rearrangement of their energy spectrum [296].

An attractive idea is to investigate ways to artificially increase the anisotropy of the electron spectrum in order to obtain a liquid with a large binding energy. Such a possibility can be realized, in particular, in quasi-one-dimensional and quasi-two-dimensional systems [20].

Comparing the parts of this review addressing bulk materials and low-dimensional structures, it can be seen that the studies of the EHL in the latter are actually at a very early stage. The possibility of controlling the electron energy spectrum by varying the structure design and selecting appropriate materials offers much promise for the search of new properties of electron–hole systems. In particular, the opportunity arises to obtain more complicated phase diagrams than those discussed in Section 2.3 (see Keldysh's papers [16, 83]), e.g., diagrams describing a phase transition between a degenerate Bose gas and an EHL.<sup>14</sup> It is certainly of interest to investigate the possibility of the transition from a metallic to a dielectric liquid (see Section 3.2) under a change in the parameters of an electron–hole bilayer or under external perturbations. And, without a doubt, we can expect much that is new and interesting from studies of phase transitions in electron–hole systems with a Dirac electron spectrum.

This article is a tribute to the outstanding scientist and person Leonid Veniaminovich Keldysh. A deep appreciation of him and the memory of our long-lasting collaboration and companionship will stay with me forever.

I am sincerely grateful to A S Alekseev, V S Bagaev, T M Burbaev, M L Skorikov, S G Tikhodeev, and V A Tsvetkov for the longtime collaboration and numerous discussions of the issues covered in this review and to M V Kochiev for his help in preparing it for publication.

## References

- Keldysh L V, in *Proc. of the 9th Intern. Conf. on Physics of Semiconductors, Moscow, July 23–29, 1968* Vol. 2 (Ed. S M Ryvkin) (Leningrad: Nauka, 1968) p. 1303; Keldysh L V, in *Trudy Devyatoi Mezhdunarodnoi Konf. po Fizike Poluprovodnikov, Moskva, 23–29 Iyulya 1968 g.* Vol. 2 (Ed. S M Ryvkin) (Leningrad: Nauka, 1968) p. 1387
- Keldysh L V *Sov. Phys. Usp.* **13** 292 (1970); *Usp. Fiz. Nauk* **100** 514 (1970)
- Keldysh L V, in *Eksitony v Poluprovodnikakh* (Excitons in Semiconductors) (Ed. B M Vul) (Moscow: Nauka, 1971) p. 5
- Leys F E et al. *Phys. Rev. B* **66** 073314 (2002)
- Pokrovskii Ya E, Svistunova K I *JETP Lett.* **9** 261 (1969); *Pis'ma Zh. Eksp. Teor. Fiz.* **9** 435 (1969)
- Bagaev V S et al. *JETP Lett.* **10** 195 (1969); *Pis'ma Zh. Eksp. Teor. Fiz.* **10** 309 (1969)
- Vavilov V S, Zayats V A, Murzin V N *JETP Lett.* **10** 192 (1969); *Pis'ma Zh. Eksp. Teor. Fiz.* **10** 304 (1969)
- Asnin V M, Rogachev A A *JETP Lett.* **9** 248 (1969); *Pis'ma Zh. Eksp. Teor. Fiz.* **9** 415 (1969)
- Haynes J R *Phys. Rev. Lett.* **17** 860 (1966)
- Kaminskii A S, Pokrovskii Ya E *JETP Lett.* **11** 255 (1970); *Pis'ma Zh. Eksp. Teor. Fiz.* **11** 381 (1970)
- Rice T M, in *Solid State Physics* Vol. 32 (Eds H Ehrenreich, F Seitz, D Turnbull) (New York: Academic Press, 1977) p. 1; Translated into Russian: Rice T M, in Rice T M, Hensel J C, Phillips T G, Thomas G A *Electronno-Dyrochnaya Zhidkost' v Poluprovodnikakh* (Electron–Hole Liquid in Semiconductors) (Moscow: Mir, 1980) p. 11
- Hensel J C, Phillips T G, Thomas G A, in *Solid State Physics* Vol. 32 (Eds H Ehrenreich, F Seitz, D Turnbull) (New York: Academic Press, 1977) p. 87; Translated into Russian: Hensel J C, Phillips T G, Thomas G A, in Rice T M, Hensel J C, Phillips T G, Thomas G A *Electronno-Dyrochnaya Zhidkost' v Poluprovodnikakh* (Electron–Hole Liquid in Semiconductors) (Moscow: Mir, 1980) p. 101
- Jeffries C D, Keldysh L V (Eds) *Electron–Hole Droplets in Semiconductors* (Modern Problems in Condensed Matter Sciences) Vol. 6 (Amsterdam: North-Holland, 1983); Translated into Russian: Jeffries C D, Keldysh L V (Eds) *Electronno-Dyrochnye Kapli v Poluprovodnikakh* (Moscow: Nauka, 1988)
- Tikhodeev S G *Sov. Phys. Usp.* **28** 1 (1985); *Usp. Fiz. Nauk* **145** 3 (1985)
- Murzin V N *Submillimetrovaya Spektroskopiya Kollektivnykh i Svyazannykh Sostoyanii Nositelei Toka v Poluprovodnikakh* (Submillimeter Spectroscopy of Collective and Bound States of Charge Carriers in Semiconductors) (Moscow: Nauka, 1985)
- Keldysh L V *Contemp. Phys.* **27** 395 (1986)
- Keldysh L V, Sibeldin N N, in *Nonequilibrium Phonons in Non-metallic Crystals* (Modern Problems in Condensed Matter Science) Vol. 16 (Eds W Eisenmenger, A A Kaplyanskii) (Amsterdam: North-Holland, 1986) p. 455
- Sibeldin N N, in *Problems of Condensed Matter Physics: Quantum Coherence Phenomena in Electron–Hole and Coupled Matter–Light Systems* (International Series of Monographs on Physics, Vol. 139, Eds A L Ivanov, S G Tikhodeev) (Oxford: Oxford Univ. Press, 2008) p. 227
- Kulakovskii V D, Timofeev V B, in *Electron–Hole Droplets in Semiconductors* (Modern Problems in Condensed Matter Sciences, Vol. 6, Eds C D Jeffries, L V Keldysh) (Amsterdam: North-Holland, 1983) p. 95; Translated into Russian: Kulakovskii V D, Timofeev V B, in *Electronno-Dyrochnye Kapli v Poluprovodnikakh* (Eds C D Jeffries, L V Keldysh) (Moscow: Nauka, 1988) p. 86
- Andryushin E A et al. *JETP Lett.* **24** 185 (1976); *Pis'ma Zh. Eksp. Teor. Fiz.* **24** 210 (1976)
- Andryushin E A, Keldysh L V, Silin A P *Sov. Phys. JETP* **46** 616 (1977); *Zh. Eksp. Teor. Fiz.* **73** 1163 (1977)
- Andryushin E A, Silin A P *Sov. Phys. Solid State* **18** 1243 (1976); *Fiz. Tverd. Tela* **18** 2132 (1976)
- Andryushin E A *Sov. Phys. Solid State* **18** 1457 (1976); *Fiz. Tverd. Tela* **18** 2493 (1976)
- Lozovik Yu E, Yudson V I *JETP Lett.* **22** 11 (1975); *Pis'ma Zh. Eksp. Teor. Fiz.* **22** 26 (1975)
- Lozovik Yu E, Yudson V I *Sov. Phys. JETP* **44** 389 (1976); *Zh. Eksp. Teor. Fiz.* **71** 738 (1976)
- Lozovik Yu E, Berman O L *JETP* **84** 1027 (1997); *Zh. Eksp. Teor. Fiz.* **111** 1879 (1997)
- Moskalenko S A et al. *Phys. Rev. B* **66** 245316 (2002)
- Ye J J. *Low Temp. Phys.* **158** 882 (2010)
- Golden K I, Kalman G J *Phys. Rev. E* **88** 033107 (2013)
- Babichenko V S, Polishchuk I Ya *JETP Lett.* **97** 628 (2013); *Pis'ma Zh. Eksp. Teor. Fiz.* **97** 726 (2013)
- Babichenko V S, Polishchuk I Ya *Physica B* **453** 49 (2014)
- Babichenko V S, Polishchuk I Ya *J. Low Temp. Phys.* **180** 153 (2015)
- Berman O L, Kezerashvili R Ya, Ziegler K *Physica E* **71** 7 (2015)
- Babichenko V S, Polishchuk I Ya *Phys. Rev. B* **94** 165304 (2016)
- Sharma R O, Saini L K, Bahuguna B P *Phys. Rev. B* **94** 205435 (2016)
- Cinti F, Wang D-W, Boninsegni M *Phys. Rev. A* **95** 023622 (2017)
- Lozovik Yu E, Berman O L, Willander M J. *Phys. Condens. Matter* **14** 12457 (2002)
- Moskalenko S A et al. *Physica E* **19** 278 (2003)
- Dumanov E V, Gherciu L E *Phys. Status Solidi B* **250** 1432 (2013)
- Moskalenko S A et al. *Phys. Solid State* **55** 1563 (2013); *Fiz. Tverd. Tela* **55** 1457 (2013)
- Lobanov S V, Gippius N A, Butov L V *Phys. Rev. B* **94** 245401 (2016)
- Combescot M, Combescot R, Dubin F *Rep. Prog. Phys.* **80** 066501 (2017)

<sup>14</sup> See [297] for coherent states and Bose condensation of excitons under nonequilibrium conditions. This little-known paper by Keldysh is published in this issue of *Physics–Uspekhi* [298].

43. Nazarenko A V, Ogawa T, Sugakov V I *Phys. Status Solidi B* **228** 857 (2001)
44. Sugakov V I *Phys. Solid State* **46** 1496 (2004); *Fiz. Tverd. Tela* **46** 1455 (2004)
45. Shilo Y et al. *Nature Commun.* **4** 2335 (2013)
46. Chernyuk A A, Sugakov V I, Tomylko V V *Phys. Rev. B* **90** 205308 (2014)
47. Cohen K et al. *Nano Lett.* **16** 3726 (2016)
48. Andreev S V *Phys. Rev. B* **94** 165308 (2016)
49. Saini L K, Nayak M G *Adv. Mater. Res.* **665** 283 (2013)
50. Suris R A *JETP* **122** 602 (2016); *Zh. Eksp. Teor. Fiz.* **149** 695 (2016)
51. Saini L K *J. Low Temp. Phys.* **158** 515 (2010)
52. Nayak M G, Saini L K *Contrib. Plasma Phys.* **52** 211 (2012)
53. Kumar K, Moudgil R K *J. Phys. Condens. Matter* **24** 415601 (2012)
54. Nayak M G, Saini L K *Eur. Phys. J. B* **86** 3 84 (2013)
55. Golden K I et al. *Phys. Rev. E* **82** 036402 (2010)
56. Golden K I et al. *Contrib. Plasma Phys.* **52** 130 (2012)
57. Nikolaev V V, Portnoi M E *Phys. Status Solidi C* **1** 1357 (2004)
58. Nikolaev V V, Portnoi M E *Superlat. Microstruct.* **43** 460 (2008)
59. Schleede J et al. *Contrib. Plasma Phys.* **52** 819 (2012)
60. Asano K, Yoshioka T *J. Phys. Soc. Jpn.* **83** 084702 (2014)
61. Lozovik Yu E, Ogarkov S L, Sokolik A A *Phys. Rev. B* **86** 045429 (2012)
62. Phan V-N, Fehske H *New J. Phys.* **14** 075007 (2012)
63. Apinyan V, Kopeć T K *Phys. Scripta* **91** 095801 (2016)
64. Butov L V et al. *Nature* **417** 47 (2002)
65. Butov L V, Gossard A C, Chemla D S *Nature* **418** 751 (2002)
66. Butov L V, in *Problems of Condensed Matter Physics: Quantum Coherence Phenomena in Electron-Hole and Coupled Matter-Light Systems* (International Series of Monographs on Physics, Vol. 139, Eds A L Ivanov, S G Tikhodeev) (Oxford: Oxford Univ. Press, 2008) p. 83
67. Gorbunov A V, Timofeev V B *JETP Lett.* **80** 185 (2004); *Pis'ma Zh. Eksp. Teor. Fiz.* **80** 210 (2004)
68. Timofeev V B, Gorbunov A V *J. Appl. Phys.* **101** 081708 (2007)
69. Timofeev V B, Gorbunov A V *Phys. Status Solidi C* **5** 2379 (2008)
70. Gorbunov A V, Timofeev V B *Solid State Commun.* **157** 6 (2013)
71. Alloing M et al. *Europhys. Lett.* **107** 10012 (2014)
72. Littlewood P B, in *Problems of Condensed Matter Physics: Quantum Coherence Phenomena in Electron-Hole and Coupled Matter-Light Systems* (International Series of Monographs on Physics, Vol. 139, Eds A L Ivanov, S G Tikhodeev) (Oxford: Oxford Univ. Press, 2008) p. 163
73. Timofeev V B, in *Problems of Condensed Matter Physics: Quantum Coherence Phenomena in Electron-Hole and Coupled Matter-Light Systems* (International Series of Monographs on Physics, Vol. 139, Eds A L Ivanov, S G Tikhodeev) (Oxford: Oxford Univ. Press, 2008) p. 258
74. Zimmermann R, in *Problems of Condensed Matter Physics: Quantum Coherence Phenomena in Electron-Hole and Coupled Matter-Light Systems* (International Series of Monographs on Physics, Vol. 139, Eds A L Ivanov, S G Tikhodeev) (Oxford: Oxford Univ. Press, 2008) p. 285
75. Timofeev V B *Low Temp. Phys.* **38** 541 (2012); *Fiz. Nizk. Temp.* **38** 693 (2012)
76. Butov L V *JETP* **122** 434 (2016); *Zh. Eksp. Teor. Fiz.* **149** 505 (2016)
77. Moskalenko S A *Sov. Phys. Solid State* **4** 199 (1962); *Fiz. Tverd. Tela* **4** 276 (1962)
78. Blatt J M, Böer K W, Brandt W *Phys. Rev.* **126** 1691 (1962)
79. Moskalenko S A, Khadzhi P I, Bobrysheva A I *Sov. Phys. Solid State* **5** 1051 (1963); *Fiz. Tverd. Tela* **5** 1444 (1963)
80. Keldysh L V, Kozlov A N *JETP Lett.* **5** 190 (1967); *Pis'ma Zh. Eksp. Teor. Fiz.* **5** 238 (1967)
81. Keldysh L V, Kozlov A N *Sov. Phys. JETP* **27** 521 (1968); *Zh. Eksp. Teor. Fiz.* **54** 978 (1968)
82. Gergel' V A, Kazarinov R F, Suris R A *Sov. Phys. JETP* **27** 159 (1968); *Zh. Eksp. Teor. Fiz.* **54** 298 (1968)
83. Keldysh L V, in *Electron-Hole Droplets in Semiconductors* (Modern Problems in Condensed Matter Sciences, Vol. 6, Eds C D Jeffries, L V Keldysh) (Amsterdam: North-Holland, 1983) p. xi; Translated into Russian: Keldysh L V, in *Elektronno-Dyrochnye Kapli v Poluprovodnikakh* (Eds C D Jeffries, L V Keldysh) (Moscow: Nauka, 1988) p. 7
84. Rice T M, in *Problems of Condensed Matter Physics: Quantum Coherence Phenomena in Electron-Hole and Coupled Matter-Light Systems* (International Series of Monographs on Physics, Vol. 139, Eds A L Ivanov, S G Tikhodeev) (Oxford: Oxford Univ. Press, 2008) p. 214
85. Pokrovskii Ya E, Svistunova K I *Sov. Phys. Semicond.* **4** 409 (1970); *Fiz. Tekh. Poluprovodn.* **4** 491 (1970)
86. Kaminskii A S, Pokrovskii Ya E, Alkeev N V *Sov. Phys. JETP* **32** 1048 (1971); *Zh. Eksp. Teor. Fiz.* **59** 1937 (1970)
87. Brinkman W F et al. *Phys. Rev. Lett.* **28** 961 (1972)
88. Combescot M, Nozieres P *J. Phys. C* **5** 2369 (1972)
89. Brinkman W F, Rice T M *Phys. Rev. B* **7** 1508 (1973)
90. Vashishta P, Bhattacharyya P, Singwi K S *Phys. Rev. Lett.* **30** 1248 (1973)
91. Vashishta P, Kalia R K, Singwi K S, in *Electron-Hole Droplets in Semiconductors* (Modern Problems in Condensed Matter Sciences, Vol. 6, Eds C D Jeffries, L V Keldysh) (Amsterdam: North-Holland, 1983) p. 1; Translated into Russian: Vashishta P, Kalia R K, Singwi K S, in *Elektronno-Dyrochnye Kapli v Poluprovodnikakh* (Eds C D Jeffries, L V Keldysh) (Moscow: Nauka, 1988) p. 26
92. Lo T K *Solid State Commun.* **15** 1231 (1974)
93. Thomas G A et al. *Phys. Rev. Lett.* **31** 386 (1973)
94. Pokrovskii Ya E, in *Electron-Hole Droplets in Semiconductor* (Modern Problems in Condensed Matter Sciences, Vol. 6, Eds C D Jeffries, L V Keldysh) (Amsterdam: North-Holland, 1983) p. 509; Translated into Russian: Pokrovskii Ya E, in *Elektronno-Dyrochnye Kapli v Poluprovodnikakh* (Eds C D Jeffries, L V Keldysh) (Moscow: Nauka, 1988) p. 374
95. Markiewicz R S, Timusk T, in *Electron-Hole Droplets in Semiconductors* (Modern Problems in Condensed Matter Sciences, Vol. 6, Eds C D Jeffries, L V Keldysh) (Amsterdam: North-Holland, 1983) p. 543; Translated into Russian: Markiewicz R S, Timusk T, in *Elektronno-Dyrochnye Kapli v Poluprovodnikakh* (Eds C D Jeffries, L V Keldysh) (Moscow: Nauka, 1988) p. 396
96. Bagaev V S et al. *JETP Lett.* **16** 83 (1972); *Pis'ma Zh. Eksp. Teor. Fiz.* **16** 120 (1972)
97. Murzin V N, Zayats V A, Kononenko V L *Sov. Phys. Solid State* **15** 2421 (1974); *Fiz. Tverd. Tela* **15** 3634 (1973)
98. Keldysh L V, Silin A P *Sov. Phys. Solid State* **15** 1026 (1973); *Fiz. Tverd. Tela* **15** 1532 (1973)
99. Karuzskii A L et al. *JETP Lett.* **22** 29 (1975); *Pis'ma Zh. Eksp. Teor. Fiz.* **22** 65 (1975)
100. Karuzskii A L et al. *Sov. Phys. JETP* **42** 554 (1975); *Zh. Eksp. Teor. Fiz.* **69** 1088 (1975)
101. Silin A P, in *Electron-Hole Droplets in Semiconductors* (Modern Problems in Condensed Matter Sciences, Vol. 6, Eds C D Jeffries, L V Keldysh) (Amsterdam: North-Holland, 1983) p. 619; Translated into Russian: Silin A P, in *Elektronno-Dyrochnye Kapli v Poluprovodnikakh* (Eds C D Jeffries, L V Keldysh) (Moscow: Nauka, 1988) p. 449
102. Rogachev A A, in *Excitons at High Density* (Springer Tracts in Modern Physics, Vol. 73, Eds H Haken, S Nikitine) (Berlin: Springer, 1974) p. 127
103. Keldysh L V, Silin A P *Sov. Phys. JETP* **42** 535 (1975); *Zh. Eksp. Teor. Fiz.* **69** 1053 (1975)
104. Beni G, Rice T M *Phys. Rev. Lett.* **37** 874 (1976)
105. Bir G L, Pikus G E *Symmetry and Strain-Induced Effects in Semiconductors* (New York: Wiley, 1974); Translated from Russian: Bir G L, Pikus G E *Simmetriya i Deformatsionnye Effekty v Poluprovodnikakh* (Moscow: Nauka, 1972)
106. Alekseev A S, Bagaev V S, Galkina T I *Sov. Phys. JETP* **36** 536 (1973); *Zh. Eksp. Teor. Fiz.* **63** 1020 (1972)
107. Bagaev V S, Galkina T I, Gogolin O V *Kratk. Soobshch. Fiz.* (2) 42 (1970)
108. Benoît à la Guillaume C, Voos M, Salvan F *Phys. Rev. B* **5** 3079 (1972)
109. Kulakovskii V D, Timofeev V B *JETP Lett.* **25** 458 (1977); *Pis'ma Zh. Eksp. Teor. Fiz.* **25** 487 (1977)
110. Kukushkin I V, Kulakovskii V D, Timofeev V B *JETP Lett.* **32** 280 (1980); *Pis'ma Zh. Eksp. Teor. Fiz.* **32** 304 (1980)
111. Kirczenow G, Singwi K S *Phys. Rev. B* **20** 4171 (1979)
112. Bagaev V S, Galkina T I, Sibeldin N N, in *Electron-Hole Droplets in Semiconductors* (Modern Problems in Condensed Matter Sciences,

- Vol. 6, Eds C D Jeffries, L V Keldysh (Amsterdam: North-Holland, 1983) p. 267; Translated into Russian: Bagaev V S, Galkina T I, Sibeldin N N, in *Electronno-Dyrochnye Kapli v Poluprovodnikakh* (Eds C D Jeffries, L V Keldysh) (Moscow: Nauka, 1988) p. 207
113. Wolfe J P, Jeffries C D, in *Electron-Hole Droplets in Semiconductors* (Modern Problems in Condensed Matter Sciences, Vol. 6, Eds C D Jeffries, L V Keldysh) (Amsterdam: North-Holland, 1983) p. 431; Translated into Russian: Wolfe J P, Jeffries C D, in *Electronno-Dyrochnye Kapli v Poluprovodnikakh* (Eds C D Jeffries, L V Keldysh) (Moscow: Nauka, 1988) p. 317
  114. Chui S T *Phys. Rev. B* **9** 3438 (1974)
  115. Buttner H, in *Proc. 12th Intern. Conf. on Physics of Semiconductors* (Ed. M H Pilkuhn) (Stuttgart: Teubner, 1974) p. 81
  116. Keldysh L V, Onishchenko T A *JETP Lett.* **24** 59 (1976); *Pis'ma Zh. Eksp. Teor. Fiz.* **24** 70 (1976)
  117. Seisyan R P *Spektroskopiya Diamagnitnykh Eksitonov* (Spectroscopy of Diamagnetic Excitons) (Moscow: Nauka, 1984)
  118. Seisyan R P, Zakharchenya B P, in *Landau Level Spectroscopy* (Modern Problems in Condensed Matter Sciences, Vol. 27, Eds G Landwehr, E I Rashba) (Amsterdam: North-Holland, 1991) p. 345
  119. Störmer H L, Martin R W *Phys. Rev. B* **20** 4213 (1979)
  120. Alberi K et al. *Phys. Rev. B* **93** 075310 (2016)
  121. Chernenko A V, Timofeev V B *JETP* **85** 593 (1997); *Zh. Eksp. Teor. Fiz.* **112** 1091 (1997)
  122. Kavetskaya I V et al. *JETP Lett.* **36** 311 (1982); *Pis'ma Zh. Eksp. Teor. Fiz.* **36** 254 (1982)
  123. Kavetskaya I V, Sibeldin N N, Tsvetkov V A *Solid State Commun.* **97** 157 (1996)
  124. Kavetskaya I V et al. *JETP* **84** 406 (1997); *Zh. Eksp. Teor. Fiz.* **111** 737 (1997)
  125. Sibeldin N N *Phys. Usp.* **46** 971 (2003); *Usp. Fiz. Nauk* **173** 999 (2003)
  126. Hensel J C, Phillips T G, Rice T M *Phys. Rev. Lett.* **30** 227 (1973)
  127. Gershenzon E M, Gol'tsman G N, Ptitsina N G *Sov. Phys. JETP* **43** 116 (1976); *Zh. Eksp. Teor. Fiz.* **70** 224 (1976)
  128. Westervelt R M, in *Electron-Hole Droplets in Semiconductors* (Modern Problems in Condensed Matter Sciences, Vol. 6, Eds C D Jeffries, L V Keldysh) (Amsterdam: North-Holland, 1983) p. 187; Translated into Russian: Westervelt R M, in *Electronno-Dyrochnye Kapli v Poluprovodnikakh* (Eds C D Jeffries, L V Keldysh) (Moscow: Nauka, 1988) p. 149
  129. Thomas G A et al. *Phys. Rev. Lett.* **31** 386 (1973)
  130. Thomas G A, Rice T M, Hensel J C *Phys. Rev. Lett.* **33** 219 (1974)
  131. Dite A F, Kulakovskii V D, Timofeev V B *Sov. Phys. JETP* **45** 604 (1977); *Zh. Eksp. Teor. Fiz.* **72** 1156 (1977)
  132. Feldman B J, Chou H-h, Wong G K *Solid State Commun.* **24** 521 (1977)
  133. Kulakovskii V D, Kukushkin I V, Timofeev V B *Sov. Phys. JETP* **51** 191 (1980); *Zh. Eksp. Teor. Fiz.* **78** 381 (1980)
  134. Forchel A et al. *Phys. Rev. Lett.* **46** 678 (1981)
  135. Nagai M et al. *Phys. Status Solidi B* **238** 509 (2003)
  136. Sauer R, Teofilov N, Thonke K *Diamond Related Mater.* **13** 691 (2004)
  137. Naka N, Omachi J, Kuwata-Gonokami M *Phys. Rev. B* **76** 193202 (2007)
  138. Kozák M et al. *Phys. Status Solidi RRL* **7** 278 (2013)
  139. Lipatov E I et al. *Proc. SPIE* **9810** 98101G (2015)
  140. Popelář T et al. *Diamond Related Mater.* **71** 13 (2017)
  141. Asnin V M, Rogachev A A, Sablina N I *JETP Lett.* **11** 99 (1970); *Pis'ma Zh. Eksp. Teor. Fiz.* **11** 162 (1970)
  142. Benoît à la Guillaume C et al. *C.R. Hebd. Seances Acad. Sci. B* **272** 236 (1971)
  143. Pokrovskii Ya E, Svistunova K I *JETP Lett.* **13** 212 (1971); *Pis'ma Zh. Eksp. Teor. Fiz.* **13** 297 (1971)
  144. Sibeldin N N et al. *Sov. Phys. Solid State* **15** 121 (1973); *Fiz. Tverd. Tela* **15** 177 (1973)
  145. Bagaev V S et al. *Sov. Phys. Solid State* **15** 2179 (1974); *Fiz. Tverd. Tela* **15** 3269 (1973)
  146. Worlock J M et al. *Phys. Rev. Lett.* **33** 771 (1974)
  147. Sibeldin N N *Proc. Lebedev Phys. Inst.* **97** 61 (1979); *Tr. Fiz. Inst. Akad. Nauk SSSR* **97** 63 (1977)
  148. Bagaev V S et al. *Sov. Phys. JETP* **43** 783 (1976); *Zh. Eksp. Teor. Fiz.* **70** 1501 (1976)
  149. Capizzi M et al. *Solid State Commun.* **16** 709 (1975)
  150. Silver R N *Phys. Rev. B* **11** 1569 (1975)
  151. Silver R N *Phys. Rev. B* **12** 5689 (1975)
  152. Etienne B, Benoît à la Guillaume C, Voos M *Phys. Rev. Lett.* **35** 536 (1975)
  153. Etienne B, Benoît à la Guillaume C, Voos M *Phys. Rev. B* **14** 712 (1976)
  154. Keldysh L V, Tikhodeev S G *Kratk. Soobshch. Fiz.* (8) 9 (1976)
  155. Westervelt R M *Phys. Status Solidi B* **74** 727 (1976)
  156. Staehli J L *Phys. Status Solidi B* **75** 451 (1976)
  157. Westervelt R M *Phys. Status Solidi B* **76** 31 (1976)
  158. Frenkel J *Kinetic Theory of Liquids* (Oxford: The Clarendon Press, 1946); Later ed. of the Russian original: Frenkel' Ya I *Kineticheskaya Teoriya Zhidkosti* (Leningrad: Nauka, 1975)
  159. Lo T K, Feldman B J, Jeffries C D *Phys. Rev. Lett.* **31** 224 (1973)
  160. Alekseev A S et al., in *Proc. of the 12th Intern. Conf. on Physics of Semiconductors* (Ed. M H Pilkuhn) (Stuttgart: Teubner, 1974) p. 91
  161. Bagaev V S, Sibel'din N N, Tsvetkov V A *JETP Lett.* **21** 80 (1975); *Pis'ma Zh. Eksp. Teor. Fiz.* **21** 180 (1975)
  162. Voisin R, Etienne B, Voos M *Phys. Rev. Lett.* **42** 526 (1979)
  163. Pokrovskii Ya *Phys. Status Solidi A* **11** 385 (1972)
  164. Kulakovskii V D, Pikus G E, Timofeev V B *Sov. Phys. Usp.* **24** 815 (1981); *Usp. Fiz. Nauk* **135** 237 (1981)
  165. Suzuki T, Shimano R *Phys. Rev. Lett.* **103** 057401 (2009)
  166. Sekiguchi F, Shimano R *Phys. Rev. B* **91** 155202 (2015)
  167. Westervelt R M et al. *Phys. Rev. Lett.* **32** 1051 (1974)
  168. Benoît à la Guillaume C et al. *Solid State Commun.* **15** 1031 (1974)
  169. Keldysh L V et al. *Sov. Phys. JETP* **39** 1072 (1974); *Zh. Eksp. Teor. Fiz.* **66** 2178 (1974)
  170. Katyrin V V et al. *Sov. Phys. Solid State* **20** 820 (1978); *Fiz. Tverd. Tela* **20** 1426 (1978)
  171. Ashkinadze B M, Fishman I M *Sov. Phys. Semicond.* **11** 235 (1977); *Fiz. Tekh. Poluprovodn.* **11** 408 (1977)
  172. Astemirov T A et al. *JETP Lett.* **24** 200 (1976); *Pis'ma Zh. Eksp. Teor. Fiz.* **24** 225 (1976)
  173. Manenkov A A et al. *Sov. Phys. JETP* **43** 359 (1976); *Zh. Eksp. Teor. Fiz.* **70** 695 (1976)
  174. Manenkov A A et al. *JETP Lett.* **16** 322 (1972); *Pis'ma Zh. Eksp. Teor. Fiz.* **16** 454 (1972)
  175. Zayats V A et al. *Sov. Phys. JETP* **46** 748 (1977); *Zh. Eksp. Teor. Fiz.* **73** 1422 (1977)
  176. Betzler K, Zhurkin B G, Karuzskii A L *Solid State Commun.* **17** 577 (1975)
  177. Cuthbert J D *Phys. Rev. B* **1** 1552 (1970)
  178. Ashkinadze B M et al. *Sov. Phys. JETP* **31** 271 (1970); *Zh. Eksp. Teor. Fiz.* **58** 507 (1970)
  179. Ashkinadze B M et al. *Phys. Status Solidi B* **46** 495 (1971)
  180. Dite A F, Lysenko V G, Timofeev V B *Phys. Status Solidi B* **66** 53 (1974)
  181. Schmid W *Solid State Commun.* **19** 347 (1976)
  182. Keldysh L V, Tikhodeev S G *JETP Lett.* **21** 273 (1975); *Pis'ma Zh. Eksp. Teor. Fiz.* **21** 582 (1975)
  183. Alekseev A S et al. *JETP Lett.* **21** 271 (1975); *Pis'ma Zh. Eksp. Teor. Fiz.* **21** 578 (1975)
  184. Alekseev A S et al. *Sov. Phys. JETP* **52** 109 (1980); *Zh. Eksp. Teor. Fiz.* **79** 216 (1980)
  185. Bagaev V S et al. *JETP Lett.* **32** 332 (1980); *Pis'ma Zh. Eksp. Teor. Fiz.* **32** 356 (1980)
  186. Bagaev V S et al. *Sov. Phys. JETP* **43** 362 (1976); *Zh. Eksp. Teor. Fiz.* **70** 702 (1976)
  187. Alekseev A S, Galkina T I *Sov. Phys. Solid State* **18** 1167 (1976); *Fiz. Tverd. Tela* **18** 2005 (1976)
  188. Keldysh L V, Tikhodeev S G *Sov. Phys. Solid State* **19** 63 (1977); *Fiz. Tverd. Tela* **19** 111 (1977)
  189. Etienne B et al. *Phys. Rev. Lett.* **37** 1299 (1976)
  190. Tamor M A, Wolfe J P *Phys. Rev. B* **24** 3596 (1981)
  191. Tamor M A, Wolfe J P *Phys. Rev. B* **26** 5743 (1982)
  192. Jeffries C D *Science* **189** 955 (1975)
  193. Markiewicz R S, Wolfe J P, Jeffries C D *Phys. Rev. Lett.* **32** 1357 (1974)
  194. Wolfe J P et al. *Phys. Rev. Lett.* **34** 275 (1975)



195. Pokrovskii Ya E, Svistunova K I *JETP Lett.* **23** 95 (1976); *Pis'ma Zh. Eksp. Teor. Fiz.* **23** 110 (1976)
196. Mattos J C V, Worlock J M, Damen T C *Solid State Commun.* **35** 519 (1980)
197. Kaminskii A S, Pokrovskii Ya E *JETP Lett.* **21** 197 (1975); *Pis'ma Zh. Eksp. Teor. Fiz.* **21** 431 (1975)
198. Furneaux J E, Wolfe J P, Jeffries C D *Solid State Commun.* **20** 317 (1976)
199. Manenkov A A et al. *JETP Lett.* **24** 122 (1976); *Pis'ma Zh. Eksp. Teor. Fiz.* **24** 141 (1976)
200. Ohyama T, Hansen A D A, Turney J L *Solid State Commun.* **19** 1083 (1976)
201. Keldysh L V *JETP Lett.* **23** 86 (1976); *Pis'ma Zh. Eksp. Teor. Fiz.* **23** 100 (1976)
202. Astemirov T A et al. *JETP Lett.* **24** 200 (1976); *Pis'ma Zh. Eksp. Teor. Fiz.* **24** 225 (1976)
203. Hensel J C, Dynes R C *Phys. Rev. Lett.* **39** 969 (1977)
204. Astemirov T A et al. *Sov. Phys. Solid State* **19** 547 (1977); *Fiz. Tverd. Tela* **19** 937 (1977)
205. Hensel J C, Dynes R C, in *Phonon Scattering in Condensed Matter. Proc. of the 3rd Intern. Conf.* (Ed. H J Maris) (New York: Plenum Press, 1980) p. 395
206. Bagaev V S et al. *Sov. Phys. JETP* **50** 1013 (1979); *Zh. Eksp. Teor. Fiz.* **77** 2117 (1979)
207. Dietsche W, Kirch S J, Wolfe J P *Phys. Rev. B* **26** 780 (1982)
208. Kirch S J, Wolfe J P *Phys. Rev. B* **29** 3382 (1984)
209. Guseinov N M, Levinson I B *Sov. Phys. JETP* **58** 452 (1983); *Zh. Eksp. Teor. Fiz.* **85** 779 (1983)
210. Kazakovtsev D V, Levinson I B *Sov. Phys. JETP* **61** 1318 (1985); *Zh. Eksp. Teor. Fiz.* **88** 2228 (1985)
211. Guseinov N M, Orudzhev G S *Sov. Phys. Solid State* **29** 1308 (1987); *Fiz. Tverd. Tela* **29** 2269 (1987)
212. Levinson Y B, in *Nonequilibrium Phonons in Nonmetallic Crystals* (Modern Problems in Condensed Matter Science, Vol. 16, Eds W Eisenmenger, A A Kaplyanskii) (Amsterdam: North-Holland, 1986) p. 91
213. Bragina T M, Konin K P, Shreter Yu G *Sov. Phys. Solid State* **19** 1086 (1977); *Fiz. Tverd. Tela* **19** 1872 (1977)
214. Hensel J C *Solid State Commun.* **31** 443 (1979)
215. Asnin V M *Sov. Phys. Solid State* **23** 99 (1981); *Fiz. Tverd. Tela* **23** 177 (1981)
216. Doehler J, Worlock J M *Phys. Rev. Lett.* **41** 980 (1978)
217. Manenkov A A et al. *Phys. Status Solidi B* **134** 631 (1986)
218. Tsvetkov V A et al. *JETP Lett.* **42** 335 (1985); *Pis'ma Zh. Eksp. Teor. Fiz.* **42** 272 (1985)
219. Zamkovets N V, Sibel'din N N, Tsvetkov V A *JETP* **78** 572 (1994); *Zh. Eksp. Teor. Fiz.* **105** 1066 (1994)
220. Markiewicz R S *Phys. Rev. B* **21** 4674 (1980)
221. Markiewicz R S *Solid State Commun.* **33** 701 (1980)
222. Doehler J, Mattos J C V, Worlock J M *Phys. Rev. Lett.* **38** 726 (1977)
223. Zamkovets N V et al. *Sov. Phys. JETP* **62** 1274 (1985); *Zh. Eksp. Teor. Fiz.* **89** 2206 (1985)
224. Shaklee K L, in *Proc. of the 3rd Intern. Conf. on Light Scattering in Solids* (Paris: Flammarion, 1976) p. 160
225. Bragina T M, Lelikov Yu S, Shreter Yu G *Sov. Phys. JETP* **52** 929 (1980); *Zh. Eksp. Teor. Fiz.* **79** 1838 (1980)
226. Greenstein M, Wolfe J P *Phys. Rev. Lett.* **41** 715 (1978)
227. Greenstein M, Wolfe J P *Solid State Commun.* **33** 309 (1980)
228. Greenstein M, Wolfe J P *Phys. Rev. B* **24** 3318 (1981)
229. Greenstein M, Wolfe J P, Haller E E *Solid State Commun.* **35** 1011 (1980)
230. Markiewicz R S, Greenstein M, Wolfe J P *Solid State Commun.* **35** 339 (1980)
231. Maris H J, in *Nonequilibrium Phonons in Nonmetallic Crystals* (Modern Problems in Condensed Matter Science, Vol. 16, Eds W Eisenmenger, A A Kaplyanskii) (Amsterdam: North-Holland, 1986) p. 51
232. Tamor M A, Wolfe J P *Phys. Rev. B* **21** 739 (1980)
233. Damen T C, Worlock J M, in *Proc. of the 3rd Intern. Conf. on Light Scattering in Solids* (Paris: Flammarion, 1976) p. 183
234. Sibel'din N N *JETP Lett.* **38** 207 (1983); *Pis'ma Zh. Eksp. Teor. Fiz.* **38** 177 (1983)
235. Zamkovets N V et al. *Sov. Phys. JETP* **47** 603 (1978); *Zh. Eksp. Teor. Fiz.* **74** 1147 (1978)
236. Kavetskaya I V et al. *Sov. Phys. Solid State* **20** 2085 (1978); *Fiz. Tverd. Tela* **20** 3608 (1978)
237. Greenstein M, Tamor M A, Wolfe J P *Solid State Commun.* **45** 355 (1983)
238. Tamor M A, Greenstein M, Wolfe J P *Phys. Rev. B* **27** 7353 (1983)
239. Bulatov A E, Tikhodeev S G *Phys. Rev. B* **46** 15058 (1992)
240. Tikhodeev S G, Gippius N A, Kopelevich G A *Phys. Status Solidi A* **178** 63 (2000)
241. Monte A F G et al. *Phys. Rev. B* **62** 6924 (2000)
242. Kleinman D A *Phys. Rev. B* **33** 2540 (1986)
243. Bauer G E W, Ando T *Phys. Rev. B* **34** 1300 (1986)
244. Ando T, Nakayama M, Hosoda M *Phys. Rev. B* **69** 165316 (2004)
245. Hawrylak P *Phys. Rev. B* **39** 6264(R) (1989)
246. Inagaki A, Katayama S *Solid State Commun.* **125** 337 (2003)
247. Belykh V V, Kochiev M V *Phys. Rev. B* **92** 045307 (2015)
248. Lee R M, Drummond N D, Needs R J *Phys. Rev. B* **79** 125308 (2009)
249. Kalt H et al. *Solid State Commun.* **83** 285 (1992)
250. Furukawa Y, Nakayama M *J. Phys. Conf. Ser.* **619** 012005 (2015)
251. Furukawa Y, Nakayama M *Phys. Status Solidi C* **13** 101 (2016)
252. Timofeev V B et al. *Phys. Rev. B* **61** 8420 (2000)
253. Stern M, Umansky V, Bar-Joseph I *Science* **343** 55 (2014)
254. Almand-Hunter A E et al. *Nature* **506** 471 (2014)
255. Mootz M et al. *Proc. SPIE* **9361** 936114 (2015)
256. Kira M et al. *Nature Phys.* **7** 799 (2011)
257. Tajima M, Ibuka S *J. Appl. Phys.* **84** 2224 (1998)
258. Calvo V et al. *Opt. Mater.* **17** 107 (2001)
259. Pauc N et al. *Phys. Rev. Lett.* **92** 236802 (2004)
260. Pauc N et al. *Phys. Rev. B* **72** 205324 (2005)
261. Roigé A et al. *Phys. Status Solidi RRL* **8** 943 (2014)
262. Keldysh L V *JETP Lett.* **29** 658 (1979); *Pis'ma Zh. Eksp. Teor. Fiz.* **29** 716 (1979)
263. Keldysh L V *Phys. Status Solidi A* **164** 3 (1997)
264. Rodina A V, Efros Al L *JETP* **122** 554 (2016); *Zh. Eksp. Teor. Fiz.* **149** 641 (2016)
265. Van de Walle C G, Martin R M *Phys. Rev. B* **34** 5621 (1986)
266. Yang L et al. *Semicond. Sci. Technol.* **19** 1174 (2004)
267. Sibeldin N N *JETP* **122** 587 (2016); *Zh. Eksp. Teor. Fiz.* **149** 678 (2016)
268. Burbaev T M et al. *JETP Lett.* **85** 331 (2007); *Pis'ma Zh. Eksp. Teor. Fiz.* **85** 410 (2007)
269. Burbaev T M et al. *Thin Solid Films* **517** 55 (2008)
270. Burbaev T M et al. *JETP Lett.* **92** 305 (2010); *Pis'ma Zh. Eksp. Teor. Fiz.* **92** 341 (2010)
271. Shepel D et al. *Phys. Status Solidi C* **8** 1186 (2011)
272. Steiner T W et al. *Solid State Commun.* **89** 429 (1994)
273. Rieger M M, Vogl P *Phys. Rev. B* **48** 14276 (1993)
274. Penn C et al. *Phys. Rev. B* **59** 13314 (1999)
275. Orlov A, Levashova N, Burbaev T J. *Phys. Conf. Ser.* **586** 012003 (2015)
276. Betzler K, Conradt R *Phys. Rev. Lett.* **28** 1562 (1972)
277. Betzler K, Weller T, Conradt R *Phys. Rev. B* **6** 1394 (1972)
278. Krivobok V S et al. *JETP Lett.* **104** 231 (2016); *Pis'ma Zh. Eksp. Teor. Fiz.* **104** 229 (2016)
279. Burbaev T M et al. *JETP Lett.* **98** 823 (2013); *Pis'ma Zh. Eksp. Teor. Fiz.* **98** 926 (2013)
280. Burbaev T M et al., in *Proc. Intern. Conf. Nanomaterials: Applications and Properties, September 21–27, 2014* Vol. 3 No. 1 (2014) 01NTF01
281. Kulakovskii V D, Lysenko V G, Timofeev V B *Sov. Phys. Usp.* **28** 735 (1985); *Usp. Fiz. Nauk* **147** 3 (1985)
282. Baier T et al. *Phys. Rev. B* **50** 15191 (1994)
283. Blokhintsev D I *Osnovy Kvantovoi Mekhaniki* (Foundations of Quantum Mechanics) (Moscow: Vysshaya Shkola, 1963) p. 398
284. Zaitsev V V et al. *Physica E* **40** 1172 (2008)
285. Bagaev V S et al. *JETP* **107** 846 (2008); *Zh. Eksp. Teor. Fiz.* **134** 988 (2008)
286. Bagaev V S et al. *Phys. Rev. B* **82** 115313 (2010)
287. Bagaev V S et al. *JETP Lett.* **94** 63 (2011); *Pis'ma Zh. Eksp. Teor. Fiz.* **94** 63 (2011)
288. Bagaev V S et al. *JETP* **117** 912 (2013); *Zh. Eksp. Teor. Fiz.* **144** 1045 (2013)



289. Bagaev V S et al. *J. Appl. Phys.* **117** 185705 (2015)
290. Nikolaev S N et al. *JETP Lett.* **104** 163 (2016); *Pis'ma Zh. Eksp. Teor. Fiz.* **104** 161 (2016)
291. Stoica T, Vescan L J. *J. Appl. Phys.* **94** 4400 (2003)
292. Zrenner A et al. *Phys. Rev. B* **52** 16608 (1995)
293. Aminev D F et al. *JETP Lett.* **105** 179 (2017); *Pis'ma Zh. Eksp. Teor. Fiz.* **105** 164 (2017)
294. Burbaev T M et al., in *Proc. of the 21st Intern. Symp. Nanostructures: Physics and Technology* (St. Petersburg: Academic Univ., 2013) p. EN.07
295. Bagaev V S et al. *JETP* **121** 1052 (2015); *Zh. Eksp. Teor. Fiz.* **148** 1198 (2015)
296. Andryushin E A, Silin A P *Sov. Phys. Solid State* **21** 491 (1979); *Fiz. Tverd. Tela* **21** 839 (1979)
297. Keldysh L V “Kogerentnye sostoyaniya eksitonov” (Coherent states of excitons), in *Problemy Teoreticheskoi Fiziki. Pamyati Igorya Evgen'evicha Tamma* (Problems of Theoretical Physics. In Memory of Igor Evgen'evich Tamm) (Ed. V I Ritus) (Moscow: Nauka, 1972) p. 433
298. Keldysh L V *Phys. Usp.* **60** (11) (2017) <https://doi.org/10.3367/UFNe.2017.10.038227>; *Usp. Fiz. Nauk* **187** 1273 (2017)